**UNIVERSITÀ DEGLI STUDI DI TRENTO**

Facoltà di Scienze Matematiche, Fisiche e Naturali

Dipartimento di Fisica

---

Tesi di Dottorato di Ricerca in Fisica
Ph.D. Thesis in Physics

# Ground state and dynamical properties of many–body systems by non conventional Quantum Monte Carlo algorithms

Supervisor:
Prof. Francesco Pederiva

Candidate:
Alessandro Roggero

Dottorato di Ricerca in Fisica, XXVII ciclo
Trento, 4 November, 2014

# Contents

# Introduction and Motivations

> *The fundamental laws necessary for the mathematical treatment of large part of physics and the whole of chemistry are completely known, and the difficulties lies only in the fact that application of these laws leads to equations that are too complex to be solved.*
>
> Paul Dirac – 1929

A complete description of a quantum system composed by even a small number of interacting particles remains one of the most challenging problems in theoretical physics today. The main difficulty being the presence of interaction–induced correlations between particles, this in general forces the description of the state of the system to live in a space which is exponentially large in the number of degrees of freedom. Theoreticians realized the problem already in the early days of Quantum Mechanics as summarized in Dirac's famous quote above.

A great effort as been dedicated in the past to the development of reliable approximations to this *Quantum Many–Body Problem* (QMBP) with the hope of predicting properties of real systems starting only from the underlying physical theory, an approach that has come to be know as *ab–initio*. For non–relativistic particles, which are the focus of the present work, this translates to solving the $N$–particle Schroedinger equation with the bare inter–particle potential. In some cases this approach can be attacked head–on since the inter–particle interaction is well–defined and known, such as the Coulomb potential between point–particles in Chemistry. In other cases, as the nuclear many–body problem, even the interaction between the effective degrees of freedom (the nucleons) is not known and thus a strictly *ab–initio* description is not possible. Nevertheless, once a choice has been made for the inter–particle interaction, the problem of solving the corresponding Schroedinger equation is perfectly well–posed and usually the term *ab–initio* is used for techniques that approximately solve it without introducing phenomenological parameters in the theory. This will be the methods we will focus on during this work.

The simplest $N$–body problem is the 1–body problem and then the first attempts to address the QMBP are mean–field theories that replaces the correlated degrees of freedom of the particles with a collection of effective ones that (hopefully) don't interact with each other, the so called *quasi–particles*. This clearly provides a huge simplification to the initial problem. Contrary to

what one may think at the beginning this approximation doesn't work well only in weakly–correlated systems, but it may happen that, after changing basis to quasi–particles, the *residual interaction* between them turns out to be very weak. Phonons in harmonic lattices are a simple example of this appealing behavior. A famous example of this kind of approach is the Hartree–Fock method [1, 2], a variational approach where the independent–particle assumption is encoded in the analytical form of the wave–function to be minimized: a Slater–determinant of single–particle states for fermions. In this way the HF solution represents the best approximation to the wanted solution of the $N$–particle Schroedinger equation that can be written as a direct sum of $N$ 1–particle solutions.

The variational approach is very powerful and can be fruitfully employed also with variational wave–functions that explicitly contain correlations, providing a better description of the ground–state of the system. The technically challenging task here is the evaluation of the cost–function that has to be minimized: the expectation value of the Hamiltonian on the correlated wave–function. Different methods have been developed in the years to deal with this problem, both deterministically such as the Fermi–Hyper–Netted–Chain [3, 4] and stochastically such as the Variational Monte Carlo [5]. We will discuss more the Variational Monte Carlo technique in later chapters.

When the starting mean–field state is a good approximation of the true solution one may also resort to some sort of perturbation theory to add the missing correlations to the starting state. Many techniques have been developed in the past, from Many–Body Perturbation Theory [6] to methods that employ diagram resummations like Bethe–Bruekner–Goldstone theory [7], Self–Consistent Green's Functions theory [8] and Coupled–Cluster (CC) theory [9] among the others.

It is also possible to include the effects of correlations without resorting to any series expansion by using stochastic methods like Quantum Monte Carlo [10]. The price to pay is the presence of statistical noise in all the predicted properties, noise that, thanks to the Central Limit Theorem (cf. Section 1.1), can be made arbitrarily small with more computation. These techniques are capable of providing *exact* results for strongly correlated bosonic systems and can be adapted to deal with fermionic degrees of freedom usually with just controllable approximations, and all this with a favorable (polynomial) scaling with system size. Quantum Monte Carlo (QMC) methods have now become standard tools for computations in a wide variety of strongly correlated systems [11] ranging from quantum chemistry [12, 13] to condensed matter [14, 15], and nuclear physics [16]. As example, some of the most accurate calculations for light nuclei and neutron matter were performed using continuum diffusion based QMC methods, i.e., nuclear Green's function Monte Carlo (GFMC) and Auxiliary Field Diffusion Monte Carlo (AFDMC) [17, 18, 19, 20], in conjunction with the semi–phenomenological Argonne-Urbana family of nuclear forces [21, 22].

The focus of the research presented in this thesis is to extend QMC techniques in order to obtain better accuracy, control on the results and in general to extend the range of applicability of these methods. In this work we will focus mainly on two subjects, the first of which is an extension of Diffusion Monte Carlo (see sec 1.2.1) to work in a general Fock–space (cf. [23, 24]). This allows us to directly compare with, and actually use results of, the well–established

Many–body methods that work on spaces generated by some set of single–particle states like the above mentioned Many–Body Perturbation Theory and Coupled–Cluster. As example of the advantages this brings, one of the drawbacks of CC theory is the non–variational nature of the calculated energy and more generally the difficulty of calculating expectation values using the wave–function obtained from the calculation; the availability of a QMC algorithm that work in the same space allows then not only variational estimates of the CC energies but, even more interestingly, the possibility to calculate consistently any observable. Working in a discrete space brings also other enjoyable properties like the possibility to use non–local interactions in the calculations, something that with conventional methods is doable only at the price of introducing uncontrollable approximations. The extension to these non–local interaction is essential for instance in Nuclear Structure where modern potentials derived in the framework of Chiral Effective Field Theory [25, 26, 27] are naturally of non–local character, at least at high enough order in the momentum expansion[1]. Extension of QMC to deal efficiently with these interaction is thus of pivotal importance in order to disentangle, by comparing with other techniques, the role played by the interaction from the effects coming from the many–body treatment employed. Besides the importance of pinpointing the nucleon–nucleon interaction, an everlasting challenge in nuclear theory, accurate results can be obtained to constrain effective theories (like e.g. Density Functional or Relativistic Mean Field Theory) that may be then employed to study systems whose complexity is far beyond the reach of *ab–initio* calculations (cf Section 3.2). As example the homogeneous part of Density Functionals used in Chemistry for electronic structure calculations [29] is fitted to reproduce accurate Quantum Monte Carlo results for the electron gas [30].

The second main topic addressed in this work is the computation of dynamical properties of strongly interacting Many–Body systems. Many important physical properties of matter, from viscosity to magnetic susceptibility, are closely linked to the underlying microscopic dynamics. Understanding the details of this microscopic dynamics is thus one of the fundamental goals of Many–Body theory. A big drawback of QMC methods is however their inability to treat in a reliable way dynamical properties of quantum systems, this failure is essentially linked to the fact that QMC works in imaginary-time (see Section 1.2.1) so for quantities that do not directly translate into imaginary-time language the noise can be hardly reduced and calculations becomes unfeasible. The usual way to turn around that problem is to compute quantities in imaginary-time first and then use analytic–continuation into the real time, this procedure is accomplished by an inverse Laplace transform of noisy data, a notorious ill-posed problem [31, 32, 33].

Even if useful in sometimes as we shall see, this approach breaks–down in many interesting cases; for example the probably most notorious failure is that even the more sophisticated inversion scheme, the Maximum Entropy Method, cannot resolve the double peaked structure of the dynamic structure factor of superfluid $He^4$ (see Fig 1). Only very recently [34] this two–peak structure has been obtained trough the inversion of imaginary–time data with a novel inversion technique know as Genetic Inversion via Falsification of Theories (GIFT).

[1] see however [28] for a recent attempt to incorporate chiral interactions in continuum QMC by removing non-localities up to next-to-next-to-leading order (NNLO)

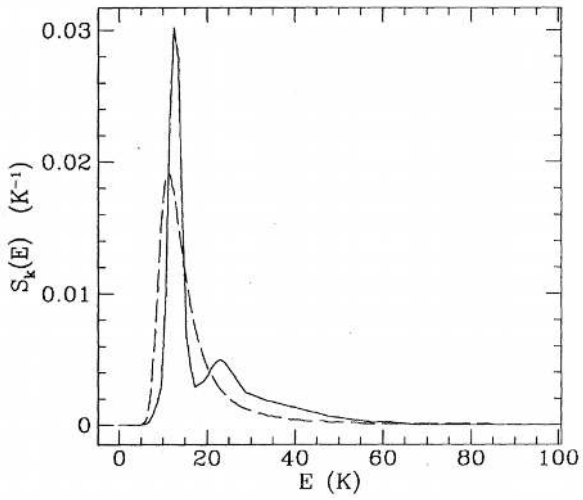


Figure 1: Dynamical structure factor for liquid $He^4$ at 1.2 K and wavelength $Q = 0.76A^{-1}$. Solid line as measured by neutron scattering [36]; dashed curve MEM reconstruction from the PIMC data [37]

Also recently, an hybrid semiclassical–PIMC calculation as been carried out to study the high-momentum response function in this system with encouraging results [35], it is however difficult to extend such results to the low–momentum transfer region that we are interested in. In this work we try to devise a method to alleviate these problems by adopting the Integral Transform approach on which is based the LIT method [38], now a powerful tool to study dynamical properties of few body nuclear systems and one of the few capable to address problems in the continuum part of the hamiltonian spectrum. The idea is to replace the commonly used Laplace transform with a different one that is more suitable to obtain stable inversions.

The thesis is structured with a first chapter that introduces the relevant notions at the foundation of Monte Carlo methods and present the key algorithms in a general basis–independent fashion. We will then specialize in Chapter 2 to our Diffusion Monte Carlo in Fock–space and then present applications to nuclear–system with non–local Chiral interactions in the following chapter. We will then present in Chapter 5 the techniques used for the calculations for the superfluid $He^4$ system, with a focus on bosonic systems only. Chapter 4 reviews the above mentioned Integral Transform approach together to a critical discussion on the role of kernel function. We finally present results for the dynamical properties of $He^4$ in the last chapter.

# Chapter 1

# Monte Carlo Methods

Solving the Schroedinger for an interacting many–body system is a really challenging task, the aim of this chapter is to introduce the stochastic techniques used in this work to pursue this goal. To set the stage let us start by considering a somewhat simpler, but technically still very challenging, problem: the calculation of expectation values on a correlated $N$–body wave–function $\Psi(\mathbf{R})$

$$\langle O \rangle_\phi = \frac{\int d\mathbf{R} \Psi^*(\mathbf{R}) O(\mathbf{R}) \Psi(\mathbf{R})}{\int d\mathbf{R} |\Psi(\mathbf{R})|^2} \tag{1.1}$$

where $\mathbf{R}$ is $3N$–dimensional vector and for simplicity we have considered $O$ to be a local operator. The evaluation of the above expression is a formidable task already for small numbers of particles mainly due to the dimensionality of the problem. Stochastic techniques can however be employed if we interpret the above expectation value as an average over a suitable Probability Density Function (PDF) defined over this $3N$–dimensional space. The great advantage in this strategy is that, thanks to the Central Limit Theorem, the error on the stochastic estimator obtained from $M$ sampled configurations scales as $err(M) \propto M^{-\frac{1}{2}}$ *regardless* of the dimensionality of the problem.

This favorable scaling of computational time with system size, while preserving at the same time the capability of accurate results, has motivated the adoption of Monte Carlo techniques in many fields of Physics. Classical systems in thermal equilibrium can be efficiently tackled by Classical Monte Carlo techniques, which are exact methods to sample from the Boltzmann distribution at finite temperature. For quantum systems, in the last two decades Quantum Monte Carlo (QMC) methods have become a standard tool for computations in a wide variety of strongly correlated systems [11] ranging from quantum chemistry [12, 13] to condensed matter [14, 15], and nuclear physics [16]. QMC are generally methods to solve the Schroedinger equation of non-relativistic Quantum Mechanics, and these will be the methods that we will focus most in this presentation. The applicability of stochastic integration to solve partial differential equation comes from the fact that we can map a differential equation into a corresponding integral one (using e.g. Green's functions) and this is the problem that we are actually going to solve. Monte Carlo methods can also be applied in relativistic theories and are in practice the only viable method to treat the low-energy non perturbative limit on Quantum Chromo Dynamics[39].

In the next section we will present the basic ideas of Monte Carlo sampling by presenting the Variational Monte Carlo method. We then focus on Projection Monte Carlo techniques that will be used to solve the Schroedinger equation.

## 1.1 Introduction

The first, natural, application of stochastic integration ideas to Quantum Mechanics is for the computation of expectation values of the form:

$$\begin{aligned}\langle O\rangle_\phi &= \frac{\langle\phi|\hat{O}|\phi\rangle}{\langle\phi|\phi\rangle} \\ &= \frac{\int d\nu\langle\phi|\nu\rangle\langle\nu|\hat{O}|\phi\rangle}{\int d\nu\langle\phi|\nu\rangle\langle\nu|\phi\rangle} \\ &\equiv \frac{\int d\nu\phi^*(\nu)\left(\hat{O}\phi\right)(\nu)}{\int d\nu|\phi(\nu)|^2},\end{aligned} \tag{1.2}$$

where for convenience we have introduced a complete set of states $\int d\nu|\nu\rangle\langle\nu|$. As mentioned in the introduction to this chapter, we have to express this expectation value in a form suitable for MC integration:

$$\begin{aligned}\langle O\rangle_\phi &= \frac{\int d\nu\phi^*(\nu)\left(\hat{O}\phi\right)(\nu)}{\int d\nu|\phi(\nu)|^2} \\ &= \frac{\int d\nu\phi^*(\nu)\frac{\phi(\nu)}{\phi(\nu)}\left(\hat{O}\phi\right)(\nu)}{\int d\nu|\phi(\nu)|^2} \\ &= \int d\nu\ \frac{|\phi(\nu)|^2}{\int d\nu|\phi(\nu)|^2}\ \frac{\hat{O}\phi}{\phi}(\nu) \\ &= \int d\nu\ f(\nu)\ o(\nu) \equiv \mathbb{E}_f\left[o(\mathbf{X})\right]\end{aligned} \tag{1.3}$$

which can be interpreted as the expected value of the function $o(\nu) = \hat{O}\phi(\nu)/\phi(\nu)$ over the perfectly valid (ie. positive–definite and normalized) Probability Density Function $f(\nu)$. The basic tool that we need is then to have the ability to generate samples from some known PDF $f$. Fortunately there are general purpose techniques for generating random numbers with the proper distribution such as the Markov Chain Monte Carlo. The idea is to generate a sequence of random configurations, with the next one depending only on its predecessor, in such a way that asymptotically these configurations are distributed according to $f$. If we start from a configuration $X_i$ the probability to end up in the configuration $Y_i$ after the step can be described by a stochastic matrix $\mathbf{M}(X_i, Y_i)$ and one can show that the asymptotic distribution sampled by such process is the dominant right–eigenvector of the matrix $\mathbf{M}$. Metropolis et al. [40] proposed a constructive way for generating $\mathbf{M}$ given the target density $f$, it relies on the factorization of the matrix

$$\mathbf{M}(X_i, Y_i) = \mathbf{T}(X_i, Y_i)\mathbf{A}(X_i, Y_i) \tag{1.4}$$

into a *proposal* one $\mathbf{T}$ from which we generate $Y_i$ starting from $X_i$ and an *acceptance* one $\mathbf{A}$ that gives the probability to accept the proposed move to $Y_i$.

The key finding is that, regardless of both $\mathbf{T}$ and the target distribution $f$, if we choose for $\mathbf{A}$ the following form

$$\mathbf{A}(X_i, Y_i) = \min\left[1, \frac{\mathbf{T}(X_i, Y_i) f(Y_i)}{\mathbf{T}(Y_i, X_i) f(X_i)}\right], \tag{1.5}$$

then the random process will produce samples distributed according to $f$. The configurations undergoing this random process will be called *walkers*. The role of the transition matrix is to control the efficiency of the overall process since low acceptance probabilities will reduce the number of samples effectively generated [41] (see also [42]).

Moreover, the fact that PDFs enter as a ratio in (1.5) allow us the great simplification of neglecting completely the normalization factor: $f(\nu) \equiv |\phi(\nu)|^2$.

The Monte Carlo estimator of expression (1.3) is then obtained as an arithmetic sum

$$\widetilde{\langle O \rangle}_\phi = \frac{1}{M} \sum_{i=1}^{M} O_L(\nu_i) \tag{1.6}$$

of so–called *local* observables:

$$\begin{aligned} O_L(\nu_i) &= \frac{\langle \nu_i | \hat{O} | \phi \rangle}{\langle \nu_i | \phi \rangle} \\ &= \frac{\int d\mu \langle \nu_i | \hat{O} | \mu \rangle \langle \mu | \phi \rangle}{\langle \nu_i | \phi \rangle} \end{aligned} \tag{1.7}$$

evaluated on the $M$ configurations $\nu_i$ sampled from $f(\nu)$.

This approach is clearly useful when we have access to some complicated wave function $\phi$ and we have no other practical way of computing the expectation value (1.2). It is also extremely useful for finding good approximations for the ground–state of interacting many–body Hamiltonians, and is in this context that is usually referred to as Variational Monte Carlo (VMC) [5]. In the particular case $\hat{O} = \hat{H}$ we have in fact a *variational theorem*

$$E_0 = \frac{\langle \Phi_0 | \hat{H} | \Phi_0 \rangle}{\langle \Phi_0 | \Phi_0 \rangle} \leq \frac{\langle \phi | \hat{H} | \phi \rangle}{\langle \phi | \phi \rangle} = E_\phi \tag{1.8}$$

where $\Phi_0$ is the ground–state wave–function and the equality holds only in the case $\phi \equiv \Phi_0$. The above relation can then be used to choose the best approximation to $\Phi_0$ among a parametrized family of wave–functions $\phi(\alpha_1, \alpha_2, \dots)$. The power of the method relies in the great flexibility on the choice of the wave–functions that can explicitly incorporate correlations. This extremely accurate wave–functions usually depend on a large number of parameters [43] and need to be optimized trough suitable minimization schemes [44, 45, 46].

Optimized approximations to the ground–state wave–function are extremely useful in Projection MC methods, like the ones we will encounter in the next sections, since they directly control both the efficiency and final accuracy of these algorithms [47].

## 1.2 Projection Monte Carlo Algorithms

We will now turn to the Quantum Monte Carlo methods that will be used to find the ground–state of interacting many–body hamiltonians: Diffusion Monte Carlo and Reptation Monte Carlo.

In the introduction we have seen how to produce a random process that samples a *known* target density $f$ by properly crafting a stochastic matrix $\mathbf{M}$ of which $f$ is the dominant right–eigenvector. The same ideas can be however applied also for the opposite process: producing a random process that will produce the dominant right–eigenvector of a *known* matrix. This is exactly the same idea underlying the so–called *Power Method* (PM) for finding the eigenvector corresponding to the biggest eigenvalue of a given matrix $\mathbf{M}$:

1. start with some initial vector $v_0$
2. apply the matrix (matrix–vector multiplication) $\tilde{v}_{k+1} = \mathbf{M}v_k$
3. normalize the resulting vector $v_{k+1} = \tilde{v}_{k+1}/\|\tilde{v}_{k+1}\|$
4. check for convergence ($v_{k+1} \approx v_k$), if not go back to 2.

The main difference is that step 2. will be done stochastically stochastically using Monte Carlo and thus we can treat extremely big (in many cases also infinite–dimensional) matrices, provided the matrix we are dealing with is sufficiently sparse. The PM is expected to work whenever we have a finite gap between the dominant eigenvalue and the rest of the spectrum and also when that eigenvalue is not degenerate. The rate of convergence of this scheme is however usually rather slow ($\approx$ linear), but we can improve on it by noticing that the algorithm works even if instead of just multiplying the matrix $\mathbf{M}$ in step 2. we apply any monotonic function of it. A more efficient choice, provided its action on the current vector is easily computable, would be to use an exponential of $\mathbf{M}$. In this way we can hope for an exponential convergence towards the wanted solution.

### 1.2.1 Diffusion Monte Carlo (DMC)

Diffusion Monte Carlo is probably the most widespread variant of QMC for zero–temperature ground-state calculations of strongly correlated systems. The goal is to solve the time–independent Schroedinger equation producing samples distributed according to the ground-state wave-function, once these are available we can calculate relevant expectation values over it. The starting point is the (imaginary)time–dependent Schroedinger equation ($t \to i\tau$):

$$-\frac{\partial}{\partial\tau}|\Psi(\tau)\rangle = \hat{H}|\Psi(\tau)\rangle = \left(\hat{K} + \hat{V}\right)|\Psi(\tau)\rangle \tag{1.9}$$

where in the last expression we have explicitly separated the contributions $\hat{K}$ and $\hat{V}$ coming respectively from the kinetic and potential parts of the total Hamiltonian $\hat{H}$. As anticipated in the introduction, we will now recast Eq.

(1.9) into the following integral equation:

$$\begin{aligned}\langle\mu|\Psi(\tau+\Delta\tau)\rangle &= \int d\nu\langle\mu|\hat{G}_{\Delta\tau}|\nu\rangle\langle\nu|\Psi(\tau)\rangle \\ &= \langle\mu|e^{-\Delta\tau\hat{H}}|\Psi(\tau)\rangle\end{aligned} \tag{1.10}$$

where we employed complete sets of states $|\nu\rangle$ and $|\mu\rangle$ for convenience. In the last equation $\hat{G}_{\Delta\tau}$ is the Green's function of equation (1.9), the so–called *imaginary-time propagator*. All eigenvectors of the Schroedinger equation would be solutions of Eq. (1.10), but we can isolate the eigenvector with the lowest eigenvalue $|\Phi_0\rangle$ by looking at the long imaginary–time solution, in fact:

$$\begin{aligned}\lim_{\tau\to\infty}|\Psi(\tau)\rangle &= \lim_{\tau\to\infty} e^{-\tau\hat{H}}|\Psi(0)\rangle \\ &= \lim_{\tau\to\infty}\sum_n e^{-\tau E_n}|\Phi_n\rangle\langle\Phi_n|\Psi(0)\rangle \\ &\to e^{-\tau E_0}|\Phi_0\rangle\langle\Phi_0|\Psi(0)\rangle \propto|\Phi_0\rangle\end{aligned} \tag{1.11}$$

where we have used the complete set of eigenstates of the hamiltonian $|\Phi_n\rangle$, with corresponding eigenvalues $E_n$. The expression in the last line holds provided that the initial condition $|\Psi(0)\rangle$ is not orthogonal to $|\Phi_0\rangle$. In general, the infinite imaginary–time limit will project out the lowest eigenstate that is not orthogonal to $|\Psi(0)\rangle$, this can be used for instance to perform calculations of low-lying excited states with definite symmetry properties.

By repeatedly integrating (1.10), starting from some initial ansatz for the wave-function, we will project to the eigenstate of $\hat{H}$ with the lowest eigenvalue as in the PM algorithm outlined above. An important, tough rather technical point, is the renormalization at step 3. of the Power Method: without it the procedure would be extremely unstable leading eg. to zero–norm results. Preserving the norm of the solution along the projection is thus an essential ingredient for the stability of the method.

In the language used for DMC this renormalization step is applied by means of an iteration–dependent multiplicative factor $\Lambda_k$ attached to the bare propagator that needs to be adjusted to preserve the normalization of the wave–function. In the usual case when the propagator is of exponential form, like in (1.10), this can be casted into an iteration–dependent energy shift $E_{Tk}$:

$$e^{-\tau\hat{H}} \longrightarrow \Lambda_k e^{-\tau\hat{H}} \equiv e^{-\tau(\hat{H}-E_{Tk})}. \tag{1.12}$$

For simplicity of notation, in the following we will use just $E_T$ instead of $E_{Tk}$. From Eq. (1.11) it is also easy to realize that with this choice $E_T \to E_0$ for sufficiently long projection times and we can thus use its average value as an estimate of the ground–state energy, the *growth–estimator*.

The main difficulty in the case of DMC with respect to the Power Method for finite, small matrices is to find an efficient way to compute the action of the imaginary–time propagator on a given state $|\Psi\rangle$. To appreciate better the issue, let us first rewrite the imaginary–time Schroedinger equation (1.9) in a slightly different fashion:

$$\begin{aligned}-\frac{\partial}{\partial\tau}\Psi(\tau,\nu) &= \int d\mu\langle\nu|\hat{H}|\mu\rangle\Psi(\tau,\mu) \\ &= \int d\mu\langle\nu|\hat{H}_T|\mu\rangle\Psi(\tau,\mu) + \langle\nu|\hat{H}_R|\nu\rangle\Psi(\tau,\nu)\end{aligned} \tag{1.13}$$

where in the second line we have explicitly separated the hamiltonian $\hat{H}$ into a part that give rise to transitions $\hat{H}_T$ and another one that acts as a multiplicative operator rescaling the PDF $\hat{H}_R$. Obviously this splitting is basis-dependent, i.e. operators that act as $\hat{H}_T$ in coordinate–space may act as an $\hat{H}_R$ in momentum–space (eg. the kinetic energy).

Correspondingly the master equation (1.10) governing the evolution of the probability distribution $\Psi(\tau, \nu)$ can be conveniently written as:

$$\begin{aligned}\Psi(\tau + \Delta\tau, \nu) &= \int d\mu \langle \nu | G_{\Delta\tau} | \mu \rangle \Psi(\tau, \mu) \\ &= \langle \nu | G^R_{\Delta\tau} | \nu \rangle \int d\mu \langle \nu | G^T_{\Delta\tau} | \mu \rangle \Psi(\tau, \mu) \\ &= G^R_{\Delta\tau}(\nu) \int d\mu \, G^T_{\Delta\tau}(\mu, \nu) \Psi(\tau, \mu).\end{aligned} \tag{1.14}$$

Given a choice of basis, and consequent splitting in $\hat{H}_T$ and $\hat{H}_R$, we can integrate the evolution equation using for instance the Metropolis acceptance/rejection scheme explained before. Starting with a given configuration $|\mu\rangle$ we propose a new move according to some transition probability $T(\mu \to \nu)$, use the MRT test (cf. Eq. 1.5) on $G^T_{\Delta\tau}(\mu, \nu)$ with acceptance probability

$$A(\mu \to \nu) = min\left[1, \frac{T(\nu \to \mu) G^T_{\Delta\tau}(\mu, \nu)}{T(\mu \to \nu) G^T_{\Delta\tau}(\nu, \mu)}\right] \tag{1.15}$$

and attach a weight $G^R_{\Delta\tau}(\nu)$ on the proposed new configuration. If the fluctuations of these weights are not too strong it may be sufficient to preserve the weights along the entire random–walk by accumulating them from one step to the next. This approach is however usually impractical since expectation values calculated along the walk will be dominated by the few walkers with the bigger weights, wasting most of the computing power. A better approach is instead to interpret $G^R_{\Delta\tau}(\nu)$ as a survival, or *branching*, probability. There are different ways of implementing this idea, the most popular one is to choose to work with walkers with weight $w \equiv 1$: after the propagation and the measure of observables, the j–th walker with weight $w_j$ is replicated $n_j = int(w_j + \xi)$ times, where $\xi$ is a uniformly distributed random number in $(0, 1)$. The total number of walkers present in the population will keep changing during the evolution and its average dimension is set by properly tuning the energy shift $E_T$.

The Metropolis step is extremely useful since it can be applied to a variety of $\hat{H}_T$ at the price to have low acceptance rates for poor choices of the auxiliary probability $T$. This can be avoided, obtaining an acceptance rate of 100%, if we are capable of sampling directly from the transition probability $G^T_{\Delta\tau}(\mu, \nu)$. This will be for instance the case for the CIMC algorithm described later in this work.

In any case, provided that we generate the appropriate stochastic process defined by the one–step evolution (1.14), the steady–state distribution would be correctly $P_\infty(\nu) = \Phi_0(\nu)$ from which we may calculate observables. The

expression for the ground state energy will be:

$$\begin{aligned} E_0 &= \lim_{\tau\to\infty} \frac{\langle\Psi_I|\hat{H}e^{-\tau\hat{H}}|\Psi_I\rangle}{\langle\Psi_I|e^{-\tau\hat{H}}|\Psi_I\rangle} = \frac{\langle\Psi_I|\hat{H}|\Psi(\tau)\rangle}{\langle\Psi_I|\Psi(\tau)\rangle} \\ &= \frac{\mathbb{E}_{\Phi_0}\left[\Psi_I(\mathbf{X})E_L(\mathbf{X})\right]}{\mathbb{E}_{\Phi_0}\left[\Psi_I(\mathbf{X})\right]} \end{aligned} \tag{1.16}$$

where $\Psi_I \equiv \Psi(\tau = 0)$ and we have defined the local–energy $E_L$ in some configuration $|\mu\rangle$ as:

$$E_L(\mu) = \frac{\langle\mu|H|\Psi_I\rangle}{\langle\mu|\Psi_I\rangle}. \tag{1.17}$$

The corresponding sample estimator will then be:

$$\widetilde{E}_0 = \frac{\sum_i^M E_L(X_i)\Psi_I(X_i)}{\sum_i^M \Psi_I(X_i)}. \tag{1.18}$$

The same procedure can be carried out for general operators

$$\begin{aligned} O_{DMC} &= \frac{\langle\Psi_I|O|\Phi_0\rangle}{\langle\Psi_I|\Phi_0\rangle} \\ &\longrightarrow \widetilde{O}_{DMC} = \frac{\sum_i^M O_L(X_i)\Psi_I(X_i)}{\sum_i^M \Psi_I(X_i)}. \end{aligned} \tag{1.19}$$

We note that (1.19) will be exact only for observables that commute with the hamiltonian, otherwise it will not be the wanted expectation value but a *mixed–estimator* of it. This estimator will have a bias that depends on how much different is the trial function $\Psi_I$ with respect to the ground state $\Phi_0$, this bias will be however smaller than the variational estimate (1.3). There are ways to partially circumvent this within DMC using *extrapolated estimators* or techniques such as *forward–walking* [48, 49, 50, 51].

### Efficiency issues and Fermions

The separation carried out before Eq. (1.13) is useful also because we need different conditions on $\hat{H}_R$ and $\hat{H}_T$ to have an efficient algorithm:

- the transition to new states governed by $\hat{H}_T$ should be implementable in an efficient way
- the values of the rescaling factor given by $\hat{H}_R$ should not fluctuate too much during the evolution (ie. it has to have a finite variance)

Clearly these conditions depend strongly on the chosen basis, but there are general–purpose techniques that can help for both, one of them being Importance Sampling (IS) which is more extensively presented in Appendix A. Given the target hamiltonian $\hat{H}$ and an auxiliary, for now indeterminate, state $|\Phi_G\rangle$ we can consider the following similarity transformation:

$$\langle\nu|\hat{H}|\mu\rangle \longrightarrow \Phi_G(\nu)\langle\nu|\hat{H}|\mu\rangle\Phi_G^{-1}(\mu) \equiv \langle\nu|H_{IS}|\mu\rangle \tag{1.20}$$

where we have now supposed that $\Phi_G(\nu) \neq 0\ \forall\nu$.

The spectrum of both hamiltonians will be the same but, with a proper choice of the auxiliary state $|\Phi_G\rangle$, the similarity–transformed one can be much more easy to deal with. Consider for now the long imaginary–time behavior attained by using the propagator of $\hat{H}_{IS}$ for the evolution:

$$\begin{aligned}\lim_{\tau\to\infty}\Psi_{IS}(\tau,\nu) &= \lim_{\tau\to\infty}\langle\nu|e^{-\tau\hat{H}_{IS}}|\Psi(0)\rangle \\ &= \lim_{\tau\to\infty}\sum_n e^{-\tau E_n}\langle\Phi_n|\Psi(0)\rangle\Phi_n(\nu)\Phi_G(\nu) \\ &\to e^{-\tau E_0}\langle\Phi_0|\Psi(0)\rangle\Phi_0(\nu)\Phi_G(\nu)\propto\Phi_0(\nu)\Phi_G(\nu)\end{aligned} \tag{1.21}$$

we see then that the asymptotically sampled distribution will be the product $P_\infty(\nu)=\Phi_0(\nu)\Phi_G(\nu)$. We recognize that if we choose $\Phi_G\equiv\Phi_0$ this method reduces to a VMC calculation on the true ground–state distribution $\Phi_0^2$ (cf. Eq. 1.3).

The single step evolution with importance sampling becomes then:

$$\begin{aligned}\Psi(\tau+\Delta\tau,\nu) &= \int d\mu\langle\nu|G_{\Delta\tau}|\mu\rangle\frac{\Phi_G(\nu)}{\Phi_G(\mu)}\Psi(\tau,\mu) \\ &= \int d\mu\langle\nu|G^{IS}_{\Delta\tau}|\mu\rangle\Psi(\tau,\mu)\end{aligned} \tag{1.22}$$

and we see that the transition to the new state in $\nu$ is now weighted with a factor $w_{IS}(\nu,\mu)=\Phi_G(\nu)/\Phi_G(\mu)$. It's main effect is to define a privileged direction for the transitions: propagation towards states that enhance the weight $w_{IS}$ will be favored while the probability to go in states that diminish this weight will be lowered.

It is easy too see that in the limit $\Phi_G\to\Phi_0$ we will gain a lot in efficiency since the random walk will be pushed towards regions where $\Phi_0$ is big. This helps us in increasing the efficiency of the transitions governed by the off–diagonal part of the $\hat{H}_T$ hamiltonian. It usually also helps in lowering the variance of the reweight factor generated by $\hat{H}_R$ since, in general, this weight is $\approx$ constant in region where $\Phi_0$ is big, but to elaborate on that we need to specialize the discussion to a particular basis as we will do in the next chapters.

However, IS not only helps in lowering variances, it may allow us to perform simulations even in cases where naively we would think to have no chance. Consider for instance the situation where

$$\langle\nu|G_{\Delta\tau}|\mu\rangle<0 \qquad \text{for some} \qquad \mu,\nu \tag{1.23}$$

and so it cannot be interpreted as a PDF itself. With a proper choice of $\Phi_I$ we may have

$$\langle\nu|G^{IS}_{\Delta\tau}|\mu\rangle>0 \tag{1.24}$$

in those points. Unfortunately cases like (1.23) are not very rare, on the contrary we will be in that situation in almost all calculations involving fermions (with few notable exceptions) due to the Pauli statistics that forces the wave–function to change sign under the action of the permutation group $S_N$. This is the source of the infamous *fermion sign–problem*. However, it is unlikely that we will be able to find some state $\Psi_G$ for which $\langle\nu|G^{IS}_{\Delta\tau}|\mu\rangle>0$ in the whole Hilbert space and one usually constrains the random–walk in regions where Eq. 1.24 is fulfilled.

This procedure is known in literature as the *fixed–node approximation* and its impact can be controlled by the quality of the guiding state $\Psi_G$.

Before going to the next algorithm we report the expressions for the energy and for the observables in the case where Importance Sampling is employed. The ground–state energy will now be:

$$E_0 = \frac{\mathbb{E}_{\Phi_0\Phi_G}\left[\frac{\Psi_I(\mathbf{X})}{\Psi_G(\mathbf{X})}E_L(\mathbf{X})\right]}{\mathbb{E}_{\Phi_0\Phi_G}\left[\frac{\Psi_I(\mathbf{X})}{\Psi_G(\mathbf{X})}\right]} \tag{1.25}$$

and we will have the following sample estimator:

$$\widetilde{E}_0 = \frac{\sum_i^M E_L(X_i)\frac{\Psi_I(X_i)}{\Phi_G(X_i)}}{\sum_i^M \frac{\Psi_I(X_i)}{\Phi_G(X_i)}} \tag{1.26}$$

with the local–energy as defined before. Analogously for a general observable:

$$\widetilde{O}_{DMC} = \frac{\sum_i^M O_L(X_i)\frac{\Psi_I(X_i)}{\Phi_G(X_i)}}{\sum_i^M \frac{\Psi_I(X_i)}{\Phi_G(X_i)}}. \tag{1.27}$$

In the particular case where the trial and guiding wave–functions are the dame $\Psi_I \equiv \Phi_G$ we find the simplified expressions

$$\widetilde{E}_0 = \frac{1}{M}\sum_i^M E_L(X_i) \tag{1.28}$$

and

$$\widetilde{O}_{DMC} = \frac{1}{M}\sum_i^M O_L(X_i). \tag{1.29}$$

Further developments along these lines require some knowledge of the basis actually used in the calculation and will be explored when relevant.

### 1.2.2 Reptation Monte Carlo (RMC)

Reptation Monte Carlo (RMC) is another Projection Monte Carlo method based on a path–integral representation of the imaginary time projector. We start by choosing an imaginary–time interval (or inverse *temperature*) $\beta$, big enough that we can assume convergence to the ground–state so that:

$$\begin{aligned} Z(\beta) &= \langle\Psi_I|\Psi_0\rangle \\ &= \langle\Psi_I|e^{-\beta\hat{H}}|\Psi_I\rangle \end{aligned} \tag{1.30}$$

for some appropriate initial trial–state $\Psi_I$. Inserting identities using a complete basis $1 = \int d\mu|\mu\rangle\langle\mu|$ we can decompose (1.30) into $K$ slices:

$$\begin{aligned} Z(\beta) &= \langle\Psi_I|\int d\mu_0|\mu_0\rangle\langle\mu_0|e^{-\beta\hat{H}}\int d\mu_K|\mu_K\rangle\langle\mu_K|\Psi_I\rangle \\ &= \int d\mu_0\ldots d\mu_K\langle\Psi_I|\mu_0\rangle\langle\mu_0|e^{-\frac{\beta}{K}\hat{H}}|\mu_1\rangle\langle\mu_1|\ldots|\mu_{K-1}\rangle\langle\mu_{K-1}|e^{-\frac{\beta}{K}\hat{H}}|\mu_K\rangle\langle\mu_K|\Psi_I\rangle \\ &= \int d\mu_0\ldots d\mu_K\Psi_I(\mu_0)\langle\mu_0|G_{\Delta\tau}|\mu_1\rangle\langle\mu_1|\ldots|\mu_{K-1}\rangle\langle\mu_{K-1}|G_{\Delta\tau}|\mu_K\rangle\Psi_I(\mu_K) \end{aligned} \tag{1.31}$$

where $G_{\Delta\tau}$ the same Green's function defined in (1.10) and $\Delta\tau \equiv \beta/K$. The quantity $Z(\beta)$ is then interpreted as partition function, and imaginary–time *paths* $\mathcal{X} = \{\mu_o, \ldots, \mu_K\}$ are given the normalized probability:

$$\Pi[\mathcal{X}] = \frac{\Psi_I(\mu_0)\langle\mu_0|G_{\Delta\tau}|\mu_1\rangle\langle\mu_1|\ldots|\mu_{K-1}\rangle\langle\mu_{K-1}|G_{\Delta\tau}|\mu_K\rangle\Psi_I(\mu_K)}{\int d\mu_0 \ldots d\mu_K \Psi_I(\mu_0)\langle\mu_0|G_{\Delta\tau}|\mu_1\rangle\langle\mu_1|\ldots|\mu_{K-1}\rangle\langle\mu_{K-1}|G_{\Delta\tau}|\mu_K\rangle\Psi_I(\mu_K)}. \tag{1.32}$$

We may also introduce a path–action $S[\mathcal{X}]$ and write simply:

$$\Pi[\mathcal{X}] = \frac{e^{-S[\mathcal{X}]}}{Z(\beta)}. \tag{1.33}$$

There are many ways for sampling such imaginary–time paths $\mathcal{X}$ using Markov Chain Monte Carlo techniques with MRT sampling. Given an initial path $\mathcal{X}$, a new one $\mathcal{Y}$ is proposed according to some probability $T(\mathcal{X} \to \mathcal{Y})$ and the move is then accepted/rejected according to the Metropolis probability

$$A(\mathcal{X} \to \mathcal{Y}) = min\left[1, \frac{T(\mathcal{Y} \to \mathcal{X})\Pi[\mathcal{Y}]}{T(\mathcal{X} \to \mathcal{Y})\Pi[\mathcal{X}]}\right]. \tag{1.34}$$

The versatility of this method comes from the relatively large freedom in the choice of the proposal probability $T(\mathcal{X} \to \mathcal{Y})$, also enlarged by the possibility of using the importance sampled propagator (1.22) with $\Phi_g \equiv \Psi_I$ to obtain equivalent expressions shifting the $\Psi_I$ along the path. In the original algorithm [52] for instance, one proceeds by taking in initial path $\mathcal{X}$ and then chooses at random a growth direction. This defines a *head* slice and a *tail* slice of the path. A number $\delta$ of slices are then added to the *head* and removed from the *tail* generating a new path $\mathcal{Y}$. The generation of the new slice is performed sampling $\delta$ steps directly from the Green's function $G_{\Delta\tau}(\mu, \nu)$ (or its IS equivalent). This "reptile"–like movement of the path, which simplifies the calculation of the ratios in (1.34) together as giving a reasonable acceptance rate, has given the name to Reptation MC. We will explore some slight variations of this sampling method when we will implement it in coordinate–space later on.

The appealing properties of RMC are the fact that it allows to have access to the ground–state energy with an accuracy comparable to DMC while at the same time allowing for the exact evaluation of other observables. Lets consider for instance the expression for the total energy obtained on a random walk starting at $|\Psi(\tau = 0)\rangle = |\Psi_I\rangle$ after a total propagation time $\beta$:

$$\begin{aligned} E(\beta) &= \frac{\langle\Psi_I|\hat{H}e^{-\tau\hat{H}}|\Psi_I\rangle}{\langle\Psi_I|e^{-\tau\hat{H}}|\Psi_I\rangle} = \frac{\langle\Psi_I|\hat{H}|\Psi(\tau)\rangle}{\langle\Psi_I|\Psi(\tau)\rangle} \\ &= \frac{\langle\Psi_I|e^{-\frac{\beta}{2}\hat{H}}\hat{H}e^{-\frac{\beta}{2}\hat{H}}|\Psi_I\rangle}{\langle\Psi_I|e^{-\beta\hat{H}}|\Psi_I\rangle} = \frac{\langle\Psi(\beta/2)|\hat{H}|\Psi(\beta/2)\rangle}{\langle\Psi(\beta/2)|\Psi(\beta/2)\rangle} \end{aligned} \tag{1.35}$$

The expression in the first line is the usual *mixed* DMC expression for the energy (1.16), where the imaginary–time evolution is carried on the rightmost state, while the second one is the RMC version where the evolution is performed for both of them. For the energy these expressions are equivalent but not for a general observable, as we have already noted before. Using the path–representation

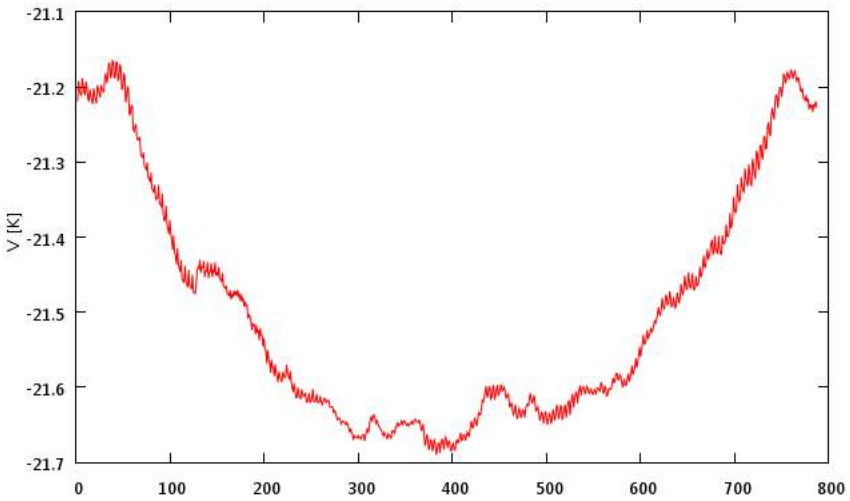


Figure 1.1: Potential energy along a $K = 800$ slices-long imaginary-time path (from [53] )

we can calculate *pure* estimators for general operators by measuring in the central slice of the path:

$$O(\beta) = \frac{\langle \Psi_I | e^{-\frac{\beta}{2}\hat{H}} \hat{O} e^{-\frac{\beta}{2}\hat{H}} | \Psi_I \rangle}{\langle \Psi_I | e^{-\beta\hat{H}} | \Psi_I \rangle} = \frac{\langle \Psi(\beta/2) | \hat{O} | \Psi(\beta/2) \rangle}{\langle \Psi(\beta/2) | \Psi(\beta/2) \rangle} \xrightarrow{\beta\to\infty} \frac{\langle \Psi_0 | \hat{O} | \Psi_0 \rangle}{\langle \Psi_0 | \Psi_0 \rangle} \tag{1.36}$$

and then use the following estimator:

$$\tilde{O} = \frac{1}{M} \sum_{i}^{M} O_L(X^i_{K/2}) \tag{1.37}$$

where with the notation $X^i_m$ we indicate the $m$–th slice of the $i$–th path $\mathcal{X}_i$ sampled and in the last line we have assumed to using the importance– sampled Green's function for the sampling with $\Psi_G \equiv \Psi_I$ (so that the denominator is $\equiv 1$). The average value of the observable $O$, if we measure it away from the center, will converge to its mixed–estimator value at both the endpoints of the path. In Fig.1.1 we see for instance the expectation value of the potential operator along a $K = 800$ slices for a bulk system of superfluid $He^4$ going from its mixed value at the edges to the exact value in the middle. Note that the curvature has not to be always positive due to the fact that the mixed–estimator does not satisfy any variational principle $O_{mix} \geq O_0$ (contrary to the energy).

RMC is also a natural framework for computing imaginary–time correlation

functions:

$$\begin{aligned} C_O(\tau;\beta) &= \frac{\langle \Psi_I | e^{-\frac{\beta}{2}\hat{H}} \hat{O} e^{-\tau \hat{H}} \hat{O} e^{-\frac{\beta}{2}\hat{H}} | \Psi_I \rangle}{\langle \Psi_I | e^{-\beta \hat{H}} | \Psi_I \rangle} \\ &= \frac{\langle \Psi(\beta/2) | \hat{O} e^{-\tau \hat{H}} \hat{O} | \Psi(\beta/2) \rangle}{\langle \Psi(\beta/2) | \Psi(\beta/2) \rangle} \\ &\xrightarrow{\beta \to \infty} \frac{\langle \Psi_0 | \hat{O} e^{-\tau \hat{H}} \hat{O} | \Psi_0 \rangle}{\langle \Psi_0 | \Psi_0 \rangle} = \frac{\langle \Psi_0 | \hat{O}(0) \hat{O}(\tau) | \Psi_0 \rangle}{\langle \Psi_0 | \Psi_0 \rangle} \end{aligned} \tag{1.38}$$

where the time–dependence in the last expression is in the Heisenberg picture. In order to estimate this quantity we can consider longer paths composed by $P = K + Q$ time slices with $Q = \tau/\Delta\tau$ and evaluate the operators in two slices separated by an interval $Q$:

$$\widetilde{C_O}\,(\tau = Q\Delta\tau) = \frac{1}{M} \sum_i^M O_L(X^i_{K/2}) O_L(X^i_{K/2+Q}). \tag{1.39}$$

In the last expression we kept the observables in the innermost part of the "snake" in order to minimize the effects coming from the necessary use of the importance function $\Psi_I$.

In the next chapters we will focus on two implementations of the general algorithms exposed so far: we will show how it is possible to carry Diffusion Monte Carlo for fermions in a Slater–Determinant space and discuss Reptation Monte Carlo for bosonic systems in coordinate–space.

# Chapter 2

# DMC in Slater–Determinant space

The great success of Quantum Monte Carlo for fermionic systems (employing the fixed–node prescription) is largely because of the development of high–quality trial wave functions. However, most of these wave functions have forms which are convenient only for calculations in coordinate–space. The lack of accurate and computationally efficient trial ground-state wave functions has, thus far, precluded a wide exploration of these algorithms within the configuration interaction (CI) scheme (see, however, [54]). Generally, QMC methods within the CI scheme tend to rely on auxiliary fields introduced via the Hubbard–Stratonovich transformation [55, 56, 57, 58, 59]. Much recent interest, however, was sparked by the demonstration that even within the CI scheme it is possible to apply stochastic projection to systems much larger than what would be possible using conventional matrix diagonalization [60]. And moreover, working in CI–space allows the development of exciting hybrid algorithms like the Semistochastic Quantum Monte Carlo [61] that combines exact diagonalization in a restricted sub–space with stochastic projection trough Monte Carlo.

In this chapter we present the details of our implementation of Diffusion Monte Carlo in a CI–space, the Configuration Interaction Monte Carlo (CIMC), presenting also some first applications.

## 2.1 Random walk on a Fock–space

Let us take a finite set $\mathcal{S}$ of sp states of size $\mathcal{N}_s$ and consider a general second–quantized fermionic Hamiltonian which includes two and possibly many–body interactions

$$H = \sum_{i\epsilon\mathcal{S}} \epsilon_i a_i^\dagger a_i + \sum_{abij\epsilon\mathcal{S}} V_{ij}^{ab} a_a^\dagger a_b^\dagger a_i a_j + \dots \,, \tag{2.1}$$

where $a_i^\dagger$ creates a particle in the single-particle (sp) state labeled by $i$ ($i$ is a collective label for all sp quantum numbers) and the $V_{ij}^{ab}$ are general (anti–symmetrized) two-body interaction matrix elements:

$$V_{ij}^{ab} = \langle ij|\hat{V}|ab\rangle - \langle ij|\hat{V}|ba\rangle \equiv \langle ij\|ab\rangle. \tag{2.2}$$

The resulting many–body Hilbert space would be spanned by the full set of $N$–particle Slater determinants that can be generated using the sp orbitals $i \in \mathcal{S}$. We will denote these Slater–determinants in the occupation number basis by $|\mathbf{n}\rangle$, where $\mathbf{n} \equiv \{n_i\}$ and $n_i = 0, 1$ are occupation number of the single–particle state $i$. In this Hilbert space we can express the one–time step evolution as

$$\Psi_{\tau+\Delta\tau}(\mathbf{m}) = \sum_{\mathbf{n}} \langle \mathbf{m}|\hat{P}|\mathbf{n}\rangle \Psi_{\tau}(\mathbf{n}) \tag{2.3}$$

where $\Psi_\tau(\mathbf{n}) \equiv \langle \mathbf{n}|\Psi_\tau\rangle$ is the representation of the wave–function in this basis. Our goal is to perform the evolution in Eq.(2.3) in a stochastic way. In order to do this, let us first split the matrix elements of $\hat{P}$ as follows

$$\langle \mathbf{m}|\hat{P}|\mathbf{n}\rangle = p(\mathbf{m}, \mathbf{n}) g(\mathbf{n}) \tag{2.4}$$

with

$$g(\mathbf{n}) = \sum_{\mathbf{m}} \langle \mathbf{m}|\hat{P}|\mathbf{n}\rangle \tag{2.5}$$

and

$$p(\mathbf{m}, \mathbf{n}) = \frac{\langle \mathbf{m}|\hat{P}|\mathbf{n}\rangle}{\sum_{\mathbf{m}} \langle \mathbf{m}|\hat{P}|\mathbf{n}\rangle} \tag{2.6}$$

.

Now if the matrix elements $\langle \mathbf{m}|\hat{P}|\mathbf{n}\rangle \geq 0$ we can interpret $p(\mathbf{m}, \mathbf{n})$ for fixed $\mathbf{n}$ as (normalized) probabilities and $g(\mathbf{n})$ as a weight factor. This is analogous to what happened in conventional coordinate–space formulations where the propagator is splitted into an off–diagonal part times a weight factor.

Imagine that at a given imaginary–time $\tau$ the wave–function $\Psi_\tau$ is non–negative in configuration space (ie. $\Psi_\tau(\mathbf{n}) \geq 0$), then we can represent it as an ensemble of configurations. Due to the non–negativity of the matrix elements of $P$, we also have that the evolution described in Eq.(2.3) preserves the signs, ie. $\Psi_{\tau+\Delta\tau}(\mathbf{m}) \geq 0 \ \forall \mathbf{m}$. This suggests the following procedure for the imaginary–time evolution: given the current configuration $\mathbf{n}$ a new configuration $\mathbf{m}$ is chosen from the probability distribution $p(\mathbf{m}, \mathbf{n})$ and its weight gets multiplied by $g(\mathbf{n})$. In order to improve efficiency the latter is usually substituted with a *branching* step where the new configuration in $\mathbf{m}$ is replicated according to the integer value of its weight.

In practice one has to choose some form for the evolution operator that appears in Eq.(2.3), a common choice in discrete spaces is the following

$$\begin{aligned} \langle \mathbf{m}|\hat{P}|\mathbf{n}\rangle &= \langle \mathbf{m}|1 - \Delta\tau\left(\hat{H} - E_T\right)|\mathbf{n}\rangle \\ &= \delta_{\mathbf{m},\mathbf{n}} - \Delta\tau \langle \mathbf{m}|H - E_T|\mathbf{n}\rangle \end{aligned} \tag{2.7}$$

where $E_T$ is the energy shift used in the simulation to preserve the norm of the solution. Convergence to the ground–state

$$|\Psi_{gs}\rangle = \lim_{M\to\infty} \hat{P}^M |\Psi_0\rangle \tag{2.8}$$

is guaranteed provided that the eigenvalues of $\hat{P}$ lie between $-1$ and 1. This translates into a condition on the imaginary–time step $\Delta\tau$ which has to satisfy $\Delta\tau < 2/(E_{max} - E_T)$ where $E_{max}$ is the maximum eigenvalue of $\hat{H}$ in our finite

basis. This upper bound becomes tighter and tighter as we increase the number of particle $N$ and/or the number of sp–states $\mathcal{N}_s$ and as a consequence the number $M$ of iterations needed for convergence to the ground state increases dramatically. In CIMC we deal with this problem by employing a different algorithm proposed in [62] (see also [63, 64] ) and that allows us to sample from the exponential propagator

$$\langle \mathbf{m}|\hat{P}|\mathbf{n}\rangle = \langle \mathbf{m}|e^{-\Delta\tau(\hat{H}-E_T)}|\mathbf{n}\rangle \tag{2.9}$$

without any limitation on the choice of the imaginary time step $\Delta\tau$. We leave the discussion of its details in Appendix D.

Necessary condition for the applicability of the algorithm discussed so far is that the matrix elements of $\hat{P}$ in configuration space are positive, in general however $\hat{P}$ will have negative–matrix elements which will cause problems, this is once again a manifestation of the sign–problem.

In principle, one can still produce a stochastic evolution absorbing the signs into the renormalization factor and sampling off-diagonal moves using the absolute value $\left|\langle \mathbf{m}|\hat{P}|\mathbf{n}\rangle\right|$, but this is accompanied by an exponential decay of the signal to noise ratio as a function of the total projection time $\tau = M\Delta\tau$. Recently it was shown that by employing an annihilation step in the evolution this problem can be substantially alleviated [23, 60, 61]. At the end however these algorithms have still an exponential scaling with system–size, though with a reduced exponent.

## 2.2 Importance–sampling and sign–problem

In CIMC we instead deal with the sign–problem in a way which is somewhat similar to standard coordinate–space QMC: we will use an initial ansatz $\Phi_T$ for the ground–state wave–function and use that to constrain the random walk in a region of the many–body Hilbert space where $\langle \mathbf{m}|\hat{P}|\mathbf{n}\rangle \geq 0$ is satisfied. In order for this scheme to be practical one needs a systematic way for reducing the bias coming from this approximation, e.g. we want the bias to go to zero as the ansatz $\Phi_T$ tends towards the ground–state $\Psi_0$. That's exactly what is done in coordinate-space fixed–node QMC simulations.

In this derivation we will follow the work in [63, 64] and generalize it to the case of complex–hermitian hamiltonians. First a comment is necessary due to the fact that the trial–wave function will now have both a real and imaginary part and in principle we should evolve both according to their evolution equation, in this work however we choose to work in the so–called *fixed–phase* approximation where the imaginary part of the solution is constrained to be the same as that of the trial wave–function, ie. $\Re[\Psi^*(\mathbf{n})\Phi_T(\mathbf{n})] = 0$ for every distribution $\Psi(\mathbf{n})$ sampled in the random walk.

We can now define for any configurations $\mathbf{n}$ and $\mathbf{m}$ for which the trial state $\Phi_T$is non–zero the following quantity:

$$\begin{aligned} \mathfrak{s}_{\mathbf{mn}} &= \text{sign}\, \Re\left[\Phi_T^*(\mathbf{m}) H_{\mathbf{mn}} \Phi_T^*(\mathbf{n})^{-1}\right] \\ &= \text{sign}\, \frac{\Re\left[\Phi_T^*(\mathbf{m}) H_{\mathbf{mn}} \Phi_T(\mathbf{n})\right]}{|\Phi_T(\mathbf{n})|^2} = \mathfrak{s}_{\mathbf{nm}} \end{aligned} \tag{2.10}$$

where $\Re$ stands for the real part and $^*$ is complex–conjugation.

We will now define a one–parameter family of Hamiltonians $\hat{\mathcal{H}}_\gamma$, defined over configurations $\mathbf{n}$ such that $|\Phi_T(\mathbf{n})| \neq 0$, with off–diagonal matrix elements given by

$$\langle \mathbf{m}|\hat{\mathcal{H}}_\gamma|\mathbf{n}\rangle = \begin{cases} -\gamma\langle \mathbf{m}|\hat{H}|\mathbf{n}\rangle & \mathfrak{s}(\mathbf{m},\mathbf{n}) > 0 \\ \langle \mathbf{m}|\hat{H}|\mathbf{n}\rangle & \text{otherwise} \end{cases} , \tag{2.11}$$

while the diagonal terms are

$$\begin{aligned} \langle \mathbf{n}|\hat{\mathcal{H}}_\gamma|\mathbf{n}\rangle &= \langle \mathbf{n}|\hat{\mathcal{H}}|\mathbf{n}\rangle + (1+\gamma) \sum_{\substack{\mathbf{m}\neq\mathbf{n} \\ \mathfrak{s}(\mathbf{m},\mathbf{n})>0}} \mathfrak{s}(\mathbf{m},\mathbf{n}) \\ &= \langle \mathbf{n}|\hat{H}|\mathbf{n}\rangle + \sum_{\mathbf{m}} h_{\mathbf{mn}} \end{aligned} \tag{2.12}$$

.

Note that $\hat{\mathcal{H}}_{\gamma=-1} \equiv \hat{H}$. We now coherently define a family of propagators $\hat{\mathcal{P}}_\gamma$ by

$$\langle \mathbf{m}|\hat{\mathcal{P}}_\gamma|\mathbf{n}\rangle = \delta_{\mathbf{m},\mathbf{n}} - \Delta\tau \frac{\Re\left[\Phi_T^*(\mathbf{m})\langle \mathbf{m}|\hat{\mathcal{H}}_\gamma - E_T|\mathbf{n}\rangle\Phi_T(\mathbf{n})\right]}{|\Phi_T(\mathbf{n})|^2} . \tag{2.13}$$

we see directly that for any $\gamma \geq 0$ we have $\langle \mathbf{m}|\mathcal{P}|\mathbf{n}\rangle \geq 0$ and so the propagator $\mathcal{P}$ is, by construction, free from the sign–problem and performing the corresponding random–walk allows us to filter the state $\Phi_T(\mathbf{n})\phi_\gamma^0(\mathbf{n})$, where now $\phi_\gamma^0(\mathbf{n})$ is the ground–state of the hamiltonian $\mathcal{H}_\gamma$. The ground–state energy $E_\gamma$ obtained following this procedure is a strict upper bound for the true ground–state energy $E_{gs}$ of the true hamiltonian $H$ and, moreover, this upper bound is tighter than the variational upper–bound provided by $\langle \Phi_T|\hat{H}|\Phi_T\rangle$ (the proofs are left to Appendix B).

Furthermore, any linear extrapolation of $E_\gamma$ from any two values $\gamma \geq 0$ to $\gamma = -1$ (which would correspond to the original hamiltonian) also provides an upper–bound on $E_{gs}$ that is usually tighter than the individual $E_\gamma$'s. We found that a good compromise between the tightness of the upper–bound and the statistical noise in the extrapolation is to choose two values: $\gamma = 0$ and $\gamma = 1$. Thus the energy estimator used throughout this work will be

$$E_{CIMC} = 2E_{\gamma=0} - E_{\gamma=1} \tag{2.14}$$

Finally, to assure the success of the proposed method a good choice for the importance function $|\Phi_T\rangle$ is crucial: we need a wave–function flexible enough to account for the relevant correlations in the system and that at the same time can be evaluated sufficiently quickly on a computer. In many strongly–interacting systems Coupled–Cluster theory provide an ansatz that fulfills the first criterion and in the next section we will show how to evaluate it efficiently.

### 2.2.1 Coupled–Cluster wave–functions

The Coupled–Cluster ansatz for the ground–state wave–function is usually expressed as follows:

$$|CC\rangle = e^{\hat{T}}|MF\rangle \tag{2.15}$$

where $|MF\rangle$ is a mean–field solution (eg. Hartree–Fock) while $\hat{T}$ is an excitation operator expressed as a sum of 1particle–1hole excitations ($\hat{T}_1$), 2particle–2hole excitations ($\hat{T}_2$) and so on. In terms of single–particle creation and annihilation operators we can rewrite the excitations as follows

$$T_1 = \sum_{ia} t_i^a a_a^\dagger a_i \tag{2.16}$$

$$T_2 = \frac{1}{4} \sum_{ijab} t_{ij}^{ab} a_a^\dagger a_b^\dagger a_j a_i \tag{2.17}$$

and so on. In these expression and in the rest of the work indices *i,j,k,l,...* represent occupied states in the reference state $|MF\rangle$ and indices *a,b,c,d,...* represent unoccupied states. The amplitudes $t_i^a, t_{ij}^{ab}, \ldots$ are the coefficients of the wave–function that need to be determined.

If we consider all excitation operators up to the maximum one $\hat{T}_N$ we recover the exact full Configuration Interaction solution, which has however a computational cost that scales exponentially in the system size. The key feature of the Coupled–Cluster formulation is that it allows for robust approximations, one can in fact prove that the wave–function resulting in any truncation in the expansion of $\hat{T}$ gives a size–consistent approximation to the ground–state properties. This allows accurate calculations to be performed in polynomial time and for systems far beyond the reach of the exact full diagonalization.

In this work we will concentrate on bulk systems where 1particle–1hole excitations are zero because of momentum conservation and thus consider the so–called coupled cluster doubles (CCD) approximation which corresponds to consider $\hat{T} \equiv \hat{T}_2$. In this case the CC correction to the energy takes the form

$$\Delta E_{CCD} = \sum_{i<j} \sum_{a<b} \langle ij||ab\rangle \, t_{ij}^{ab}, \tag{2.18}$$

while the equations to be solved for the amplitudes are given by (see eg. [6]):

$$\langle \Phi_{ij}^{ab}|\hat{H}\left(1 + \hat{T}_2 + \frac{1}{2}\hat{T}_2^2\right)|MF\rangle = \Delta E_{CCD} t_{ij}^{ab}, \tag{2.19}$$

where the pair–excited state $|\Phi_{ij}^{ab}\rangle$ is given by:

$$|\Phi_{ij}^{ab}\rangle = a_a^\dagger a_b^\dagger a_j a_i |MF\rangle \tag{2.20}$$

.

Now that we have the amplitudes we also have to evaluate the wave–function fast enough in configuration space in order to be an effective choice for $\Phi_T$. In [65] we showed how to evaluate the overlaps $\langle \mathbf{n}|\Phi_T\rangle$ in a computationally efficient way in the doubles (CCD) approximation. The idea works as follows: imagine you want to compute the amplitude of the CCD wave–function on a particular determinant $\mathbf{m} \equiv a_{p_1}^\dagger \ldots a_{p_m}^\dagger a_{h_1} \ldots a_{h_m} |\Phi_{\mathrm{MF}}\rangle$ containing $M$particle–$M$hole excitations, this amplitude can be expressed as a superposition of 2particle–2hole excitations acting on the all possible $(M-2)$particle–$(M-2)$holes that can be generated from $\mathbf{m}$. This process can be pursued up to the 0particle–0hole state

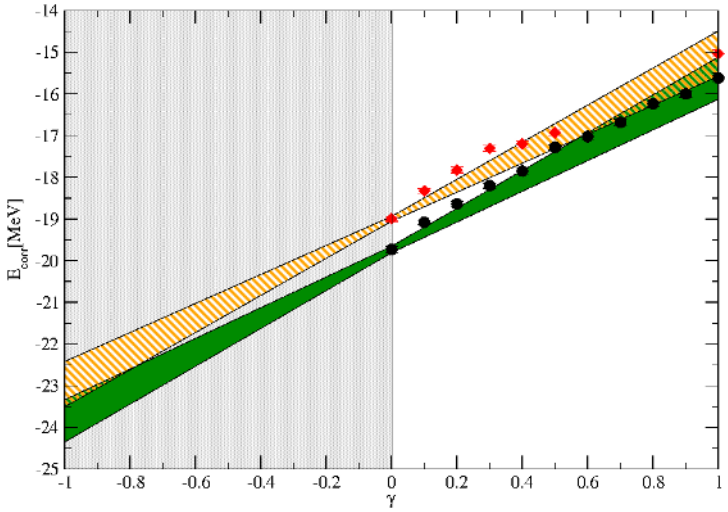


Figure 2.1: Extrapolations of CIMC correlation energies in the $\gamma$ parameter for a system of $N = 14$ neutrons interacting trough chiral NNLO$_{opt}$ interaction. Black circles data were obtained using a Coupled–Cluster type wave–function with amplitudes calculated from PT2 while for the red diamonds we added a stochastic component to the amplitudes (cf. Eq.(2.23)).

$|MF\rangle$ and we obtain the following recursive relation (see Appendix C for details)

$$\Phi^M_{\rm CCD}\left(\begin{smallmatrix} p_1 p_2 \cdots p_M \\ h_1 h_2 \cdots h_M \end{smallmatrix}\right) = \langle \mathbf{m} | \Phi_{\rm CCD} \rangle \equiv \Phi_{\rm CCD}(\mathbf{m}) = \sum_{\gamma=2}^{M} \sum_{\mu<\nu}^{M} (-)^{\gamma+\mu+\nu} t^{p_\mu p_\nu}_{h_1 h_\gamma} \Phi^{M-2}_{\rm CCD}\left(\begin{smallmatrix} p_1 p_2 \cdots p_{\mu-1} p_{\mu+1} \cdots p_{\nu-1} p_{\nu+1} \cdots p_M \\ h_2 \cdots h_{\gamma-1} h_{\gamma+1} \cdots h_M \end{smallmatrix}\right) , \tag{2.21}$$

.

In the above equation we assumed that the single–particle indices are ordered, ie. $p_1 < \ldots < p_m$ and $h_1 < \ldots < h_m$. The wave function has a vanishing component for odd $M$, and the component for $M = 0$ is fixed by our choice of normalization to be 1 (ie. $\langle \Phi_{MF} | \Phi_{\rm CCD} \rangle = 1$). Tough we have concentrated just on the CCD case, it is clear that extensions to include singles (CCSD) and triples (CCSDT) corrections, useful for treating inhomogeneous systems or many–body interactions, are straightforward and we are actively working in this direction.

### Amplitudes from many–body perturbation theory

As we just saw CC wave–functions are an excellent choice as trial wave–functions, however, solving the CC equations (2.20) is computationally expensive. Therefore, we investigated the possibility of using less computationally demanding ways of obtaining the $t^{ab}_{ij}$, while still preserving the structure of the CC wave function. A simple option is to compute $t^{ab}_{ij}$ by the second order Møller-Plesset

perturbation theory (MP2):

$$t_{ij}^{ab} = \frac{\langle ij||ab\rangle}{\eta_i + \eta_j - \eta_a - \eta_b} \quad \text{with} \quad \eta_q = \epsilon_q + \sum_k \langle qk||qk\rangle \ . \tag{2.22}$$

If the CC equations are solved iteratively, then this is equivalent to stopping after the first iteration. In this way we are able to obtain decent wave–functions in a fraction of the time even when the iterative solution shows difficulties in convergence (eg. when static correlations are important).

This choice for the amplitudes is clearly a worse approximation than using the fully–converged CCD amplitudes, however since we are using these wave–functions as constrain for the random walk, as long as the nodal structure is sufficiently well-described the particular form of $\Phi_T$ should not matter since the Monte Carlo walk will develop the missing correlations. We have tested in few selected cases that this is indeed true and moreover, provided we include the $\gamma$–extrapolation step Eq.(2.14), the algorithm is so robust that we obtain reasonable values for the energy (within statistical error–bars) also by adding random noise to the amplitudes. For instance, in Fig.2.1 we show estimates of the CIMC correlation energies obtained at different values of the $\gamma$ parameter (and corresponding $\gamma = 0, 1$ extrapolation bands) for two different wave–functions: the black circles are obtained using amplitudes obtained from PT2 while for the red diamonds we used the distorted amplitudes

$$\tilde{t}_{ij}^{ab} = t_{ij}^{ab}(0.5 + \xi) \tag{2.23}$$

where $\xi$ is a random number uniformly distributed in $[0, 1]$. Even with this crude approximation the extrapolated values (employing just $\gamma = 0$ and $\gamma = 1$) agree with each other. This is a clear signature that the sign structure is really encoded in the overall structure (ie. the exponential ansatz) of the wave–function and not in the precise values of the amplitudes. This opens a lot of opportunities when we will go beyond CCD by employing analogous approximate expressions for the singles and triplets.

## 2.3 Basis set convergence and extrapolations

Working in a big but finite basis set requires some careful study on the convergence of the calculations that we carry out. A direct, and costly, check for the convergence of a finite–basis calculation is simply to increase the basis size until results no longer change within a predetermined threshold. This is the procedure we adopted for all the neutron matter calculations ([66, 67, 68]) in Section 3.1, where the presence of regulators in the interactions effectively suppresses the importance of contributions from high–energy states. In other situations, like the Homogeneous Electron Gas [65] in section 2.4, the convergence may be problematic due to the slow decay of the matrix elements of the Coulomb potentials as a function of the momentum–transfer in particle collisions (cf. Eq.(2.26)).

Methods for extrapolations to the infinite basis limit are then welcome since they can save a large amount of computer time, provided sensible estimates of the introduced systematic error can be obtained. In the HEG case for instance

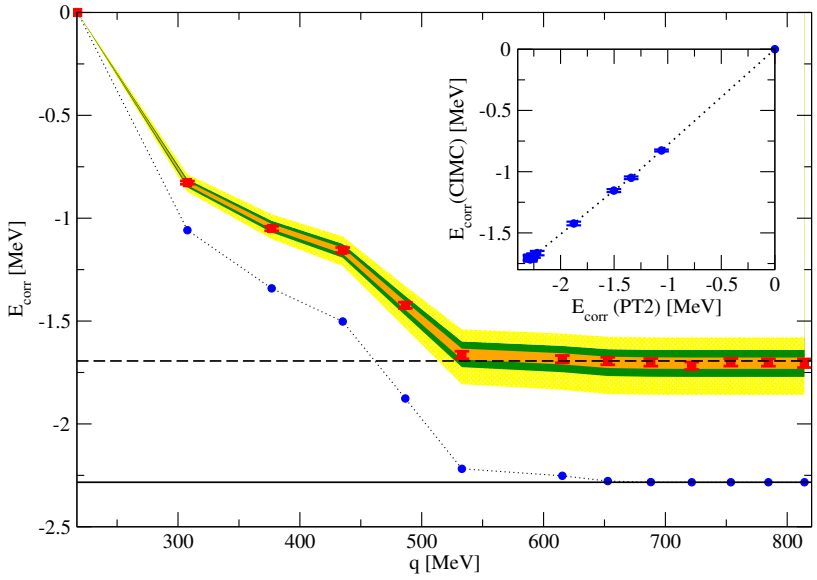


Figure 2.2: Plot of the correlation energy for N=14 neutrons obtained from PT2 (blue circles) and CIMC (red squares). The bands corresponds to extrapolations obtained fitting (2.25) up to $\Omega \equiv 435$ MeV (yellow band), $\Omega \equiv 486$ MeV (green band) and $\Omega \equiv 652$ MeV (orange band). The inset shows the CIMC correlation energy as a function of the PT2 correlation energy.

one can suppose that when the number of plane–waves $\Omega$ becomes large enough, the resulting energy $E(\Omega) \approx (1/\Omega)$ and one can extrapolate to the $\Omega \to \infty$ limit. Under this assumption of linearity one can even devise efficient schemes (see [69]) where a single calculation, performed at a value of $\Omega$ believed to be large enough, can be used to perform directly the calculations by estimating smaller–$\Omega$ results on–the fly.

Where exactly this linear regime starts is however a controversial question, in Section 2.4 we observe such trend just in the less interacting system considered. In this small section we want to report on a simple extrapolation method, based just on empirical evidence, that resulted to be quite robust against tests we did in many systems explored in our simulations.

The idea starts by noticing that the behavior of the correlation energy calculated with CIMC as a function of $\Omega$ is quite similar to the one produced by second order PT. As can be seen in Fig. 2.2 (where CIMC data are the red squares and PT2 results are the blue circles), we have approximately that

$$E_{corr}^{CIMC}(\Omega) \approx \gamma E_{corr}^{PT2}(\Omega), \tag{2.24}$$

with a $\Omega$–independent constant $\gamma$. If we now plot $E_{corr}^{CIMC}(\Omega)$ as a function of $E_{corr}^{PT2}(\Omega)$ we find indeed a smooth behavior (see inset in Fig.2.2). In some cases, like HEG with $r_s \leq 1$, a fit to the MC data with the simple ansatz Eq.(2.24) gives already a reduced $\chi^2 \approx 1$. In other more interacting circumstances, like the intermediate–density neutron matter of Fig.2.2 we have to introduce an

additional, arbitrary, parameter $\eta$:

$$E_{corr}^{CIMC}(\Omega) \approx \gamma E_{corr}^{PT2}(\Omega) + \eta E_{corr}^{PT2}(\Omega)^2 \tag{2.25}$$

to get a good fit with $\chi^2 \approx 1$. The three bands (orange, purple and green) in Fig.2.2 correspond to the results obtained using Eq.(2.25) when the two parameters $\gamma$ and $\eta$ are obtained trough fits to CIMC data up to the $\Omega$ corresponding to an UV cut-off of 435 MeV, 486 MeV and 652 MeV respectively. Values for higher momenta are predictions. In order to obtain the error bands we assumed $\gamma$ and $\eta$ to be perfectly correlated, thus the size of the bands may considered an upper–bound on the uncertainty (central values are much closer to the actual CIMC results).

It is striking to see that predictions made from the fit at values as low as 435 MeV, which is still far from the onset of the final plateau region, are capable of such accurate extrapolations with errors of $\approx 8\%$ in the correlation energy ($< 2\%$ in energy per particle).

## 2.4 Application: 3D Homogeneous Electron Gas

As a first application we investigated the three dimensional homogeneous electron gas (3DEG) using plane wave states, with definite momentum and spin as the sp basis set [65]. The 3DEG is described by a simple Hamiltonian; it nevertheless encapsulates many of the difficulties associated with modern many-body theories. In particular, it has both the weakly and strongly correlated regimes which can be accessed via a single tunable density parameter, the Wigner-Seitz radius $r_s$, thus providing an ideal system for benchmarking many body theories [29, 30, 69, 70, 71, 72].

The single–particle (sp) energies employed are $\varepsilon_i = \mathbf{k}_i^2/2m$, where $\mathbf{k}_i$ is the momentum of the $i$-state, and $m$ is the fermion mass. We include in our sp basis all single-particle states $i$ with $k_i^2 \leq k_{\max}^2$. The interaction matrix elements are given by:

$$\begin{aligned} V_{ij}^{ab} &= (1 - \delta_{\mathbf{k}_a - \mathbf{k}_i, 0}) \delta_{\mathbf{k}_i + \mathbf{k}_j, \mathbf{k}_a + \mathbf{k}_b} \frac{4\pi}{\Lambda} \frac{1}{(\mathbf{k}_a - \mathbf{k}_i)^2} \\ &= (1 - \delta_{\mathbf{k}_a - \mathbf{k}_i, 0}) \delta_{\mathbf{k}_i + \mathbf{k}_j, \mathbf{k}_a + \mathbf{k}_b} \frac{3}{N} \frac{1}{r_s^3} \frac{1}{(\mathbf{k}_a - \mathbf{k}_i)^2}, \end{aligned} \tag{2.26}$$

where the volume $\Lambda = L^3$ of the simulation box (and hence the unit spacing in momentum) is determined by the density (or $r_s$) and the number of particles $N$. We ignore the Madelung term because it does not affect the correlation energy.

In Table 2.1 we show the CCD energies, calculated using conventional CC theory, along with the corresponding Monte Carlo energies of an 3DEG system with $N = 14$ and $\mathcal{N}_s = 342$, for $r_s = 0.5, 1.0$ and 2.0. For these calculations we used $\gamma = 0$ in expressions (2.11), (2.12) and (2.13). We see that, for $r_s = 0.5$ the CCD energy is very close to the corresponding Monte Carlo energy. But, for $r_s = 1.0$ and 2.0 they are, in fact, lower than the corresponding Monte Carlo energies. Since, $E_{\text{CIMC}} \leq \langle \Phi_{\text{CCD}} | H | \Phi_{\text{CCD}} \rangle$ (see discussion above), this shows, once again, the non-variational nature of the energies obtained from conventional CC theory [73, 74].

| | Correlation energy (a.u.) | | | |
|---|---|---|---|---|
| $r_s$ | CCD | + CIMC | CCD(PT2) | + CIMC |
| 0.5 | −0.572682 | −0.5729(3) | −0.659641 | −0.5733(2) |
| 1.0 | −0.506701 | −0.5021(3) | −0.657347 | −0.5025(2) |
| 2.0 | −0.417946 | −0.40317(2) | −0.665071 | −0.4029(3) |

Table 2.1: Correlation energies for $N$ = 14 and $\mathcal{N}_s$ = 342 from conventional CC theory with the CCD and CCD(PT2) wave functions, along with the corresponding CIMC energies using each as importance functions. The numbers in parenthesis indicate statistical error in the last significant digit.

In Table 2.1 the energies obtained using the MP2 amplitudes are denoted by CCD(PT2). These CCD(PT2) amplitudes produce a worse approximation to the ground state wave function as compared to the full CCD amplitudes. Nevertheless, when used as importance functions in our CIMC algorithm, the final estimate for the ground state energy for both cases are very close. The statistical errors are comparable for $r_s$ = 0.5 and 1.0. For $r_s$ = 2.0 they are about an order of magnitude lower when the full CCD amplitudes are used.

The above observation is encouraging because it means that, as we mentioned in the previous section, it may not be necessary to solve the full CC equations to get reasonable $t_{ij}^{ab}$ amplitudes. Of course, we do not expect the CCD(PT2) amplitudes to be satisfactory for more strongly correlated systems. Still, even in those cases one can, presumably, use computationally inexpensive approximations to the full CC equations. For the rest of this work, all the CIMC results have been computed using the CCD(PT2) amplitudes.

In Fig. 2.3 we show the CIMC ground state energy estimates for $N$ = 14 and $r_s$ = 0.5, 1.0, 2.0 and 3.0 for some of our large basis size calculations. In Refs. [75, 72, 69] it was suggested that for the 3DEG it might be possible to extrapolate to the $\mathcal{N}_s \to \infty$ limit by exploiting a linear $1/\mathcal{N}_s$ dependence of the correlation energy for large but finite $\mathcal{N}_s$. Although, for $r_s$ = 0.5 and $N$ = 14 such a linear trend in the correlation energy is visible, for the other values of $r_s$ shown in the figure, no such trend is evident.

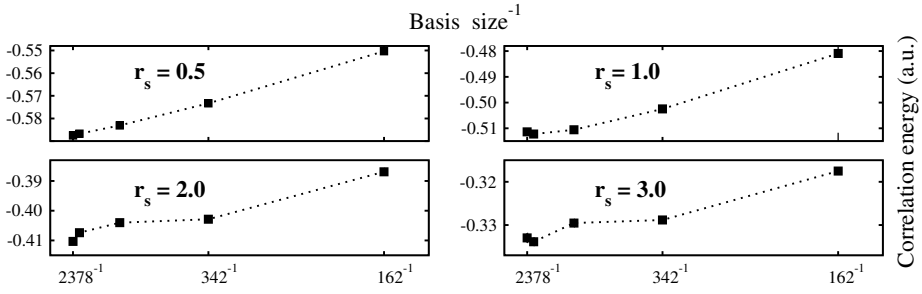


Figure 2.3: Correlation energies for $N$ = 14 and $r_s$ = 0.5, 1.0, 2.0 and 3.0 as a function of the single particle basis size from CIMC with the CCD(PT2) importance function. The statistical errors are smaller than the size of the symbols. The lines are drawn as a guide to the eye.

The situation is similar for calculations we performed with $N = 32$ and 54. Thus, at least up to our largest basis size $\mathcal{N}_s = 2378$, we cannot safely do an extrapolation to $\mathcal{N}_s \to \infty$ with a reasonably low $\chi^2$.

| | | Correlation energy (a.u) | |
|---|---|---|---|
| $r_s$ | N | CIMC | Other |
| 0.5 | 14 | −0.5875(6) | −0.5959(7) [69] |
| | 38 | −1.809(4) | −1.849(1) [69] |
| | 54 | −2.354(2) | −2.435(7) [69] |
| | | | −2.387(2) [71] |
| 1.0 | 14 | −0.5114(5) | −0.5316(4) [69] |
| | 38 | −1.521(4) | −1.590(1) [69] |
| | 54 | −2.053(4) | −2.124(3) [69] |
| | | | −2.125(2) [71] |
| 2.0 | 14 | −0.4103(6) | −0.444(1) [69] |
| | 38 | −1.134(7) | −1.225(2) [69] |
| 3.0 | 14 | −0.333(1) | |

Table 2.2: Correlation energies from CIMC with the CCD(PT2) importance function for different $r_s$ and $N$ and $\mathcal{N}_s = 2378$. For comparison we have also included the results from Ref. [71] (basis set independent) and Ref. [69] (extrapolated using single point extrapolation from $\mathcal{N}_s = 1850$ for $N = 14$ and from $\mathcal{N}_s = 922$ for $N = 38, 54$). The numbers in parenthesis indicate the statistical error in each case.

In Table 2.2 we show the ground state energy of different $r_s$ and $N$ for the largest $\mathcal{N}_s (= 2378)$ calculated by us. For comparison, we also include the energy estimates from Refs. [71] and [69]. The energies in Ref. [71] are calculated using the $r$-space diffusion Monte Carlo method with an importance function that included backflow correlation on top of the Slater-Jastrow wave function. These are strict energy upper bounds with a bias due to the fixed-node approximation. Nevertheless, they are believed to be highly accurate.

On the other hand, in Ref. [69] the energies are calculated in a finite CI like basis set (as in this work), using the Initiator Full Configuration Interaction Quantum Monte Carlo method ($i$-FCIQMC). The $\mathcal{N}_s \to \infty$ results are obtained by using the so called *single point extrapolation* from much smaller values of $\mathcal{N}_s$ than ours. These finite-basis set results are already in good agreement with the other calculations, capturing between 93% to 99% of the correlation energy. The energy upper bounds can be systematically improved by including higher order excitations (triples) in the CC wave function and by using larger basis sizes. Possibly, a much faster way to achieve basis set convergence is to use a finite basis renormalized Coulomb interaction [76].

Our method shares many similarities with the FCIQMC method. The FCIQMC method, in principle, can provide exact ground state energies for a CI Hamiltonian. However, most calculations are performed using the initiator approximation ($i$-FCIQMC) which adds a bias to the energy estimate. The energies in $i$-FCIQMC are not necessarily upper bounds to the true ground state energy. Due to the sign problem, the computational resources required in either

FCIQMC or $i$-FCIQMC scale as the size the many body Hilbert space, i.e., they are exponential in the system size, $N$, and the basis size, $\mathcal{N}_s$.

| | | | Computational time (cpu hours) | |
|---|---|---|---|---|
| $r_s$ | $N$ | $\mathcal{N}_s$ | CIMC | $i$-FCIQMC |
| 0.5 | 14 | 1850 | 384(0.6) | 200 |
| 1.0 | 14 | 1850 | 768(1.6) | 2500 |
| 2.0 | 14 | 1850 | 768(8.8) | 2500 |
| 2.0 | 38 | 922 | 4608(–) | 16000 |

Table 2.3: Computational cost of our method (CIMC) compared with the $i$-FCIQMC method [69] for different $r_s$, $N$ and $\mathcal{N}_s$. The numbers in parenthesis for CIMC are timings with a more efficient recent code.

Our method, instead, provides strict energy upper bounds, the tightness of which can be systematically improved by improving the quality of the importance function. Importantly, the computational cost of our Monte Carlo algorithm nominally grows as $N^2(\mathcal{N}_s - N)$, for both computational time (per Monte Carlo step) and memory requirements. Due to this polynomial scaling, we expect our method to be applicable to much larger systems than those manageable by conventional diagonalization methods or by ($i$-)FCIQMC. We see evidence of this in Table 2.3, where we compare computational time in our method with that in $i$-FCIQMC (especially using the more efficient recent version). The statistical error for the two methods are comparable in each case.

## 2.5 Pure observables

In this section we want to give the necessary details to compute *pure expectation–values* (PE) for operators that are diagonal in the basis that we are working on. In section 1.2.1 we have already seen that DMC–like techniques provide in general a *mixed expectation–value* (ME) (cf Eq.(1.27)) which, for observables that does not commute with the Hamiltonian $\hat{H}$, is in general different from the PE:

$$\langle O \rangle_{ME} = \frac{\langle \Psi_I | \hat{O} | \Psi_0 \rangle}{\langle \Psi_I | \Psi_0 \rangle} \neq \frac{\langle \Psi_0 | \hat{O} | \Psi_0 \rangle}{\langle \Psi_0 | \Psi_0 \rangle} = \langle O \rangle_{PE} \tag{2.27}$$

This is for instance the case if we want to calculate the occupation number operator, $n(\vec{k})$ in momentum–space or $g(\vec{r})$ in coordinate–space. However, even in these cases, we can construct an estimator for the PE of the observable with the help of Hellmann–Feyman theorem.

Let us define an auxiliary hamiltonian $\hat{H}_O \equiv \hat{H} + \alpha \hat{O}$ and the following energy:

$$E_\tau(\alpha) = \frac{\langle \Psi_\tau | \hat{H}_O | \Psi_\tau \rangle}{\langle \Psi_\tau | \Psi_\tau \rangle} = \frac{\langle \Psi_I | \hat{H}_O | \Psi_\tau \rangle}{\langle \Psi_I | \Psi_\tau \rangle} \tag{2.28}$$

where $|\Psi_\tau\rangle$ is the projected wave–function at imaginary–time $\tau$ obtained using the propagator corresponding to $\hat{H}_O$:

$$e^{-\tau \hat{H}_O} = e^{-\tau \hat{H}} e^{-\tau \alpha \hat{O}} + O(\alpha) \tag{2.29}$$

.

Then the Hellmann–Feynmann theorem provides the following expression for the PE of $\hat{O}$:

$$\langle O \rangle_{PE} = \lim_{\alpha \to 0} \frac{\partial E(\alpha)}{\partial \alpha} \tag{2.30}$$

where the derivative involved in the above equation can, in principle, be calculated numerically. Numerical derivatives are however noisy, especially for small values of $\alpha$ and we avoid this problem by using a recent algorithm developed in reference [77].

Let us first note that if $\hat{O}$ is diagonal in the basis where we are working, the additional piece in the propagator

$$e^{-\tau \alpha \hat{O}}$$

can be incorporated in the *branching* part of the original propagator (cf. Eq.(2.5) and Appendix D), and thus simply amounts to a change in the weights of the configurations during the simulation. For instance the weight for a walker moving on the state $\mathbf{n}$ in a time–step $\Delta\tau$ will now be given by:

$$b(\mathbf{n}) \longrightarrow b_\alpha(\mathbf{n}) \equiv b_{(\alpha=0)}(\mathbf{n}) e^{-\Delta\tau\alpha O_L(\mathbf{n})}. \tag{2.31}$$

The total energy at imaginary–time $\tau$ will be given by the (weighted) average among the $N_W$ walker present in the simulation[1]:

$$E_\tau(\alpha) = \frac{\sum_j^{N_W} b_\alpha(\mathbf{n}_{\tau;j}) E_L(\alpha; \mathbf{n}_{\tau;j})}{\sum_j^{N_W} b_\alpha(\mathbf{n}_{\tau;j})} \tag{2.32}$$

where $\mathbf{n}_{\tau;j}$ is the Slater–Determinant occupied by the $j$th–walker at imaginary–time $\tau$, while $E_L(\alpha; \mathbf{n}_{\tau;j})$ is the local–energy Eq.(1.17) calculated at $\mathbf{n}_{\tau;j}$. Walkers will accumulate corrections to the weight along the random walk so that the weight factor $b_\alpha$ at time $\tau$ will be given by:

$$b_\alpha(\mathbf{n}_\tau) = b_{(\alpha=0)}(\mathbf{n}_\tau) e^{-\Delta\tau\alpha \sum_{\tau'}^{\tau} O_L(\mathbf{n}_{\tau'})} \tag{2.33}$$

where the sum in $\tau'$ goes in discrete steps $\Delta\tau$. The equation for the energy becomes then:

$$\begin{aligned} E_\tau(\alpha) &= \frac{\sum_j^{N_W} b_{(\alpha=0)}(\mathbf{n}_{\tau;j}) e^{-\Delta\tau\alpha \sum_{\tau'}^{\tau} O_L(\mathbf{n}_{\tau';j})} E_L(\alpha; \mathbf{n}_{\tau;j})}{\sum_j^{N_W} b_{(\alpha=0)}(\mathbf{n}_{\tau;j}) e^{-\Delta\tau\alpha \sum_{\tau'}^{\tau} O_L(\mathbf{n}_{\tau';j})}} \\ &= \frac{\sum_j^{N_W} b_{(\alpha=0)}(\mathbf{n}_{\tau;j}) e^{-\Delta\tau\alpha \sum_{\tau'}^{\tau} O_L(\mathbf{n}_{\tau';j})} \left[ E_L(\mathbf{n}_{\tau;j}) + \alpha O_L(\mathbf{n}_{\tau;j}) \right]}{\sum_j^{N_W} b_{(\alpha=0)}(\mathbf{n}_{\tau;j}) e^{-\Delta\tau\alpha \sum_{\tau'}^{\tau} O_L(\mathbf{n}_{\tau';j})}} \\ &= \frac{\sum_j^{N_W} b_{(\alpha=0)}(\mathbf{n}_{\tau;j}) e^{-\tau\alpha X_j(\tau)} \left[ E_L(\mathbf{n}_{\tau;j}) + \alpha O_L(\mathbf{n}_{\tau;j}) \right]}{\sum_j^{N_W} b_{(\alpha=0)}(\mathbf{n}_{\tau;j}) e^{-\tau\alpha X_j(\tau)}} \end{aligned} \tag{2.34}$$

where in the last expression we have defined the running average for walker $j$:

$$X_j(\tau) = \frac{1}{k} \sum_l^k O_L(\mathbf{n}_{\tau = l\Delta\tau;j}) \quad \text{with} \quad \tau \equiv k\Delta\tau. \tag{2.35}$$

[1] we will neglect effects coming from branching/population–control that will introduce a time dependence in $N_W \to N_W(\tau)$

Now taking the derivative with respect to $\alpha$ and taking the limit $\alpha \to 0$ in Eq.(2.34), we get

$$\begin{aligned} \langle O \rangle_{PE} &= \langle O \rangle_{ME} - \tau \; cov\left(E_L(\tau), X_L(\tau)\right) \\ &= \langle O \rangle_{ME} - \tau \left[ \langle E_L(\tau) X_L(\tau) \rangle_{ME} - \langle E_L(\tau) \rangle_{ME} \langle X_L(\tau) \rangle_{ME} \right]. \end{aligned} \tag{2.36}$$

Since the correlation time is finite, the second term on the right hand side of the above equation does not depend on $\tau$ for large enough $\tau$. Thus, the pure estimator for $\hat{O}$ is independent of $\tau$ as it should. All terms on the right hand side of Eq.(2.36) are quantities that can be calculated during *a single CIMC simulation* with the hamiltonian $\hat{H}_O$. We also note that the correction term in Eq.(2.36) vanishes in the limit $\Psi_I = \Psi_G \to \Psi_0$, again as it should.

The implementation of the algorithm is straightforward as it just amounts to attaching to each walker the auxiliary variable $X$ and updating it trough the random walk. A small number of equilibration steps were taken before averaging.

We note in passing that the same ideas can be applied to the calculation of general susceptibilities (see [78]), but we didn't try to calculate them in this work.

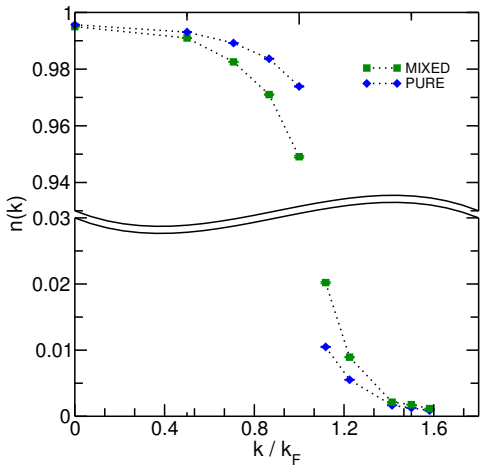


Figure 2.4: Comparison between the pure and mixed estimates of the momentum distribution for the Yukawa potential with $r_s = 1.36$ and $\xi = 1.74$.

## 2.6 Application: Yukawa and momentum distributions

As application of the techniques exposed in the last section we want to calculate the momentum–distribution of Yukawa fermions, interacting trough a screened

pair potential given by

$$V(r) = \frac{e^{-\mu r}}{r} = \frac{e^{-r/\xi}}{r}. \tag{2.37}$$

The matrix elements $V_{ij}^{ab}$ in momentum–space can be rewritten in terms of two parameters $r_s$ and $\xi$:

$$V_{ij}^{ab} = \delta_{\mathbf{k}_i+\mathbf{k}_j,\mathbf{k}_a+\mathbf{k}_b} \frac{3}{N} \frac{1}{r_s^3} \frac{1}{(\mathbf{k}_a - \mathbf{k}_i)^2 + \frac{1}{\xi^2}} \tag{2.38}$$

where $r_s$ is the Wigner–Seitz radius and $\xi = 1/\mu$ is a range parameter. By sending the range $\xi \to \infty$ we recover the usual Coulomb interaction. Our Monte

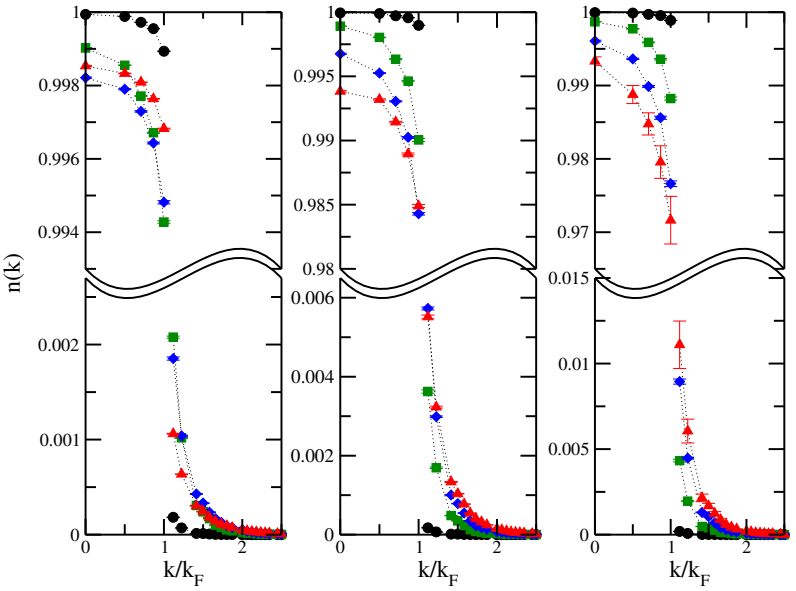


Figure 2.5: Momentum distribution for the Yukawa potential with $\xi = 0.5$ (left), $\xi = 1.0$ (center) and $\xi = 2.0$ for different values $r_s$. The black dots are $r_s = 0.1$, green squares are $r_s = 0.5$, blue diamonds are $r_s = 1.0$ while the red triangles correspond to $r_s = 2.0$.

Carlo calculations were performed with different numbers of particles, up to $N = 66$, and for each value of $N$ we used increasing values of $k_{\max}$. Apart from the boundary regions close to $k \sim k_{\max}$, the momentum distribution seemed to converge by $k_{\max}^2 = 20$. All the results reported here, use $N = 66$, $k_{\max}^2 = 20$ and the approximation of the CC doubles wave function CCD(PT2). In Fig. 2.4 we compare the pure and the mixed estimates for the momentum distribution for the repulsive Yukawa potential with $r_s = 1.36$ and $\xi = 1.74$ (the Bethe "homework" potential coming from the repulsive $^1S_0$ core of the Reid potential).

As can be seen, the mixed estimator overestimates considerably the depletion at the Fermi–surface, thus having for instance important consequences on the calculated quasi–particle properties. We also performed calculations for many different values of $r_s$ and $\xi$ and present some of the momentum distributions in Fig. 2.5.

For the barely interacting case $r_s = 0.1$ the density is so high in this case that no difference is noticeable by changing $\xi$. In the other cases however the effects of the range parameter are much more evident. The rightmost panel in Fig. 2.5 resembles a Coulomb system where by decreasing the density (increasing $r_s$) we will increase the interaction strength resulting in a more pronouced hole for zero–momentum states and a smaller quasi–particle residue at the Fermi surface. When the screening length is reduced to $\xi = 1.0$ the strongest effect is at the Fermi–surface where the discontinuity at $k = k_F$ is smaller for $r_s = 2.0$ than it is for the higher density system $r_s = 1.0$. Finally in the leftmost panel, the range considered $\xi = 0.5$ is so small that the system with $r_s = 2.0$ becomes less interacting than the $r_s = 1.0$ one and the biggest depletion at $k_F$ is obtained for the relatively dense $r_s = 0.5$ case.

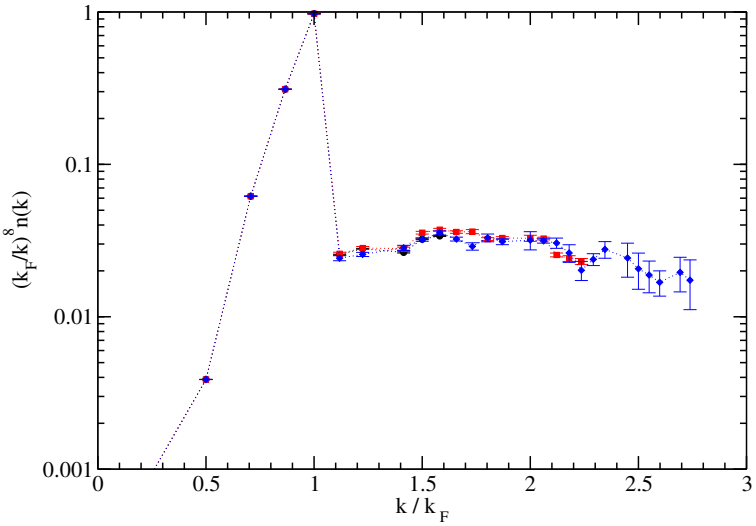


Figure 2.6: High momentum tail of $n(k)$ for a system of 66 particles with $\xi = 2.0$, $r_s = 1.0$ and different values of the UV cut–off: black circles $k^2_{\rm max} = 10$, red squares $k^2_{\rm max} = 20$, blue diamonds $k^2_{\rm max} = 30$.

Another interesting quantity that can be calculated from the momentum distribution is its high–momentum tail, which is directly connected to the probability of finding two particle in the same position. For the Yukawa potential the asymptotic behavior of $n(k)$ is given by

$$n(k) \xrightarrow{k\to\infty} \lambda r_s^2 g(0) \left(\frac{k_F}{k}\right)^8 \tag{2.39}$$

where $\lambda$ is some constant and $g(0)$ is the pair distribution function at $r = 0$. In Fig. 2.6 we show the emergence of the polynomial high–momentum tail, we however didn't attempt to extract the value for $g(0)$ from the data since we found sizable finite–size effects for some combinations of $r_s$ and $\xi$ that need further explorations.

# Chapter 3

# QMC with non–local chiral interactions

An interesting side–effect of the formulation in Fock–space of Diffusion Monte Carlo is the ability to treat in a reliable way hamiltonians containing interactions that are not–diagonal in the chosen basis. An example are *non–local* potentials in coordinate space

$$\langle \vec{r}|\hat{V}|\vec{r}'\rangle = V(\vec{r},\vec{r}') \neq \delta(\vec{r}-\vec{r}')\,V(\vec{r}), \tag{3.1}$$

that are notoriously difficult to deal with in conventional coordinate–space methods. Usually they are treated by localizing the interaction using some trial state [79], thus introducing an additional bias to the calculation (see however [80] for some recent attempts). This kind of interaction are less uncommon than one may think, they appear for instance in electronic structure calculations involving pseudopotentials [81] as well as in low–energy nuclear theory where non–local potentials naturally emerge from Effective Field Theory calculations carried in momentum–space [82]. In particular Chiral effective field theory ($\chi$-EFT) has seen an increasing attention in recent years as a bridge between QCD and low energy nuclear physics by providing a systematic expansion for the nuclear forces based on the symmetries and on the symmetry breakings of QCD [25, 26, 27]. Chiral interactions have already been employed in calculations of nuclear structure and reactions of light and medium-mass nuclei [83, 84, 85, 86, 87, 88, 89, 90, 91, 92, 93, 94, 95, 96, 97, 98], and infinite matter [99, 100, 101, 102, 103, 104]. However, non–perturbative Quantum Monte Carlo calculations with these potentials have become possible just recently thanks to the development of a local–version [28, 105] valid up to the third (NNLO) order in the chiral expansion. With the help of Configuration Interaction Monte Carlo we are now able to treat on an equal footing both local and non–local interactions thus allowing for a more consistent comparison with other many–body techniques.

Accurate predictions of the dynamics of a supernova explosion and of the structural properties of compact stars is tightly related to the correct understanding of the properties of dense matter, and in particular of its equation of state (EoS). In this chapter we will explore the predictions made with $\chi$-EFT

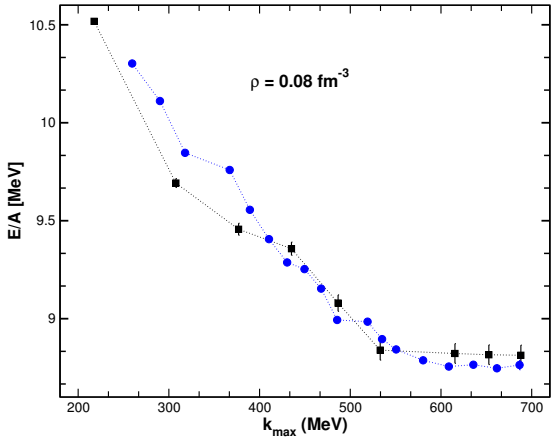


Figure 3.1: The convergence of our energies as a function of $k_{\max}$ at $\rho = 0.08$ fm$^{-3}$ for 14 (black squares) and 66 (blue circles) particles interacting trough NNLO$_{\rm opt}$ interaction. The dotted lines are a guide to the eye.

interaction for the equation of state of both Pure Neutron Matter considering systems of $N = 66$ neutrons interacting through either the N2LO interaction by Ekström et al. [106] or the N3LO interaction by Entem and Machleidt [26, 107]. We then review our recent work on spin–isospin impurities in polarized neutron matter with the aim of constraining the parameters of Skyrme–type Energy Density Functionals [108]. Finally we present some unpublished results for a small ($A = 28$ nucleons) system of Symmetric Nuclear Matter ($N = Z$) comparing against recent Coupled–Cluster and Auxiliary–Field Diffusion Monte Carlo (AFDMC) results.

## 3.1 Pure Neutron Matter

A widely accepted model for the outer core of a neutrons star is an homogeneous system of nucleons at relatively high densities (up to several times nuclear saturation density) and with relatively low ($\approx 5 - 10\%$) fraction of protons. A first, further simplified, description of this system can be obtained by considering a bulk system of neutrons–only: the so called *Pure Neutron Matter*. A good understanding of the properties of PNM is important in order to constrain effective theories that are later applied to more exotic and realistic phases of dense matter.

In this section we calculate the equation of state (EoS) and the nucleon chemical potentials in pure neutron matter up to one and a half times the nuclear saturation density. In addition, we also present unbiased QMC estimates of the momentum distribution. Since we are using 2–body interactions only, we stress that results obtained at intermediate to high densities should be taken with caution due to the neglected effect of many–body forces.

Focusing on homogeneous systems we can use again the plane wave states, with definite momentum, spin and now isospin as the sp basis set. Again, we

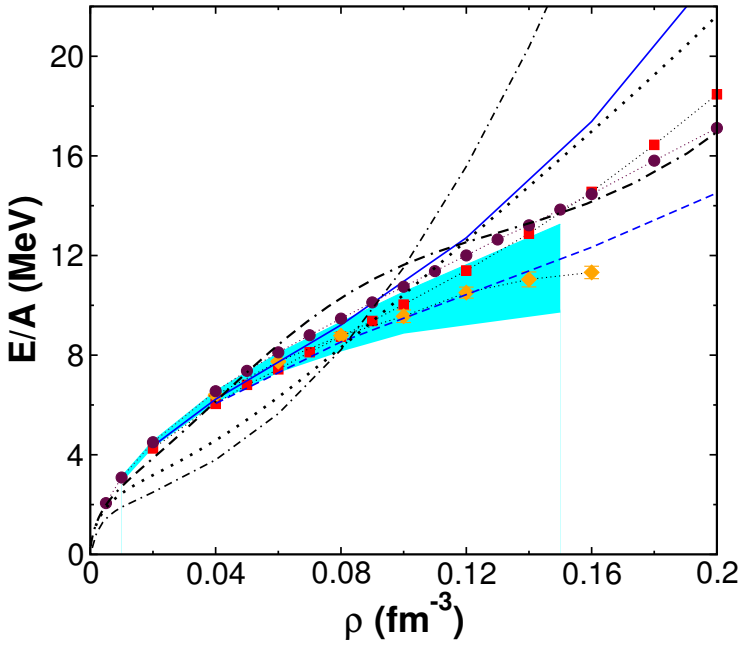


Figure 3.2: The EoS of pure neutron matter: red squares - CIMC results (66 neutrons), $\mathrm{NNLO_{opt}}$ (brown circles) and N3LO 500* (orange diamonds) interaction respectively - AFDMC EoS with the 2b AV8' [109], blue dashed line - APR EoS with the 2b AV18 [110], blue solid line - APR EoS with the 2b AV18 + 3b UIX [110], cyan band - AFDMC band with local NNLO interaction [28], black dashed dotted line - NL3 EoS [111], dotted and dash–dash dotted lines - SFHo and SFHx Eos respectively [112].

always include in our sp basis all single-particle states $i$ with $k_i^2 \leq k_{\mathrm{max}}^2$. As seen in the previous chapter, cutoff independent results can be obtained by performing successive calculations with increasing $k_{\mathrm{max}}$ and then extrapolating to $k_{\mathrm{max}} \to \infty$.

As mentioned earlier, in CIMC, successive calculations with larger sp basis sizes need to be performed till convergence. In Fig. 3.1 we plot the energy per particle as a function of $k_{\mathrm{max}}$ at $\rho$ = 0.08 fm$^{-3}$ for 14 and 66 particles. We deem the CIMC calculations for have converged when the difference in the energy estimate between successive values of $k_{\mathrm{max}}$ is less than the statistical error (typically $\sim 10 - 25$ KeV at convergence). For all the densities considered in this work we observe a smooth convergence in the CIMC calculations as a function of $k_{\mathrm{max}}$.

In Fig. 3.2, we show our results for the EoS (energy per particle vs density) of pure neutron matter employing both the $\mathrm{NNLO_{opt}}$ and N3LO 500* interactions. The latter is a regular Entem–Machleidt N3LO potential but with the regulators of the N3LO contacts chosen independently of the partial–wave (cf. [26] for details), this just for efficiency reasons (we work in the operator basis). The corresponding LECs have been refitted obtaining a slightly different set that we used in our calculations.

The energies refer to a box containing 66 neutrons with periodic boundary conditions. For periodic boundary conditions, finite size (shell) effects are minimal for the shell closures at 14 and 66 (see, e.g. Ref. [113]). For comparison, we have also included the variational APR EoSs (two body - AV18 and two plus three body - AV18+UIX interactions) [110], the AFDMC EoS (two body - AV8′ interaction) [109], the AFDMC EoS band from *local* NNLO chiral interactions [28]. Moreover, since most computer simulations of supernovae use phenomenological EoSs based typically on the liquid drop model, the most popular being the Lattimer-Swesty EoS [114], or on relativistic mean field theory [115, 116, 112, 117, 118], we have included also three Relativistic Mean Field (RMF) calculations usually employed in this context: the NL3 EoS [111] and the recent SFHo and SFHx [112] which were constrained on neutron–star observational data.

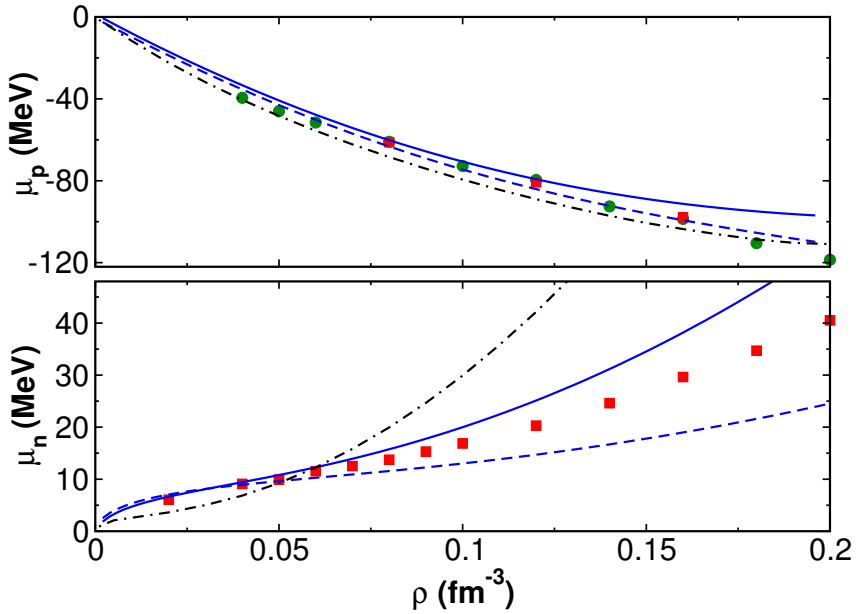


Figure 3.3: The proton and neutron chemical potentials in pure neutron matter: green circles - our results for 14 neutrons. The rest of the legend is similar to Fig. 3.2.

The nucleon chemical potentials in dense matter play a crucial role in determining the proton fraction at beta equilibrium, and consequently the equation of state and the cooling mechanism in neutron stars. In Fig. 3.3, we show the proton and the neutron chemical potentials in pure neutron matter. We calculate the neutron chemical potential

$$\mu_n = \rho \partial(E/N)/\partial\rho + E/N$$

by numerical differentiation of the EoS. The proton chemical potential ($\mu_p$) is calculated from the binding energy of one extra proton in pure neutron matter. The calculations for $\mu_p$ were performed for 14 neutrons + 1 proton; however,

we also checked in a few cases that the results for the 66 neutrons + 1 proton case are within 2%.

For $\mu_p$ all the calculations are reasonably consistent with each other. For the EoS and $\mu_n$, however, only the calculations based on microscopic Hamiltonians fit to the scattering phase shifts are consistent (within $\sim 10\%$) at low densities ($\rho \lesssim 0.1$ fm$^{-3}$). Other many body calculations based on microscopic Hamiltonians [28, 99, 100, 101, 103, 104] are also consistent with the ones shown in the figure in this density range.

The RMF models on the other hand have a completely different behavior for low density neutron matter (with the exception of SFHx). Such a failure of most of the currently popular phenomenological EoSs to meet the constraints set by microscopic calculations was also pointed out recently, in the context of chiral EFT interactions, in Ref [104].

*Momentum Distribution.*— In interacting fermionic systems the momentum distribution, $n(k)$, is modified from the ideal Fermi-Dirac distribution due to quantum correlations. In particular, the quasiparticle renormalization factor $Z = n(k_F^-) - n(k_F^+)$ plays a fundamental role in Fermi liquid theory in quantifying the impact of the in-medium effective interactions [119]. In homogeneous systems, the Fourier transform of $n(k)$ is the reduced off diagonal single particle density matrix, which is the primary object in density-matrix functional theory [120]. As we mentioned in Section 2.5, computing an estimate of the

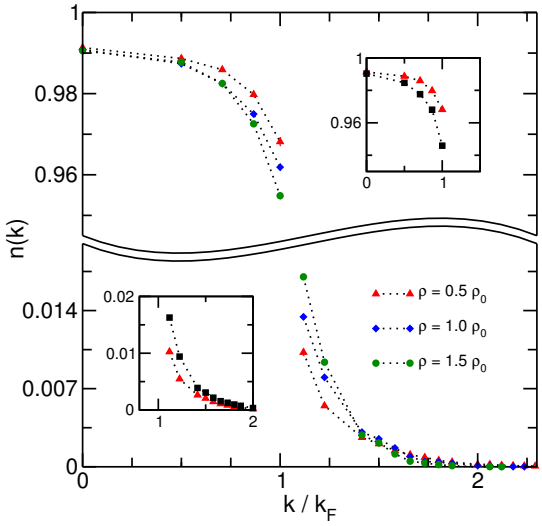


Figure 3.4: Pure estimates momentum distribution of pure neutron matter from our QMC method for three different densities. The inset shows the comparison between the pure and the mixed estimates for $\rho = 0.5\rho_0$. The dotted lines are a guide to the eye.

momentum distribution within continuum QMC methods that is independent of the importance function (a.k.a. pure estimator) is notoriously difficult, due to the fact that $n(k)$ is an off-diagonal operator in real space. In CIMC, on the the other hand, $n(k)$ is a diagonal operator. We adopt the method exposed in

Section 2.5 to our CIMC method to calculate the momentum distribution. In Fig. 3.4 we show $n(k)$ in pure neutron matter for three different densities.

Our estimates for the occupation number at zero momentum $n(0)$ and the renormalization factor $Z$ are given in Table 3.1. These results can be compared,

| $\rho(\mathrm{fm}^{-3})$ | $Z$ | $n(0)$ |
|---|---|---|
| 0.08 | 0.9579(8) | 0.9913(5) |
| 0.16 | 0.9484(8) | 0.9909(5) |
| 0.24 | 0.9378(8) | 0.9906(5) |

Table 3.1: The renormalization factor $Z$ and the occupation number at zero momentum $n(0)$ in neutron matter

e.g., with those in Ref. [121] for CDBONN and the Argonne family of potentials with the self-consistent Green's function method. The rather large values of $n(0)$ in Table. 3.1 is due to the softness of the $\mathrm{NNLO_{opt}}$ interaction.

In the inset we compare the pure and mixed estimates of the momentum distribution at density $\rho = 0.08$ fm$^{-3}$. We see that the biased mixed estimator for $n(k)$ overestimates both the depletion at $k \to k_F^-$ and the growth at $k \to k_F^+$ by more than 50%, a behavior very similar to what we found for the Yukawa interaction in the previous chapter.

## Uncertainties of the calculations

In order to make reliable *ab initio* predictions, it is very important to have an estimate of the theoretical uncertainty coming from all possible sources. Given the number of particles, the uncertainties in our calculations come from two sources: (a) the inherent uncertainty in the chiral EFT Hamiltonian due to the neglect of higher orders and to the ultraviolet cutoff dependence, and (b) the uncertainty in the many body method. In this work we do not address the former, while noting that a significant amount of effort has already been devoted to this question by other authors. The latter, in our QMC calculations (assuming convergence in $k_{\max}$), has two sources: the statistical error and the bias introduced due to the fixed-phase approximation. We see in Fig. 3.5 that the statistical error is $1-2\%$ of the correlation energy (measured with respect to the Hartree-Fock energy). Note that this uncertainty can be systematically reduced by simply running the simulations for longer time. For comparison, we also show the (absolute) difference between our QMC energy, and the energies obtained from CC theory (with the CCD wave function) [103] and from 2nd order perturbation theory (PT-2), all as fractions of the QMC correlation energy. For this particular interaction and the densities considered, the CCD energy estimate is, in fact, quite close to the QMC estimate, differing at most by about 3% at $\rho = 0.04$ fm$^{-3}$; while in PT-2, the correlation energies are overestimated by $24-36\%$ compared to our QMC results.

The uncertainty due to the fixed-phase approximation is very difficult to assess in continuum QMC calculations because, in general, a systematic scheme to improve the guiding wave function is not available. Fortunately, in our CIMC method the energies are rigorous upper bounds, and CC theory provides a sys-

tematic scheme for constructing more general guiding wave functions. We exploit this hierarchy to provide a perturbative estimate of the leading order contribution to the bias due to the fixed-phase approximation, viz. that due to the exclusion of the irreducible triples in the guiding wave function.

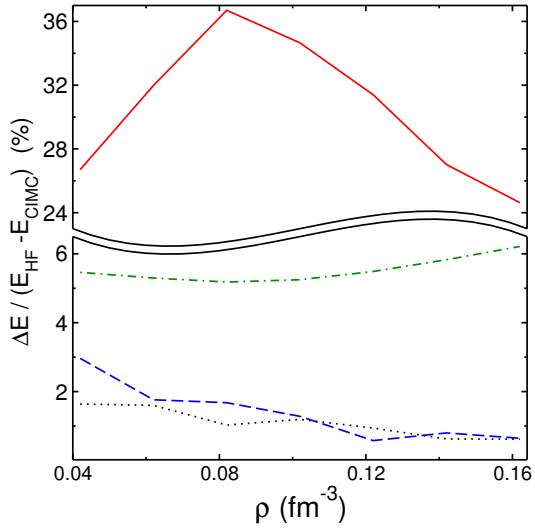


Figure 3.5: Different energy scales as a fraction of the QMC correlation energy: red solid line - $\Delta E$ = difference between PT-2 and QMC energies, blue dashed line - $\Delta E$ = difference between the CCD [103] and QMC energies, black dotted line - $\Delta E$ = statistical error in the QMC energies, green dashed dotted line - $\Delta E$ = estimate of the fixed-phase bias in the QMC energies (see text).

The difference between the CCD(T) , i.e., CCD with perturbative triples, and the CCD energies [103] provide such an estimate. However, just as the correlation energy is overestimated in PT2, we expect CCD(T), which is a similar perturbative estimate, to overestimate the residual correlation energy. Therefore, we obtain our improved estimate by multiplying this quantity by the ratio of our QMC correlation energy and the PT2 correlation energy. Note that, the correction in energy from CCD(T) is always negative, which is consistent if one considers this to be the estimated correction on our QMC energy estimate, which is a *variational upper bound*. This is not the case for the energies obtained from standard CC theory.

We plot the above estimate, again as a fraction of the QMC correlation energy in Fig. 3.5. This estimate of about $5-6\%$ of the correlation energy ($\sim 1\%$ of the total energy), probably still overestimates the theoretical uncertainty, since in the homogeneous electron gas, the CIMC method (with a CCD type guiding wave function) was found to be accurate to within $2-3\%$ in the moderately interacting regime [65]. In any case, the overall uncertainty in our many body method is certainly much less than the inherent uncertainty in the Hamiltonian, and in future work we plan to reduce it further by including the irreducible triples in our guiding wave function.

## 3.2 Polarized Pure Neutron Matter

In this section we report the results from CIMC calculations with a chiral EFT Hamiltonian for fully polarized (spin up) low density neutron matter with an impurity (spin down neutron or spin up/down proton). The impurity problem that we discuss here is a generalization of the well known polaron problem in solid state systems and in ultracold gases (see, e.g. in [122, 123]). In fact, we find that the proton spin-down impurity behaves in a manner which is qualitatively very similar to a polaron in a fully polarized Fermi gas in the unitary regime, i.e., the regime with diverging s-wave scattering length ($a_s \to \infty$) and vanishing effective range ($r_e \to 0$), over a wide density range $10^{-3}$ fm$^{-3} \le \rho \le 5\times10^{-2}$ fm$^{-3}$.

As we have briefly mentioned in the introduction to this chapter, the main motivation behind this explorations is to put stringent constraint on nuclear Energy Density Functionals. The main problem being the fact that most nuclear EDFs are fit to the ground state properties of even-even nuclei, saturation properties of nuclear matter and, occasionally, to microscopic calculations of unpolarized neutron matter. These quantities constrain only that part of the EDF which depends on the time-reversal-even densities ("time-even part"). The EDF also depends on time-reversal-odd densities ("time-odd part") which plays an important role in a variety of phenomena: binding energies of odd-mass nuclei [124], pairing correlations in nuclei [125], distribution of the Gamow-Teller strength [126], properties of rotating nuclei [128, 129], nuclear magnetism [130]

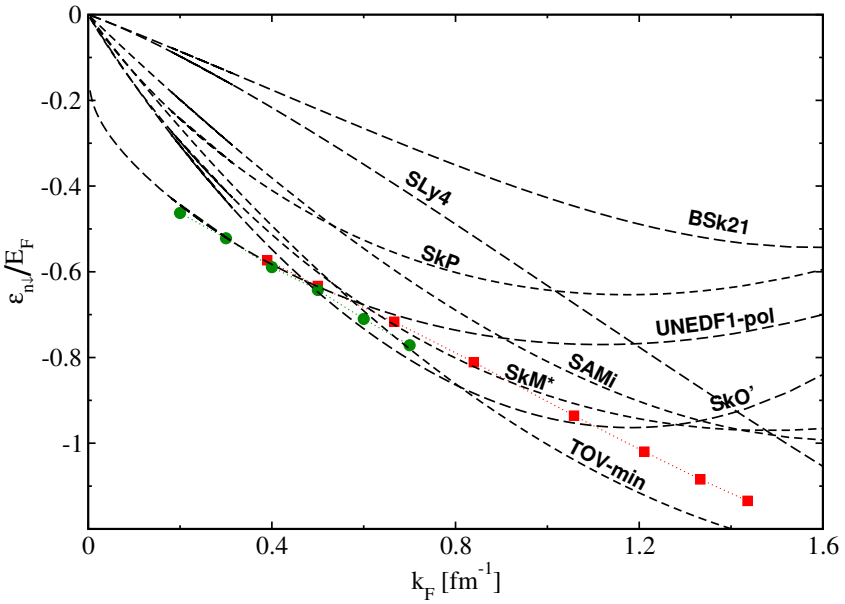


Figure 3.6: The energy of the neutron spin-down impurity in the units of the Fermi energy of the spin-up neutrons. The red filled squares are our QMC results with the NNLO$_{\rm opt}$ interaction. The green filled circles are the GFMC calculations with an s-wave interaction fit to the $nn$ scattering length and effective range [127]. The black dashed lines are predictions from various density functionals (see text).

etc. At present, the time-odd part of the nuclear EDF is ill-determined because of the lack of unambiguous constraints.

We will show that the difference between energies of the proton spin up and spin down impurities depends only on the time-odd part of the EDF. Thus, our results provide stringent constraints for the time-odd part of the density functional, *independent of the time-even contributions*.

The calculation proceeds by computing the ground state energies for a fully polarized system and that with an additional impurity particle. The difference between these two energies gives the impurity energy. We use the next-to-next-to-leading order chiral $\mathrm{NNLO_{opt}}$ two body interaction [106] for our calculations.

We have focused on two–body potentials in this study due to the emerging consensus that the theoretical uncertainties of the nuclear forces is largely suppressed in low density neutron matter (densities sufficiently less than the saturation density of nuclear matter). In this regime, the properties of the relevant components of the two nucleon forces are well established and the contributions from three and higher body forces are rather small. Any realistic nucleon-nucleon interaction, which fits the low energy nucleon-nucleon scattering phase shifts and the binding energy of deuteron, in conjunction with an accurate many body method produce consistent "theoretical data"; which can provide constraints for the EDF complementary to those coming from experiments.

In Fig. 3.6 we plot the ratio of the energy of neutron spin-down impurity, $\varepsilon_{n\downarrow}$, and the Fermi energy of the fully polarized system, $E_F$, versus the Fermi momentum $k_F$. Our results are good agreement with the GFMC calculations reported in Ref. [127] using an s-wave interaction (fit to the $nn$ scattering length and effective range). For example, at $k_F = 0.4$ fm$^{-1}$, we get $\varepsilon_{n\uparrow}/E_F = -0.582 \pm 0.002$ while the GFMC calculation gives $-0.589 \pm 0.005$. An AFDMC calculation performed the Argonne $v_8'$ potential gives $-0.567 \pm 0.006$ at the same $k_F$.

The impurity energies reported in Fig. 3.6 and later in Fig. 3.7 were performed with $N = 7$ spin-up neutrons. We have checked in selected cases that the difference between the $N = 7$ and the $N = 33$ energies is less than about $1 - 2\%$. For example, for $\rho = 0.04$ fm$^{-3}$ $\varepsilon_{n\downarrow}/E_F$ is $-0.6698 \pm 0.0005$ with $N = 7$ and is $-0.664 \pm 0.006$ for $N = 33$, while for $\rho = 0.06$ fm$^{-3}$ the corresponding values are $-0.6617 \pm 0.0003$ and $-0.647 \pm 0.004$. With $N = 7$ the size of the box, $L$, for the largest density we consider in this work ($\rho = 0.06$ fm$^{-3}$) is about 4.9 fm. This is about three times the characteristic range of the nucleon-nucleon interaction given by the pion Compton wavelength ($\approx 1.4$ fm). At higher densities ($\rho \geq 0.06$ fm$^{-3}$) the corrections resulting from performing calculations with a finite number of particles is expected to sizeable and it is customary to perform calculations with larger particle number ($N \geq 33$, for each spin). However, at the densities we are considering in this paper, the finite particle number corrections (even at $N = 7$) can be reasonably expected to be smaller than, or at most comparable to, the other sources of uncertainty (the non inclusion of three body forces in the Hamiltonian or the absence of triples in the wave function).

In Fig. 3.7 we plot the ratio of the energy of the proton spin up/down impurity ($\varepsilon_{p\uparrow/\downarrow}$) and $E_F$. The density dependence of $\varepsilon_{p\uparrow/\downarrow}/E_F$ is rather weak. In fact, the QMC results for $\varepsilon_{p\downarrow}/E_F$ change by less than 2% ($-0.681 < \varepsilon_{p\downarrow}/E_F < -0.666$) when the density changes by more than an order of magnitude ($10^{-3}$–$5\times$

$10^{-2}$). Interestingly, this value is larger, in magnitude, than the corresponding (theoretical) value for polaron energy in a fully polarized unitary Fermi gas ($\approx -0.6$) [131, 132] by about 10%. It is worth pointing out here that the singlet $pn$ scattering length is about 25% larger than the singlet $nn$ scattering length. This weak density dependence of $\varepsilon_{p\uparrow/\downarrow}$ is a non-perturbative result. Calculations from second order perturbation theory, also shown in the figure, predict a much stronger density dependence for $k_F < 1.0$ fm.

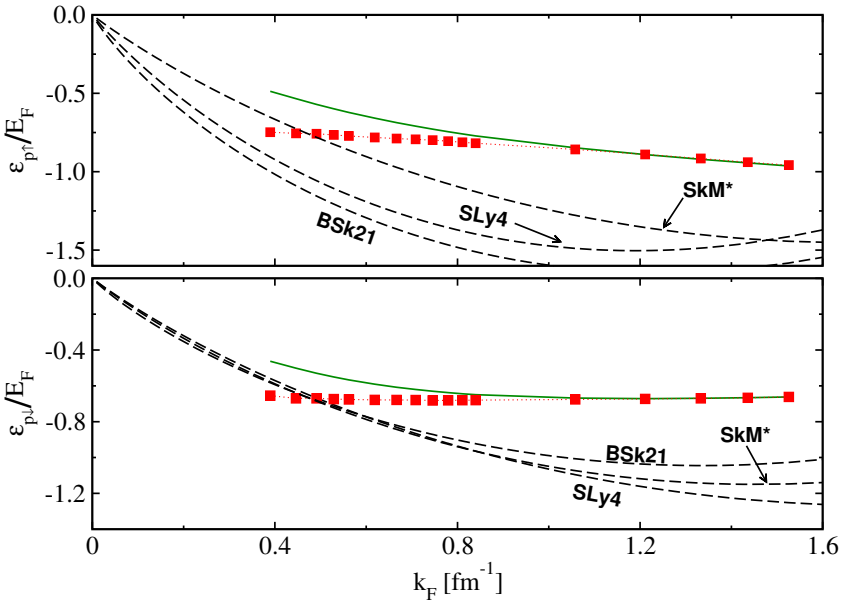


Figure 3.7: The energy of the proton spin-up (top panel) and spin-down (bottom panel) impurities in the units of the Fermi energy of the spin-up neutrons. The red filled squares are our QMC results with the $\mathrm{NNLO_{opt}}$. interaction. The green solid lines are the results from second order perturbation theory. The black dashed lines are predictions from various density functionals (see text).

The EDF for uniform matter is usually parametrized as

$$\mathcal{E} = \mathcal{E}_{\rm kin} + \sum_{t=0,1} \left( C_t^\rho \rho_t^2 + C_t^\tau \rho_t \tau_t + C_t^s s_t^2 + C_t^T s_t T_t \right). \tag{3.2}$$

where $\mathcal{E}_{\rm kin}$ is the kinetic energy density. The isoscalar (isovector) density, spin-density, kinetic density and spin-kinetic density are denoted by $\rho_0, s_0, \tau_0$ and $T_0$ ($\rho_1, s_1, \tau_1$ and $T_1$ ), respectively. The part of the density functional which explicitly depends on the time-odd densities ($s_t$, $T_t$) is the time-odd part, and the rest is the time-even part.

The couplings $C_t^\rho, C_t^\tau, C_t^s$ and $C_t^T$ can only depend on the total (isoscalar) density $\rho_0 = \rho$. In general, they are all independent and should be fixed from available data. However, for EDFs derived from a Skyrme force, there are additional relationships amongst the couplings and the number of independent ones is smaller. Usually the $C_t^\rho$ and $C_t^s$ are assumed to have the form

$$C_t^{(\rho/s)} = C_t^{(\rho/s)0} + C_t^{(\rho/s)\rho} \rho^{(\gamma/\delta)}. \tag{3.3}$$

The impurity energy can be calculated from the EDF as

$$\varepsilon_{\tau\sigma} = \left.\frac{\partial \mathcal{E}}{\partial \rho_{\tau\sigma}}\right|_{\rho_{\tau\sigma}\to 0}, \tag{3.4}$$

with $\tau\sigma = \{n\downarrow, p\uparrow, p\downarrow\}$. In Fig. 3.6 we also show $\varepsilon_{n\downarrow}/E_F$ obtained from a wide cross-section of currently popular EDFs: SLy4 [133, 134, 135], SkM* [136], BSk21 [137], SkP [138], SkO′ [139], SAMi [140], TOV-min [141] and UNEDF-pol [127]. In Fig. 3.7, we show $\varepsilon_{p\uparrow/\downarrow}/E_F$ for a smaller sub-section of the EDFs. This is done in order to avoid over-crowding the figure. However, we would like to note here that the three EDFs, which are plotted in Fig. 3.7, provide a fair representation of the spread in the predictions from the current EDFs; all the other EDFs show very similar trends both qualitatively and quantitatively.

None of the EDFs reproduce the QMC results satisfactorily. This is even more evident in the case of the proton spin-down impurity; whereas all the EDFs predict $\varepsilon_{p\downarrow}/E_F$ to be decreasing with $k_F$, our QMC calculations predict a flat behavior. This is not unexpected since the EDFs are usually fit to the experimental properties nuclear systems near saturation density and low isospin polarization (stable nuclei), and many body calculations of unpolarized neutron matter. On the basis of our calculations we conclude that in order to account for the correlations in the low density matter in the presence of large spin and isospin polarization, *qualitative changes* are warranted in the form of the EDFs.

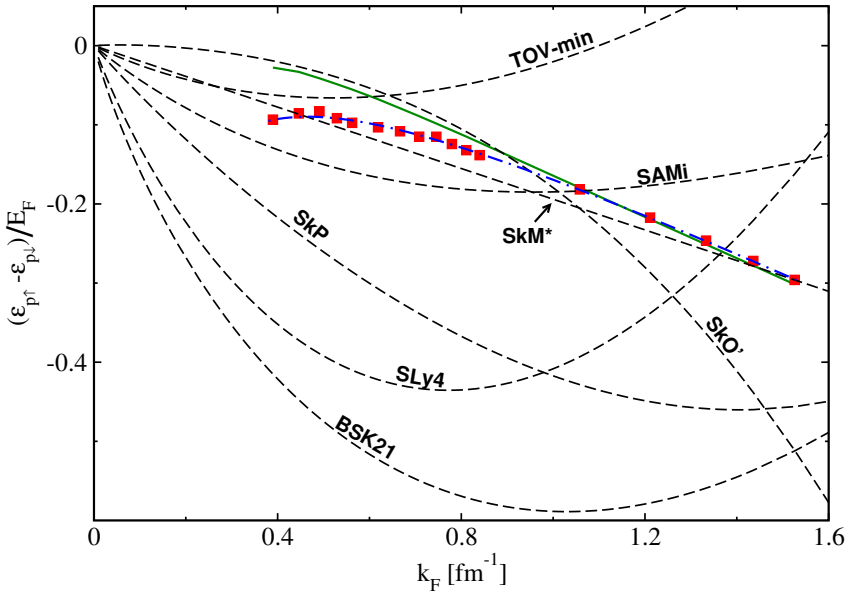


Figure 3.8: The difference between the energies of the proton spin-up and spin-down impurities in the units of the Fermi energy of the spin-up neutrons. The red filled squares are our QMC results with the chiral NNLO$_{\rm opt}$ interaction. The green solid line is the prediction from second order perturbation theory. The blue dot-dashed line is a fit of the form : $A - \frac{B}{k_F|a_s|} - Ck_Fr_e$. The black dashed lines are predictions from various density functionals (see text).

The difference $\varepsilon_{p\uparrow} - \varepsilon_{p\downarrow}$ is a purely time-odd quantity. From Eqs. (3.2) and (3.4) one can easily obtain the following relation

$$\frac{\varepsilon_{p\uparrow} - \varepsilon_{p\downarrow}}{E_F} = \frac{4m(C_0^s - C_1^s)}{3\pi^2\hbar^2} k_F - \frac{2m(C_0^T - C_1^T)}{5\pi^2\hbar^2} k_F^3. \tag{3.5}$$

In Fig.3.8 we compare the predictions from our QMC calculations for $(\varepsilon_{p\uparrow} - \varepsilon p\downarrow)/E_F$ with those from different EDFs. It is clear that none of the EDFs correctly describe our results. The SkM* EDF reproduces the linear part of our results reasonably well. However, the SkM* EDF does not perform any better than the other EDFs for the individual $\varepsilon_{p\uparrow/\downarrow}$. Also, globally the SkM* EDF fares significantly worse than the more modern EDFs in describing experimental data for nuclei (e.g., masses).

Our results are well fit by the form

$$\frac{\varepsilon_{p\uparrow} - \varepsilon_{p\downarrow}}{E_F} = A - \frac{B}{k_F|a_s|} - Ck_F r_e \tag{3.6}$$

with $A = 0.17 \pm 0.01$, $B = 1.4 \pm 0.1$ and $C = 0.101 \pm 0.001$. We have used the values $a_s = -23.75$ fm and $r_e = 2.75$ fm for the neutron-proton singlet scattering length and effective range, respectively. This form is clearly reminiscent of a dilute unitary Fermi gas, the physics of which is clearly missing in the Skyrme EDF. This suggest once more, that in order to obtain a global description of matter in neutron–star conditions a single effective parametrization may not be sufficient and different Density Functionals should be used in regimes with different key physical properties (eg. Unitary vs. Normal Fermi Gas).

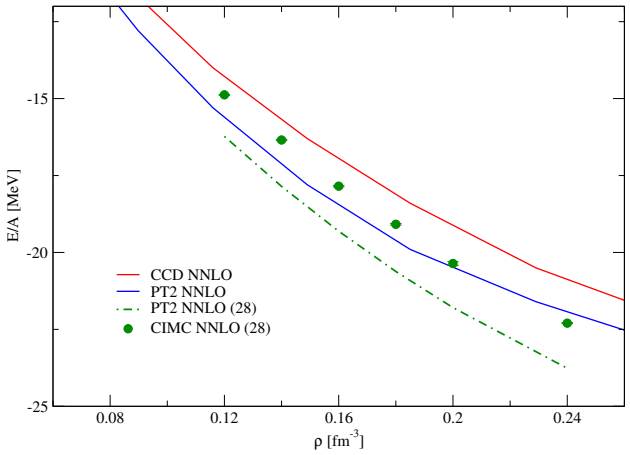


Figure 3.9: Energy per nucleon in Symmetric Nuclear Matter using the NNLO$_{opt}$ interaction. We plot perturbative calculations (PT2) for a system composed by $A = 28$ nucleons (green dash–dotted line) and another with $A = 132$ nucleons (blue line) as well as non–perturbative CIMC calculations with $A = 28$ (green dots) and Coupled–Cluster calculations for $A = 132$ (red curve) from [103].

## 3.3 Symmetric Nuclear Matter

In this section we want to present some preliminary results obtained for Symmetric Nuclear Matter. Calculations have been performed on a small system composed by 28 nucleons (14 protons + 14 neutrons) interacting through four chiral potentials already presented: $NNLO_{opt}$,$N3LO_{500}*$,$N3LO*_{500}$ and $N3LO*_{600}$. We have already presented the first two, the last ones are Entem–Machleidt interactions with the N3LO contact regulators choosen to have the same power (as in $N3LO_{500}*$) but *without* a refitting of the LECs, for cut–off values of either 500 MeV or 600 MeV.

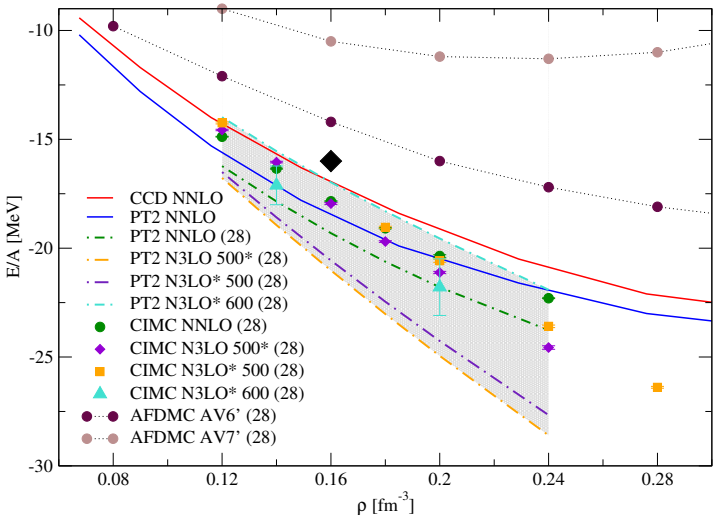


Figure 3.10: The EoS of symmetric nuclear matter: the red (blue) curve is a CCD (PT2) calculation using the $NNLO_{opt}$ interaction ina system of $A$ = 132 nucleons from [103]. The remaining results are obtained with a smaller $A$ = 28 system and employing four different chiral potentials (see text) both in perturbation theory (PT2) and with monte carlo (CIMC). For comparison we also report recent AFDMC results obtained trough the semi–phoenomenological potentials Agronne AV6' and AV7' from [142].The grey band represents the spread of predictions at the PT2 level.

Due to the smallness of the system we use, finite–size effects are an important contribution to the energy per particle (corresponding to $\approx$ 15% at the highest density considered $\rho = 0.28 fm^{-3}$). We can have a feeling of these effects by looking at Fig. 3.9 where we plot the energy per particle obtained using the $NNLO_{opt}$ interaction for two systems: one made of 28 nucleons and a bigger one composed by 132 nucleons. While CIMC and CCD results (green circles and red curve respectively) differ also in the many–body treatment, the two PT2 calculations differ only for finite–size effects and allow to have an estimate of their magnitude. Results found here are consistent with the findings in [142] where a finite–size correction of $\approx 1 MeV$ is found at the empirical saturation point $\rho = 0.16 fm^{-3}$. From Fig.3.10, the overall density dependence of the energy per particle is however quite different from what is found in the AFDMC

calculations: using the four chiral interactions mentioned above we always find over–binding of SNM indicating the need for a repulsive three–body contribution while AFDMC results using either AV6' or AV7' consistently give under–binding pushing for an attractive three–body contribution in the same range. Our results with chiral interactions are consistent with previous Coupled–Cluster [103] as well as Self–consistent Greeen's Function calculations [143] at $T = 5MeV$.

Another interesting feature present in Fig.3.10 is the fact that the dependence on the model hamiltonian of the final resuls changes considerably when more and more correlation effects are taken into account. The grey band represents the spread in the PT2 equations of state calculated with the four different chiral forces, we didn't show the corresponding HF band since it would be out of scale. By looking at the corresponding CIMC results we see that the inclusion of more correlations brings the different results in better agreeement between each other. This shows how delicate may be the estimation of the now popular *theoretical error bands*. It is also evident that a three–body force is needed in order to reproduce the empirical saturation point (black diamond in the graph) and we are actively working in the implementation of these contributions (for now) at the normal–ordering level and we plan to start production runs in the near future. In order to obtain reliable results it would be good to include also triplet contributions in the coupled–cluster trial–wavefunction employed in the random walk, we are now in the process of benchmarking this new piece of algorithm and will produce results soon.

# Chapter 4

# Response Functions and Integral Transforms

The original idea to calculate reaction cross-section with the aid of integral transforms is due to Efros [144] and extended in the past years with the introduction of the Lorentz Integral Transform ([145] or [38] for a recent review), now a well tested method for extracting useful informations about the excitations of nuclear few-body systems.

This rather unconventional approach is based on the consideration that the informations enclosed in the wave-function of the system are quite redundant if we are interested only in the transition matrix elements needed for calculating cross sections. What if we concentrate directly on the matrix element? As we will see in this chapter the closure properties of the hamiltonian eigenstates allow the calculation of these matrix elements using an integral transform and its successive inversion. For some type of integral kernels one can show that the extremely hard problem of exploring the continuum part of spectrum of the system can be turned into a much less problematic bound-state like problem, therefore allowing us to do practical calculations. As we will see, the crucial part of this process is the choice of the integral transform kernel.

In the first study by Efros [144] the Stiltjes transform has been used with successfully in some simple model cases but later, in a test with the deuteron response function (which is computable with standard techniques) it has been found that this form of the integral kernel is rather unsatisfactory since it leads to quite inaccurate results. The main problem is that the Stiltjes transform is closely related to the Laplace one, for which the inversion is the paradigmatic exponentially ill-posed problem (see eg. [31], [32], [33]). This is intimately connected to the structure of the kernel which is of infinite range thus spreading the information contained in the original quantity in the entire transformed space. We will see that in order to achieve better results a kernel of finite range is needed, with width roughly of the order of the information we want to recover.

The chapter is organized with an introduction to the formalism used for treating inclusive scattering processes using integral tranforms. We will then review strengths and weaknesses of different kernel functionslinking them at the end with the inversion techniques used for retrieving the response functions.

## 4.1 General Inclusive Scattering Processes

We will focus on general inclusive process, i.e any reaction of the type:

$$A + B \rightarrow C + X$$

where A, B, C are real particles and X stands for the unobserved remaining reaction products. When we study the cross-section for such processes the quantity of interest is the overlap between the asymptotic initial and final state. In general this has the following form:

$$\mathcal{R}(\omega) = \sum\!\!\!\!\!\!\int \langle Q|\Psi_\nu\rangle\langle\Psi_\nu|Q'\rangle\delta(E_\nu - \omega)d\nu, \tag{4.1}$$

where the states $|\Psi_\nu\rangle$ obey the many-body Schroedinger equation

$$\hat{H}|\Psi_\nu\rangle = E_\nu|\Psi_\nu\rangle, \tag{4.2}$$

and we require the $|\Psi_\nu\rangle$ states to be orthonormal and to form a complete set

$$\sum\!\!\!\!\!\!\int |\Psi_\nu\rangle\langle\Psi_\nu|d\nu = 1 \tag{4.3}$$

The integration and summation in Eq.(4.1) and Eq.(4.3) has to be taken over all discrete and continuum spectrum states in the set.

In the case of perturbation induced transitions we have for the $|Q\rangle$ and $|Q'\rangle$ states

$$|Q\rangle = \hat{O}|\Psi_0\rangle \quad \text{and} \quad |Q'\rangle = \hat{O}'|\Psi_0\rangle$$

where $|\Psi_0\rangle$ is the initial state of the reaction (in our zero–temperature case the ground state of the system), and $\hat{O}$,$\hat{O}'$ are excitation operators inducing the particular transition.

We can now understand $|\Psi_\nu\rangle$ as final states of the reaction and Eq.(4.1) becomes

$$\mathcal{R}(\omega) = \sum\!\!\!\!\!\!\int \langle\Psi_0|\hat{O}^\dagger|\Psi_\nu\rangle\langle\Psi_\nu|\hat{O}'|\Psi_0\rangle\delta(E_\nu - \omega)d\nu \tag{4.4}$$

If $\hat{O} = \hat{O}'$, the quantity in Eq.(4.4) can be interpreted as the contribution to the response of the system to a perturbative probe transferring energy $\omega$ to it.

The cost of a direct calculation of $\mathcal{R}(\omega)$ becomes however rapidly prohibitive as the number of particle in the system or the energy transfer $\omega$ increases. The problem is related to the fact that more and more continuum states contribute to to the response function and the structure of these states is too complicated, even when the number of particles is quite low, mainly due to the existence of many reaction channels.

## 4.2 Integral transform methods

Despite the incredible difficulties that one encounters while trying to evaluate directly Dynamical Responses like Eq.(4.4), a lot of infomations can be accessed without it's explicit evaluation. In fact, some of the properties of $\mathcal{R}(\omega)$ can be determined by looking at integral relations, the so–called *sum–rules*, which are

accessible via the use of the closure property Eq.(4.3). For instance, let us consider the following integrated quantity:

$$\int \mathcal{R}(\omega)d\omega = \langle Q|Q'\rangle.$$

The calculation of this object is much easier than a direct calculation of $\mathcal{R}(\omega)$ because we now only need states $|Q\rangle$ and $|Q'\rangle$. Under general conditions these states have a finite norm, meaning that we can obtain their wave–functions using standard techniques developed for bound–states, which are much more efficient than any scattering wave–function calculation.

The problem with this approach, however, is that this sum–rule contains only a limited information on the original $\mathcal{R}(\omega)$ (merely its norm).

One way to go further and obtain more informations on the spectral function is to consider other integral relations like the *n-th* "momentum" of $\mathcal{R}(\omega)$ for various values of $n$:

$$m_n = \int \omega^n \mathcal{R}(\omega)d\omega, \tag{4.5}$$

whenever these integrals converge to a finite value. For instance by calculating the zeroth, first and second moment ($m_0$, $m_1$ and $m_2$) of $\mathcal{R}(\omega)$ we have sufficient informations to approximate it as a gaussian with norm $m_0$, mean $m_1$ and variance $m_2$. Unfortunately in many interesting cases $m_2$ is not a well defined quantity ($\mathcal{R}(\omega)$ has slower tail). Moreover some of these sum–rules are fixed by external constraints (eg. $m_1$ for density and spin–density responses), so the total amount of information available is further reduced.

The approach that we will pursue in this work is to consider an integral transform with some generic kernel $K(\sigma,\omega)$ such as

$$\Phi(\sigma) = \int K(\sigma,\omega)\mathcal{R}(\omega)d\omega \tag{4.6}$$

Using Eq.(4.1) this yields:

$$\begin{aligned}\Phi(\sigma) &= \int K(\sigma,\omega)\left[\sum\!\!\!\!\!\!\int \langle Q|\Psi_\nu\rangle\delta(E_\nu-\omega)\langle\Psi_\nu|Q'\rangle d\nu\right]d\omega \\ &= \sum\!\!\!\!\!\!\int \langle Q|\Psi_\nu\rangle K(\sigma,E_\nu)\langle\Psi_\nu|Q'\rangle d\nu\end{aligned} \tag{4.7}$$

and by removing the closure relations Eq.(4.3) one obtains

$$\Phi(\sigma) = \langle Q|K(\sigma,\hat{H})|Q'\rangle. \tag{4.8}$$

Equation (4.8) can be viewed as a generalized sum rule which depends on a continuous parameter $\sigma$.

The key point here is that with a proper choice of the integral kernel $K$, the r.h.s. of Eq.(4.8) can be calculated using bound-state type methods, and once the transform is available we can obtain $\mathcal{R}(\omega)$ via an inversion of the transform.

Furthermore using the closures (4.3) one obtains another form for (4.1), maybe unpractical but rather illuminating:

$$\mathcal{R}(\omega) = \langle Q|\delta(\hat{H}-\omega)|Q'\rangle. \tag{4.9}$$

The delta of an operator is a well known quantity in functional analysis, where its called the *spectral density* of the operator.

We see that the best kernel is one that converges in some limit to the spectral density of the Hamiltonian. In other words we should take as our kernel some representations of the delta-function. This is clear also in the perspective of the integral transform inversion since the transform $\Phi(\sigma)$ will look very much like the originating signal $\mathcal{R}(\omega)$, thus allowing an easier inversion.

As is well known there's plenty of such representations but only few of them satisfy the two basic requirements: namely that both the action of $K(\sigma, \hat{H})$ on the state $|Q'\rangle$ must be easy to evaluate and the analytical form of the kernel must permit a practical implementation.

The form Eq.(4.9) suggest immediately another interesting idea linked to the properties of the spectral density: we can use it with $\omega$ equal to an eigenvalue as a projection operator to the corresponding eigenstate. If we manage to find a suitable representation of the spectral density, not only the response function calculation but hopefully even truly excited state calculations can be carried out. Obviously, since we have only a delta representation with a finite width, the projection would not be perfect because of different states contributing:

$$\delta_\epsilon(\hat{H} - \omega)|\psi\rangle \longrightarrow \sum_{\lambda \epsilon [\omega-\epsilon, \omega+\epsilon]} c_\lambda |\psi_\lambda\rangle \tag{4.10}$$

where $\delta_\epsilon$ is a finite representation of a delta–function with width $\epsilon$, and the r.h.s. summation means that the final state will be a superposition of energy eigen–states with energies within a window $[\omega - \epsilon, \omega + \epsilon]$.

This method can be applied only to the discrete part of the Hamiltonian spectrum, provided that the resolution of our delta representation is of the order of the gap between contiguous levels. This approach has been already applied to study excitations on molecular systems by Chan and Booth [146] where a gaussian kernel was used in the framework of the FCIQMC method, we will come back to this later in the chapter.

As final remark, it has been shown (see eg. [147]) that quantities of the same type arise in the exclusive process framework and even in the general non-perturbative reaction case, so the method has a very wide range of applications.

### 4.2.1 Integral kernels

As we have seen, the best kernels for our purposes are those which are representations of the Dirac delta-function. Hereafter we will analyze some of those representations in more detail, focusing on both the capability of using the kernel as a projection operator and for calculating response functions.

#### Laplace

As we have seen in the first–chapter, Quantum Monte Carlo projection is performed in imaginary–time, employing the imaginary–time propagator $\exp(-\tau\hat{H})$. A natural starting point would be to consider exponential functions, for example we can take the following expression:

$$K(\sigma, \omega) = \Theta(\omega - \sigma)\tau e^{-\tau(\omega-\sigma)} \quad \text{with} \quad \tau \to \infty. \tag{4.11}$$

The main problem in using this kernel is the practical implementation of the Heaviside theta function, whose representations are often much more complicated than the delta ones. A similar kernel would be a Stiltjes one which has quite the same form:

$$K(\sigma,\omega) = \Theta(\omega-\sigma)\frac{1}{\tau(\omega+\sigma)} \quad \text{with} \quad \tau\to\infty. \tag{4.12}$$

Once again, we are left with the problem of implementing an operatorial theta function. These two kernels are however employed in almost every Projection Monte Carlo algorithm used today. The former (neglecting the $\tau$ in front of the exponential) in Diffusion-like methods and the latter in Green's function Monte Carlo ones (not the nuclear GFMC which is again a DMC–like algorithm), where the kernels are viewed as imaginary-time Green's functions. The key point in these approaches is that you make an implicit use of an already present theta function coming from the fact that the hamiltonian is bounded from below, ie:

$$\hat{H} \equiv \Theta(\hat{H}-E_0)\hat{H} \tag{4.13}$$

where $E_0$ is the lowest eigenvalue of $\hat{H}$. The limits in Eq.(4.11) and Eq.(4.12) are reached propagating an initial wave-function for a sufficient number of small time-step propagations. In the first case for instance we see that for a sufficiently long projection time $\tau$, and thanks to the spectrum being discrete, the contribution from the first excited state falls exponentially fast towards zero. The problem is that these methods are capable to project only to the ground state of the system, ie. they are useful only with $\sigma \equiv E_0$. If we want now to extend this approach to the case of excited states ( $\sigma \neq E_0$ ) we have to face the problem of inserting a theta function inside the propagator. And we have to do it without introducing any bias.

There are however cases where it is possible to implement correctly this theta function on excited–states, this happens usually when there is a clean way for partitioning the full Hilbert space in disconnected regions. Imagine that the Hamiltonian we looking is invariant under the action of some group $G$ (eg. $SU(2)$ for rotations, $S_N$ for particle statistics,... ), then we have to factorize it using the irreducible representations of $G$. Unfortunately this is not an easy task for the permutation group $S_N$ but it is much easier if we consider eg. rotations. In the latter case in fact, it is relatively easy to write down explicitly projection operators that properly factorize the total Hilbert space.

This is what its used for instance in obtaining the excitation spectrum of nuclei in GFMC calculations (cf. [148]). When this is not fully possible, a complimentary way is to consider correlation functions of properly designed operators (ie. the Casimir operator of the interesting group $G$) and look at the multi–component exponential decay that occurs in imaginary–time. The kernel function used in these approach usually looks like the following:

$$K(\sigma,\omega) = e^{-\frac{\omega}{\sigma}}. \tag{4.14}$$

which closely resembles the Laplace kernel (and has basically all its ill–posedness features). With such kernel the transform of the response function Eq.(4.4) would be

$$\Phi(\sigma) = \langle\Psi_0|\hat{O}^\dagger e^{-\frac{\hat{H}}{\sigma}}\hat{O}|\Psi_0\rangle. \tag{4.15}$$

and using the fact that $|\Psi_0\rangle$ is an energy eigenstate we have:

$$\Phi(\sigma) = \langle\Psi_0|\hat{O}^\dagger(0)\hat{O}(1/\sigma)|\Psi_0\rangle, \tag{4.16}$$

where $\hat{O}(\tau)$ is an imaginary-time Heisenberg operator calculated at imaginary time $\tau$. This quantity is then the imaginary-time auto-correlation function of the operator $\hat{O}$. What is calculated in practice is usually a normalized version of Eq.(4.16)

$$\Phi(\sigma) = \frac{\langle\Psi_0|\hat{O}^\dagger(0)\hat{O}(1/\sigma)|\Psi_0\rangle}{\langle\Psi_0|\hat{O}^\dagger(0)\hat{O}(0)|\Psi_0\rangle}. \tag{4.17}$$

This approach is extensively used in Lattice–QCD calculations, where correlation function are basically the only kind of observable available, but has been also explored in the condensed–matter community with the Projection Operator Imaginary Time Spectral Evolution (POITSE) algorithm [149]. In these cases however one simply drops the theta function and we have no more the connection to a delta–function on the interesting energy range.

These last methods (LQCD and POITSE) can be viewed as an educated–guess inversion of the Laplace transform, and as such they bring in all the troubles connected to integral transform inversions that we will see in the next parts of this chapter.

In order deal with the ill-posedness of the inversion of Laplace transforms, or analytic continuation on real–time axis, many different approaches has been developed and implemented in the past, we will deal with them in Section 4.4.

### Gaussian

Another possibility is the use of a kernel of the following form

$$K(\sigma,\omega) = \sqrt{\frac{\tau}{\pi}}e^{-\tau(\omega-\sigma)^2} \quad \text{with} \quad \tau\to\infty. \tag{4.18}$$

In literature we can find different approaches for calculating the average (4.8) with the gaussian kernel. We will focus here on applications in the condensed–matter/chemistry communities, but we should point out that similar approaches has been pursued in non–perturbative QCD through so–called Gaussian Sum Rules [150]. For example T. Muneihsa and Y. Munehisa [151] used a Trotter-Suzuki decomposition scheme for computing the wave-function

$$|\tilde{Q}\rangle = e^{-\tau(\omega-\sigma)^2}|Q\rangle, \tag{4.19}$$

and then took the scalar product with $|Q\rangle$. This approach has been demonstrated to be useful in the simple cases of the 1- and 3-dimensional harmonic oscillator, but has not been further applied ever since. One disadvantage of this method is the replacement of derivative operators with finite difference operators. This is another ill-posed problem, so we finally have to get rid of two ill-posed problems instead of one.

Another approach has been explored by Kornilovitch [152] who considered the previous wave function as the solution of an initial value problem. In fact

we can see the above state as an evolution of the initial state $|Q\rangle$ in another sort of fictious *time*, an evolution governed by the equation

$$-\frac{\partial}{\partial\tau}|\Psi\rangle = \left(\hat{H}-\sigma\right)^2|\Psi\rangle, \tag{4.20}$$

with the initial condition

$$|\Psi(\tau=0)\rangle = |Q\rangle. \tag{4.21}$$

We can then in principle propagate our $|Q\rangle$ according to Eq.(4.20) and finally take the scalar product with $\langle Q|$.

The use of the square of the Hamiltonian in the evolution equation introduces a substantial drawback in the algorithm since, under rather general assumptions (cf. [152]), the Green's function of Eq.(4.20) is not positive definite in coordinate–space but instead has positive and negative regions. This forces us to face a problem even worse than the Fermion Sign Problem, since in this case it does not seem possible to adopt approximations like the introduction of a nodal surfaces as in fixed-node calculations because now the needed nodal structure changes with the evolution parameter $\tau$.

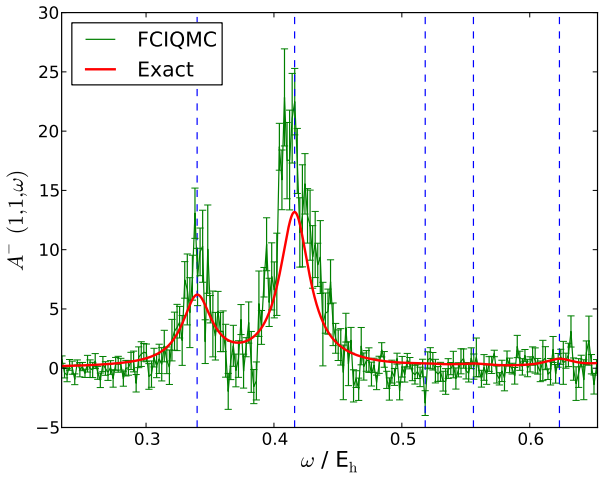


Figure 4.1: Comparison between exact and FCI-QMC calculations of the $A^-(1,1,\omega)$ spectral function (cf. Eq.(9) in [146] ) for the Be dymer (figure from [146]).

This clearly prevents the possibility to deal with more realistic problems than the perturbed harmonic oscillator analyzed in the paper by Kornilovitch, at least in the framework of common coordinate–space continuum PMC methods.

But, as we have seen, coordinate–space continuum PMC methods is not all we have available on the market. In particular a lot of progress has been achieved in tackling the sign problem in Slater–determinant spaces as in the FCIQMC method by Alavi et al. ([23],[60]). In this framework a substantial

alleviation of the sign–problem can be achieved by means of cancellation of opposite signed walkers [153], a route explored with some success also in the continuum Projection MC versions [154] as well as Variational MC with Shadow wave–functions [155]. Employing this kind of cancellation techniques Booth and Chan [146] has shown that it is actually possible to use a Gaussian to both project to excited states and to calculate response function.

The agreement with exact results is remarkably good (cf. Fig. 4.1), especially at low energies, but the accuracy leave still something to be desired. The biggest problem they face in their calculation is actually the attainable width of the gaussian employable. In fact the kernel used in [146] is a linearization of the gaussian which by construction is a rather wide kernel and it is thus difficult to separate different energy components using it.

A possible way forward is to actually sample from a narrower gaussian using a variant of the continuum–time algorithms for the propagation which can be extended quite easily to the gaussian case (cf. Appendix D).

### Lorentz

The Lorentzian kernel is the first one that as been successfully implemented and extensively used for performing calculation of the type we are interested in. Using the integral transform approach previously outlined, Efros et al. [145] were able to construct an algorithm to calculate with good accuracy response functions of nuclear few-body systems: the Lorentz Integral Transform (LIT) method (see [38] for review). This kernel has the form

$$K(\sigma_R, \sigma_I, \omega) = \frac{1}{(\omega - \sigma_R)^2 + \sigma_I^2} \quad \text{with} \quad \sigma_I \to 0. \tag{4.22}$$

By the substitution $\omega \to \hat{H} - E_0$, we find for the transformed response

$$\begin{aligned} Ł(\sigma_R, \sigma_I) &= \left\langle \Psi_0 \left| \hat{O}^\dagger \frac{1}{(\hat{H} - E_0 - \sigma_R)^2 + \sigma_I^2} \hat{O}' \right| \Psi_0 \right\rangle \\ &= \left\langle \Psi_0 \left| \hat{O}^\dagger \frac{1}{(\hat{H} - E_0 - \sigma_R + i\sigma_I)} \frac{1}{(\hat{H} - E_0 - \sigma_R - i\sigma_I)} \hat{O}' \right| \Psi_0 \right\rangle \\ &\equiv \langle \tilde{\Phi} | \tilde{\Phi}' \rangle \end{aligned} \tag{4.23}$$

where $i$ is the imaginary unit. The states $|\tilde{\Phi}\rangle$ and $|\tilde{\Phi}'\rangle$ in the last inner product are solutions of the following Schroedinger-like equations with a source term:

$$(\hat{H} - E_0 - \sigma_R - i\sigma_I)|\tilde{\Phi}\rangle = \hat{O}|\Psi_0\rangle, \tag{4.24}$$

$$(\hat{H} - E_0 - \sigma_R - i\sigma_I)|\tilde{\Phi}'\rangle = \hat{O}'|\Psi_0\rangle. \tag{4.25}$$

Let us suppose that $\hat{O} = \hat{O}'$. Then the transformed response will be simply the $L_2$ norm of the state $|\tilde{\Phi}\rangle$: $Ł(\sigma_R, \sigma_I) \equiv \langle \tilde{\Phi} | \tilde{\Phi} \rangle$. Now, the crucial point is that since $\sigma_I \neq 0$, the integral which defines the transform does exist, or in other words the $L_2$ norm $\langle \tilde{\Phi} | \tilde{\Phi} \rangle$ is finite. This implies that the Lorentz states are localized and so we can use bound-state like techniques in order to solve equations (4.24) and (4.25).

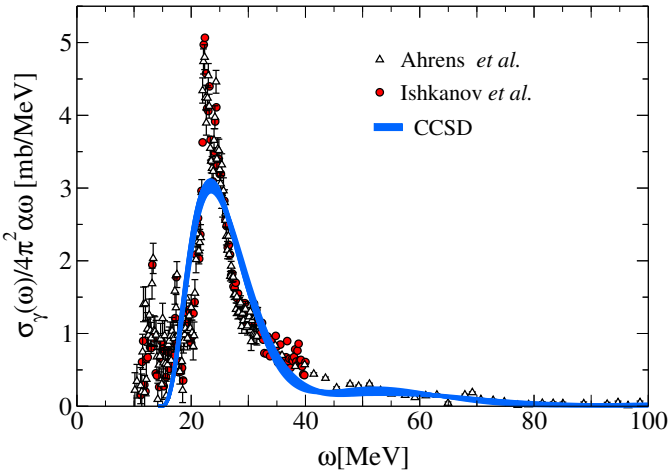


Figure 4.2: Comparison between the dipole response of $^{16}$O obtained trough LIT and Coupled–Cluster in the SD (singles–doubles) approximation and experimental values (figure from [156]).

Once the transform has been calculated, its inversion can be pursued using one of the available regularization techniques.

The LIT method just described has been successfully applied to quite a few physical problems (see [38]). However in the past it has only been applied to systems composed of few particles ($3 \div 7$). This is mostly due to the procedure adopted for solving equations (4.24) and (4.25). The standard way to tackle the problem is a direct approach: one expands the solutions over a set of $N$ basis functions and then directly diagonalize the resulting Hamiltonian matrix. The dimension $N$ of the basis set is chosen to assure convergence of the procedure. When converging, this algorithm provides excellent results, especially when one uses some insight on the problem to choose good basis functions (e.g. Hyperspherical Harmonics). The intrinsic problem is that the number of basis function needed for a given accuracy scales exponentially with system size, thus making impossible in practice to carry on calculations within many–body systems.

A more efficient way that has been explored is using the Lanczos approach (see [38]) for solving the equations for the LIT state. This approach has allowed recently the extension of the LIT method to medium–mass nuclei using Coupled–Cluster techniques, where the Giant Dipole Resonance has been been computed for $^{16}$O and $^{40}$Ca ([156],[157]), in Fig.4.2 we show the results obtained in [156] for the dipole response of $^{16}$O.

**Generalized Sumudu**

In order to design an integral kernel whose transform can be interpreted in the imaginary-time framework the basic idea is to use some linear combination of Laplace kernel. Particularly useful for this purpose is the form

$$K(\sigma,\omega) = e^{-\frac{\omega}{\sigma}}, \tag{4.26}$$

or, limiting ourselves to the case $\omega, \sigma \geq 0$, the following:

$$K(\sigma,\omega) = \frac{1}{\sigma} e^{-\frac{\omega}{\sigma}}. \tag{4.27}$$

The last form is motivated by the fact that Eq.(4.27) is a bell-shaped function in both variables, and by the so-called *initial-value* and $final$-*value* theorems which state that for any function $f(x)$ of a non-negative real variable $x$ the following asymptotic conditions hold:

$$\lim_{\tau \to 0^+} f(\tau) = \lim_{\tau \to +0^+} \frac{1}{\tau} L[f](\frac{1}{\tau}), \tag{4.28}$$

and

$$\lim_{\tau \to +\infty} f(\tau) = \lim_{\tau \to +\infty} \frac{1}{\tau} L[f](\frac{1}{\tau}), \tag{4.29}$$

whenever the limits exists. Mathematicians, motivated by these and other useful properties of the kernel Eq.(4.27), studied the corresponding integral transform for its own right, and called it *Sumudu transform* ([158],[159]).

From our perspective the fact that the height of the peak is a decreasing function of $\tau$ while the width is growing function of $\tau$, is a remarkable feature. In this way, high energy contributions are suppressed while in the low energy region the accuracy is preserved. This allows an efficient study of the low lying excitation spectrum. However, there is still a problem: the resolution of the transform in this case cannot be varied easily as for example in the Gaussian or Lorentzian cases.

The lack of this feature motivated us to search for another similar bell-shaped function made up using exponentials. Consider for example the following functions:

$$K(\sigma,\omega;A,B) = A^{-\frac{\omega}{\sigma}} - A^{-B\frac{\omega}{\sigma}}, \tag{4.30}$$

where A is fixed by requiring the maximum in $\omega/\sigma = 1$ and $B$ is chosen in order to made both parameters as small as possible (big values will require longer imaginary-time simulations). A good–compromise combination was found to be $A = B = 2$.

If we allow both exponents to change independently (ie. as if we add a new $C$ parameter as exponent for the first term) we obtain a more general family of kernels. By also constraining the maximum to be in $\omega/\sigma = 1$ we find the following family of kernels:

$$\tilde{K}(\sigma,\omega;a,b) = \frac{e^{-\mu(a,b)\frac{\omega}{\sigma}}}{\sigma} - \frac{e^{-\nu(a,b)\frac{\omega}{\sigma}}}{\sigma}, \tag{4.31}$$

where

$$\mu(a,b) = \frac{ln[b] - ln[a]}{b-a} a\,; \quad \nu(a,b) = \frac{ln[b] - ln[a]}{b-a} b\,, \tag{4.32}$$

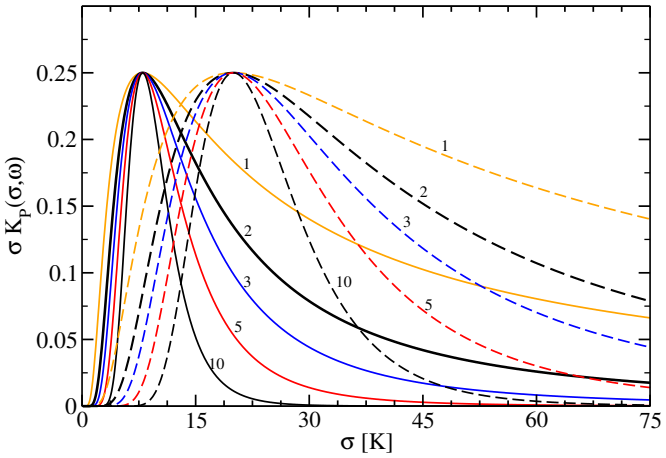


Figure 4.3: Plot of $K_P(\sigma,\omega = 8\,\mathrm{K})$ (full lines) and $K_P(\sigma,\omega = 20\,\mathrm{K})$ (dashed lines), for different values of P. All curves have been normalized to the maximum value of $\sigma K_1(\sigma,\omega)$.

and the parameters $a, b$ are real numbers with $b > a$. The choice $K(\sigma,\omega;2,2)$ for the previous kernel Eq.(4.30) corresponds to $\tilde{K}(\sigma,\omega;1,2)$.

In order to obtain a sharper peak we can use products of such kernels, for instance we define:

$$\begin{aligned} K_P(\sigma,\omega) &= \left(2^{-\frac{\omega}{\sigma}} - 4^{-\frac{\omega}{\sigma}}\right)^P \\ &\equiv \tilde{K}_P(\sigma,\omega;1,2) = K_P(\sigma,\omega;2,2) \end{aligned} \tag{4.33}$$

or more generally we have the following:

$$\tilde{K}_P(\sigma,\omega;a,b) = \left(\frac{e^{-\mu(a,b)\frac{\omega}{\sigma}}}{\sigma} - \frac{e^{-\nu(a,b)\frac{\omega}{\sigma}}}{\sigma}\right)^P . \tag{4.34}$$

As $P$ increases the peak becomes sharper and sharper (see Fig. 4.3) eventually reaching the limit:

$$\lim_{P\to\infty} \tilde{K}_P(\sigma,\omega;a,b) = \tilde{A}_P(\sigma;a,b)\delta\left(\frac{\omega}{\sigma} - 1\right) \quad \forall a,b, \tag{4.35}$$

where $\delta$ is the scaled delta-function and $\tilde{A}_P(\sigma;a,b)$ is a $\sigma$-dependent normalization factor, which is effectively a constant when we do the transformation integral over $\omega$. The calculation in the special case $A_P(\sigma) = \tilde{A}_P(\sigma;1,2) = A_P(\sigma;2,2)$ gives for instance:

$$A_P(\sigma) = \int_0^\infty K_P(\sigma,\omega)d\omega = \frac{\sqrt{\pi}}{\ln(2)} 2^{-2P} \frac{\Gamma(N)}{\Gamma(P+\frac{1}{2})}\sigma = c_P\sigma. \tag{4.36}$$

Due to the new $\sigma$ dependence, the resulting normalized function has a shifted maximum position. In order to restore the maximum at the wanted point $\frac{\omega}{\sigma} = 1$

we can simply to change the numerical factor 2 with a numerically optimized one for every choice of $P$:

$$\mathcal{K}_P(\sigma,\omega) = \frac{1}{\sigma}(\beta_P{}^{-\frac{\omega}{\sigma}} - \beta_P{}^{-2\frac{\omega}{\sigma}})^N \tag{4.37}$$

where the first values of the parameters are: $\beta_1 = 4.2443$, $\beta_2 = 2.8906$, $\beta_3 = 2.5523$ and $\beta_4 = 2.3998$.

Using a binomial expansion, and rewriting powers as exponential functions, leads to a form of the kernel that is a linear combination of the so-called Sumudu transform kernels [158], and is more transparent in view of a QMC calculation[1]:

$$\mathcal{K}_P(\sigma,\omega) = \frac{1}{\sigma}\sum_{k=0}^{P}\binom{P}{k}(-1)^k e^{-\ln(\beta_P)(P+k)\frac{\omega}{\sigma}}. \tag{4.38}$$

or more generally

$$\tilde{\mathcal{K}}_P(\sigma,\omega;a,b) = \frac{N}{\sigma}\sum_{k=0}^{P}\binom{P}{k}(-1)^k e^{-\ln(b/a)[\frac{a}{b-a}P+k]\frac{\omega}{\sigma}}. \tag{4.39}$$

With the substitution $\omega \to \hat{H}$ we arrive to a simple linear combination of imaginary-time propagators taken at imaginary-time

$$\tau = (\ln(\beta_N))(N+k))/\sigma$$

and

$$\tau = \ln(b/a)[\frac{a}{b-a}P + k]/\sigma$$

respectively.

One problem is that this transform kernel is well-defined only for $\sigma, \omega > 0$ but in the general case the Hamiltonian has an entire discrete spectrum in the negative energy region. This will hurt our transform process since for values of $\omega$ below zero the kernel starts to diverge and so unwanted parts add to our transform. Fortunately, in response function calculations, $\omega > 0$ since it represents the energy transfer, so in practice we consider $\hat{H}' = \hat{H} - E_0$ and no problem should arise. It is however easy to find a version of the transform well-defined for $\omega \in (E_0, \infty)$ and any finite $E_0$. Consider for example

$$\mathcal{K}'_P(\sigma,\omega) = \frac{1}{\sigma}\sum_{k=0}^{P}\binom{P}{k}(-1)^k e^{-\ln(\beta_P)(P+k)\frac{\omega-E_0}{\sigma-E_0}}. \tag{4.40}$$

The kernel $\mathcal{K}'_P$ can be useful for instance when we want to use the transform as a projection operator.

We can now write down the full expression for our transform of the response function:

$$\begin{aligned}\Phi(\sigma) &= \int_0^\infty \mathcal{K}_P(\sigma,\omega)\langle\Psi_0|\hat{O}^\dagger\delta(\hat{H}'-\omega)\hat{O}'|\Psi_0\rangle d\omega \\ &= \langle\Psi_0|\hat{O}^\dagger\mathcal{K}_P(\sigma,\hat{H}')\hat{O}'|\Psi_0\rangle\end{aligned} \tag{4.41}$$

[1]The presence of the inverse $\sigma$ power in the transform, which amplifies contributions coming from low energy, are not necessarily useful in numerical calculations and we usually work directly with the un–scaled versions like (4.33).

so that

$$\Phi(\sigma) = \frac{1}{\sigma}\sum_{k=0}^{P}\binom{P}{k}(-1)^k\langle\Psi_0|\hat{O}^\dagger e^{-(\ln(\beta_P))(P+k))\frac{\hat{H}'}{\sigma}}\hat{O}'|\Psi_0\rangle \tag{4.42}$$

Following what we have done with the Laplace-kernel we eventually arrive to

$$\Phi(\sigma) = \frac{1}{\sigma}\sum_{k=0}^{P}\binom{P}{k}(-1)^k e^{\tau_{Pk}(\sigma)E_0}\langle\Psi_0|\hat{O}^\dagger(0)\hat{O}(\tau_{Pk}(\sigma))|\Psi_0\rangle \tag{4.43}$$

where

$$\tau_{Pk}(\sigma) = (\ln(\beta_P))(P+k))/\sigma$$

is the usual imaginary-time value at which we have to take the auto-correlation samples, and the exponential factor is just a constant (in $\omega$) arising from the fact we have used $\hat{H}'$ instead of $\hat{H}$.

Finally we see that all we have to do to compute this transform is the same calculation of imaginary-time correlation function from which we can construct the linear combination seen ahead. To take the limit $P \to \infty$ we have to know the correlation function for extremely long imaginary-time. This might indeed be complication for the QMC calculation.

There will be eventually a computational limit mainly for two reasons: the first one is a numerical precision problem due to the presence of binomial coefficients. With high values of $P$, these coefficients grows rapidly and soon the series in the previous equations will be numerically ill-behaved due to the bad balance between summands. To prevent this, high precision arithmetic is necessary and this complicate the whole method a lot. In numerical test cases we have seen that this limit is generally reached for $P \approx 100 \div 200$.

We have found however that in some cases it does not seem necessary to take very large values of $P$ to extract useful informations. For example in our calculations a typical value of $N = 2$ has been fruitfully adopted. For a finite $P$ at each value of $\omega$ the kernels presented above have a finite width that depends on $P$ and that represents a sort of *resolution* at which one can study the DSF. Moreover the maximum can be fixed at will around $\omega = \sigma$. Therefore, the main advantage is that one can choose both the energy range of interest (the $\sigma$ values) and the resolution (larger values of $P$ correspond to higher resolution) for the study of the DSF. This makes the approach quite flexible, similarly to the case of the LIT method.

## 4.3 Ill-posed problems

The concept of a well-posed problem in mathematical physics was formulated at the beginning of the last century by the french mathematician Hadamard. The idea was that problems whose solutions do not satisfy certain continuity conditions should not be regarded as physically relevant. These necessary defining conditions for a *well–posed* problems are the following

1. a solution for the problem exist
2. the solution is unique
3. the solution depends continuously on the data of the problem

Conversely, any problem for which these rules do not hold is named *ill-posed* in the sense of Hadamard. From a practical point of view the main restriction is the third request since typically physical data are affected by noise and the presence of discontinuities may destroy any attempt to obtain the solution starting from those data with a sufficient accuracy.

A typical example of an ill-posed problem is the Cauchy problem for the Laplace equation: uniqueness of the solution can be proved (see [160]) but we will see that the solution depends non–continuously on the data. Let us consider

$$\Delta f(x,y) = 0 \quad \text{with} \quad f(x,0) = 0 \quad \frac{\partial}{\partial y} f(x,y)|_{y=0} = \eta \sin nx, \tag{4.44}$$

with $x \in [0,\pi]$ and $y > 0$, the solution is readily found to be

$$f(x,y) = \frac{\eta}{n} \sin nx \sinh ny. \tag{4.45}$$

If we now want to find the solution $f$ for some fixed $y > 0$ using the Cauchy data at $y = 0$ we encounter the following problem: for any choice of $\epsilon$ , $\delta$ and $y$ we can always find $\eta$ and $n$ such that

$$\|\eta \sin nx\| < \delta \qquad \left\| \frac{\eta}{n} \sin nx \sinh ny \right\| > \epsilon, \tag{4.46}$$

hence for any arbitrary small variation in the input data, the resulting variation in the output solution can be arbitrary large.

In this work we are focused on integral equations, which are one of the main methods of investigating boundary value problems, such as our Schroedinger equation in a finite simulation box. In particular well-posed boundary value problems reduces to Fredholm integral equations of the second kind:

$$\phi(y) + \lambda \int K(x,y)\phi(x)dx = f(y). \tag{4.47}$$

Conversely, ill-posed problems can be casted into Fredholm integral equations of the first kind, much harder to study. The equation defining an integral transform such as (4.37) are just a particular example of integral equations of the first kind:

$$\int K(x,y)\mathcal{R}(x)dx = \Phi(y). \tag{4.48}$$

It turns out that the solution $\mathcal{R}$ does not depend continuously on the input $\Phi$ and so the inversion of such equation is an ill-posed problem. To see this let us consider a variation in the input $\Phi \to \Phi + \Delta\Phi$ and suppose that the corresponding variation of the solution is $\Delta\mathcal{R} = A \sin kx$. One can see by Fourier analysis that when $k$ becomes sufficiently large the corresponding $\Delta\Phi$ can be arbitrary small. Therefore even with relatively precise data, without any regularization procedure, highly oscillatory noise components can be superimposed to the signal eventually destroying the quality of the computed $\mathcal{R}$.

### 4.3.1 SVD Analysis

It is possible to characterize in a more quantitative way the role played by the choice of the kernel, by looking at its Singular Value Decomposition (SVD). We

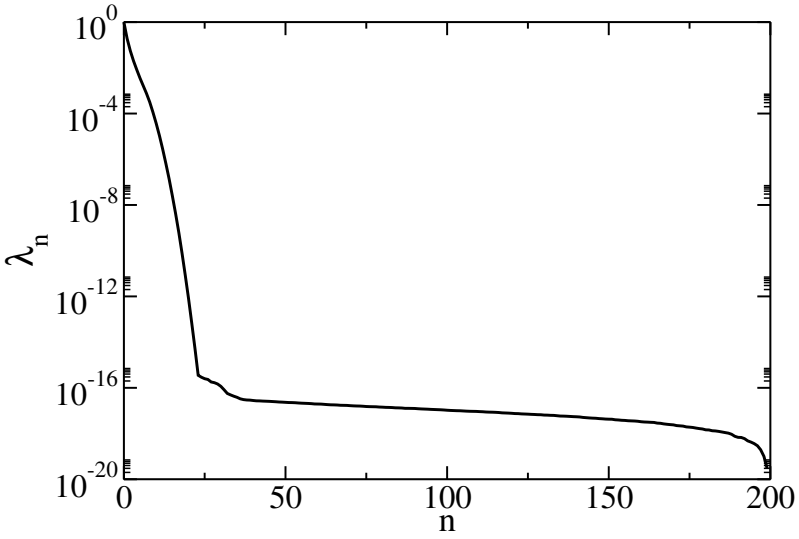


Figure 4.4: Eigenvalues of the SVD for the Laplace kernel on a N=200 mesh points grid. A $\delta$-function would give all eigenvalues equal to one.

start by discretizing the integral equation (4.6) on a $N$-point grid

$$\Phi(\sigma) = \int K(\sigma,\omega)\mathcal{R}(\omega)d\omega \;\rightarrow\; \Phi_i = \sum_k^N K_{ik}\mathcal{R}_k \;\; i \in [1,N] \tag{4.49}$$

where we have defined

$$\Phi_i \equiv \Phi(\sigma_i) \quad K_{ik} \equiv \alpha_k K(\sigma_i,\omega_k) \quad \mathcal{R}_k \equiv \mathcal{R}(\omega_k) \tag{4.50}$$

and $\alpha_k$ are the coefficients used for the particular integration scheme employed. We can now apply the SVD to the kernel-matrix $K$ to produce the following factorization

$$K = U\Lambda V^T \;, \quad U,V,\Lambda \in \mathbf{R}^{NxN} \tag{4.51}$$

with $U$,$V$ orthogonal matrices and $\Lambda = diag[\lambda_1,\ldots,\lambda_N]$. The positive–definite elements on the diagonal of $\Lambda$ are called *singular–values* and can be organized in descending order: $\lambda_1 > \lambda_2 > \ldots > \lambda_N$, while the column–vectors of $U$, and $V$, $\bar{u}_i$ and $\bar{v}_i$ , are called left and right singular–vectors respectively. Usually when dealing with integral transforms (Fredholm integral equation of the 1st kind) the rate of decay of singular–values $\lambda_n$ is at least exponential in $n$ (eg. see Fig. 4.4), and the singular vectors $\bar{u}_i$ and $\bar{v}_i$ can be viewed as discrete functions with an increasing number of sign changes. In the continuum limit these would be functions with an increasing number of nodes, therefore corresponding to contributions with increasing frequencies.

Using this decomposition we can obtain explicit expressions for both the direct and inverse problem

$$\bar{\Phi} = K\bar{S} = \sum_j^N \lambda_j(\bar{v}_j,\bar{S})\bar{u}_j \tag{4.52}$$

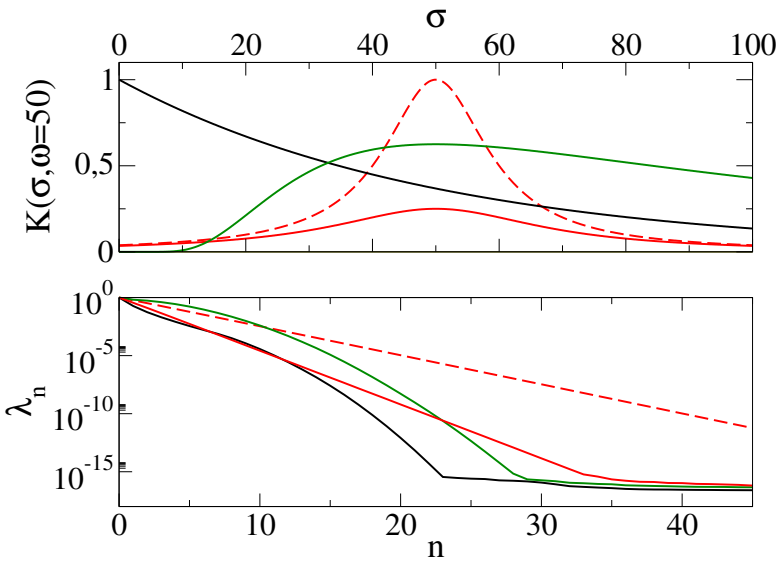


Figure 4.5: Upper panel: Comparison between Lorentz kernel (red curves) with width 20 (continuous line) and 10 (dashed line), a Sumudu kernel with $P = 2$ and $b = 2a = 2$ (solid green curve), and a Laplace kernel (solid black curve). Lower panel: the corresponding singular values for the kernels of the upper panel.

$$\bar{\mathcal{R}} = K^{-1}\bar{\Phi} = \sum_{j}^{N} \frac{(\bar{u}_j, \bar{\Phi})}{\lambda_j} \bar{v}_j \tag{4.53}$$

were $(\bar{a}, \bar{b})$ here denotes the scalar product of two vectors. We will show that in this form it is easier to appreciate where the ill-posed nature of the inverse problem resides.

The solution of the direct problem $\bar{\phi}$ is expressed on the basis set spanned by the left singular–vectors $\bar{u}_j$ with coefficients that are proportional to the singular–values and thus are damped exponentially fast as the index $j$ grows. Due to this *low–pass filter* feature, it is usually said that the integral transform is a *smoothened* version of the original signal.

On the contrary in the inverse problem the coefficients of the expansion on the basis given by the right singular-vectors $\bar{v}_j$ are exponentially amplified raising the index $j$. A necessary requirement in order to obtain anything meaningful out of it is for the overlaps $(\bar{u}_j, \bar{\Phi})$ to decay faster to zero than the singular values, and this is a really strong constraint when the transform is computed with finite precision.

In practical situations the singular–value decay is so fast that just the first few have a meaning because after a while the number gets completely corrupted by floating-point errors (see Fig. 4.4), and thus one expects meaningful results just for the first few terms in the sum appearing in Eq.(4.53). This is a sign of the fact that when one discretize an ill–posed problem the corresponding discrete problem is numerically ill–conditioned or in other words the problem is not stable with respect to uncertainties in the input.

The decay rate of the singular values towards zero can be used as an indication of the *degree of ill-posedness* of the problem: the faster the singular values goes to zero the worst is the impact of the ill-posed nature of the problem. This can be understood by initially noticing that for a $\delta$-function kernel all the singular values are one. When a function with a finite width is used, the SVD yields eigenvalues that start deviating more and more from this limit: the larger the width the faster the decay. However, the SVD picks up not just information about the width, but also about the behavior of the function in the tails.

As an example, in Fig. 4.5 we compare the SVD of a Laplace kernel, two Lorentz kernels with different width, and a Sumudu kernel of a given width. The plot clearly shows that while the Sumudu kernel underperforms with respect to the Lorentz kernels, it widely overperforms the Laplace kernel. This is the key point of this part of the work: while it is not possible for technical reasons related to the nature of Quantum Monte Carlo algorithms to use an optimal kernel form as a Guassian or a Lorentzian, which are good representations of a $\delta$-function with separately tunable center and width, we have found a kernel that, as discussed in the following, is 1) suitable for being used in projection QMC calculation, and 2) is a qualitatively and quantitatively better choice than a Laplace kernel. This prescription sets a more efficient way of analyzing QMC data in order to obtain information about the response function. Its application will result in an *a–priori* milder ill–posedness of the inversion problem, which will in any case benefit of very efficient inversion schemes. The main advantage here, is that almost no previous knowledge of the spectrum is required, and calculations can be predictive. However, there is an even more important point: the fact that the kernel $K_P(\sigma, \omega)$ tends to the $\delta$-function when $P \to \infty$ tell us that *in principle*, if we could perform a calculation for very large $P$, we might get to the limit at which some information, such as the position of the peaks, has no need of any inversion to be extracted. This fact has been exploited, for example, in nuclear dynamics calculations [156].

## 4.4 Regularization techniques

In this section we want just to give a rough idea of inversion techniques since our focus is on the integral transforms by themselves.

Regularization procedures (see eg. [147],[38]) are practical methods to circumvent the ill–posed nature of the problem at hand by suppressing the unwanted noise components that may appear in approximate solutions. The idea is that the original ill-posed problem is replaced by a well-posed one that includes a regularization parameter $r$. The regularized solution of this new problem $R(x, r)$ now depends continuously on the data $T(y)$ and, with the true $T(y)$, the solution is arbitrarily close to $R(x)$ for a *proper* choice of $r$. Differences between regualarization methods stands mainly in the choice of the regularization parameter and in the procedure adopted to find its "*proper*" value.

Over the years many powerful inversion schemes were developed in a wide range of contexts, among them we find the popular Maximum Entropy Method [161, 162, 163] (MEM), or others like the Average Spectrum Method (ASM) [164] and the Stochastic Analytic Continuation (SAC) [165]. Recently the Genetic Inversion via Falsification of Theories (GIFT) [34] has been proposed and ap-

plied quite successfully to superfluid $^4$He. Also an hybrid MEM–SVD inversion scheme ([166] for details) has been applied at finite temperatures with both a Unitary Fermi Gases ([167]) and neutron matter [168]. When the number of extramal points in the solution is known beforehand the inversion method by Efros [169] may offer a valid alternative too.

We shall start with a technique widely used in LIT calculations which has a straightforward implementation and still allows to keep uncertainties at a sufficiently low level. The solution of eq (4.48) is represented as the sum of the first $N$ functions of a complete set $\{\psi_n(x)\}$

$$R(x,N) = \sum_{n=1}^{N} \alpha_n \psi_n(x,\vec{\eta}) \tag{4.54}$$

where $\vec{\eta}$ are possible non-linear parameters. Here the role of the regularization parameter is played by the value $N$ of basis functions included, which for example can be taken of the following bell-shaped form (widely used in LIT calculations [147])

$$\psi_n(x,\vec{\eta}) = x^{\eta_1} exp(-\frac{\eta_2}{n}x) \tag{4.55}$$

Expression (4.55) is then transformed into the corresponding $T_n(y,\eta)$ and the linear coefficients $\alpha_n$ can be found by a least-square fit of the measured $T(y)$. This approach proved very successful in various benchmark LIT calculations ([38]) where it was found the existence of a range of $N$ values where the solution is stable, hence showing the accuracy of the procedure.

The above mentioned method is well-suited especially when dealing with spectra with a single distinct peak, as is the case for liquids at large momentum transfer (incoherent response). Another important point is that within this regularization approach one needs only values of $T(y)$ over a limited range of $y$, thus enabling the possibility to study just the region of the spectrum we are interested in. We will use this approach as inversion technique in the next chapter.

Speaking more generally, when dealing with regularization techniques one is usually confronted with a minimization problem of the form:

$$\min_{\bar{f}} \; D\left[K\bar{f},\bar{g}\right] + \alpha L\left[\bar{f}\right] \tag{4.56}$$

where $\bar{g}$ is the available data, $D$ is a likelihood function such as the euclidean distance or the Chi–squared, $L$ is a penalty function that tries to reduce noise components by enforcing smoothness in the final solution and finally $\alpha \in [0,1]$ is the regualarization parameter that controls the balance between fitness to the data (small alpha) and smoothness of the solution. For instance a widespread method is the Tikhonov regularization in which the solution to the equation $K\bar{f} = \bar{g}$ is replaced by the solution to the following (regularized) Least Squares equation:

$$\min_{\bar{f}} \; \|K\bar{f} - \bar{g}\|^2 + \alpha\|\Gamma\bar{f}\|^2 \tag{4.57}$$

where the Tikhonov matrix $\Gamma$ can be the identity $I$ or a discrete version of a derivative operator $D_1$ or $D_2$. In either case the role of the second term is to reduce the norm of high frequency components in the solution and one has to

search for a sufficiently low value for $\alpha$ such that solutions are stable to small variations in the input.

Similarly, in the Maximum Likelihood methods that we will use for studying superfluid $He^4$, one considers the following Cross–Entropy minimization problem:

$$\min_{\bar{f}} \; KL\left[K\bar{f}, \bar{g}\right] + \alpha KL\left[\bar{f}, \bar{f}_0\right] \tag{4.58}$$

where KL is the Kullback-Leibler divergence that measures of the difference between two probability distributions

$$KL\left[\bar{a}, \bar{b}\right] = \sum_n a_n log(a_n/b_n) + b_n - a_n$$

and $\bar{f}_0$ is some prior estimate of $\bar{f}$, usually we used a positive constant in order to reduce the amount of external information that we put in the inversion procedure. Tha main advantage of this formulation is that by construction every signal, whether input or output, should be positive definite which simplifies the application of this to the inversion of spectral functions. The particular form of the likelihood function in this case also allows for very efficient implementation of the minimization process.

# Chapter 5

# RMC in coordinate–space for bosons

The coordinate–space representation is a particularly useful basis to work with, and as such it has been widely used in literature in a variety of sub–fields for the representation of the Schroedinger equation and its solution. From the Monte Carlo perspective the two most interesting features offered by coordinate–space are the possibility to find efficient representations for both the imaginary–time propagator and the guiding–wavefunction $\Psi_G$ used for the stochastic evolution. The quality of the data acquired by sampling along the random walk is usually quite sensitive to the quality of $\Psi_G$, and RMC is an example of an algorithm which is particularly sensitive to this. For instance we will use a guiding–wavefunction for the bulk superfluid $He^4$ case that contains explicit two– and three–body correlations. The coordinate–space formulation allows us to handle this complicated wave–function without efficiency problems even when the number of particles in the system becomes a few hundred.

In the following section we will set the stage by introducing Diffusion MC in coordinate–space, and will further proceed by presenting the details of RMC algorithm implementation in this basis.

## 5.1 Langevin dynamics and the Schroedinger equation

Let us start by reviewing briefly a well–studied random process: the Langevin random–walk, which is at the hearth of the success of most of the Quantum Monte Carlo implementations in coordinate–space. Here and in the following we will use $\mathbf{R}$ as a shorthand for the $dN$–dimensional vector containing the coordinates of a $d$–dimensional system with $N$ degrees of freedom.

The Langevin random–walk is a generalization of the well–known Brownian motion where we allow for the presence of an external force field $W(\mathbf{R})$. Its one step dynamics is governed by the following equation:

$$\mathbf{R}' = \mathbf{R} + D\Delta\tau\mathbf{F}(\mathbf{R}) + \xi \tag{5.1}$$

where $\mathbf{F}(\mathbf{R}) = -\nabla W(\mathbf{R})$ is the *drift force* given by the external force field $W(\mathbf{R})$, $D$ is a diffusion coefficient, $\Delta\tau$ is the discretized time interval and $\xi$ is a $dN$-dimensional gaussian random number with zero mean and variance $2D\Delta\tau$.

The corresponding transition probability for the process $\mathbf{R} \to \mathbf{R}'$ is

$$\mathcal{W}(\mathbf{R}', \mathbf{R}, \Delta\tau) = \frac{1}{(4\pi D\Delta\tau)^{\frac{3N}{2}}} \exp\left(-\frac{(\mathbf{R}' - \mathbf{R} - D\Delta\tau\mathbf{F}(\mathbf{R}))^2}{4D\Delta\tau}\right), \tag{5.2}$$

and we can then use it to generate a Markov chain starting from some initial distribution $P_0(\mathbf{R})$. In order to recover the Brownian motion limit we can just set the force–field to zero; in this way we recover the familiar gaussian transition probability.

One can proceed further and then show that the equilibrium distribution of the dynamics governed by Eq.(5.2) is given by:

$$\begin{aligned} &\lim_{N\to\infty} \int d\mathbf{R}_0 \dots d\mathbf{R}_N \mathcal{W}(\mathbf{R}_N, \mathbf{R}_{N-1}, \Delta\tau) \dots \mathcal{W}(\mathbf{R}_1, \mathbf{R}_0, \Delta\tau) P(\mathbf{R}_0) \\ &\quad = \lim_{N\to\infty} \mathcal{W}^N P_0 \longrightarrow \exp(-W(R)). \end{aligned} \tag{5.3}$$

In fact the Langevin random walk asymptotically samples the unique stationary solution of the Fokker-Planck equation:

$$\frac{\partial \mathcal{P}(\mathbf{R}, t)}{\partial t} = \hat{F}\mathcal{P}(\mathbf{R}, t), \tag{5.4}$$

here $\hat{F}$ is the Fokker-Planck operator

$$\hat{F} = D\frac{\partial^2}{\partial \mathbf{R}^2} - D\frac{\partial W(\mathbf{R})}{\partial \mathbf{R}}\frac{\partial}{\partial \mathbf{R}}, \tag{5.5}$$

and $\mathcal{P}(\mathbf{R}, t)$ represents the probability to find the system, undergoing thermal motion under the influence of the force field $W(\mathbf{R})$, in the configuration $\mathbf{R}$ at the time $t$. As anticipated, the unique stationary solution of this equation is in fact given by

$$\mathcal{P}_{\mathcal{S}}(\mathbf{R}) = \lim_{t\to\infty} \mathcal{P}(\mathbf{R}, t) = \exp(-W(\mathbf{R})).$$

As one can directly see from (5.4) the Fokker-Planck equation is quite similar to the Schroedinger equation that we ultimately are willing to solve. So, once a complete correspondence between the two has been established, it would be straightforward to use classical systems undergoing Langevin dynamics to simulate the corresponding imaginary time-dynamics of the quantum system.

To establish this classical-to-quantum analogy one can simply made the following transformation (reminiscent of importance–sampling):

$$\mathcal{P}(\mathbf{R}, t) = \Psi(\mathbf{R}, t)g(\mathbf{R}) \quad \text{with} \quad g(\mathbf{R}) \propto exp(-W(\mathbf{R})), \tag{5.6}$$

and by inserting this expression in (5.4) we obtain

$$\frac{\partial \mathcal{P}(\mathbf{R}, t)}{\partial t} = \hat{F}\mathcal{P}(\mathbf{R}, t) \quad \Longleftrightarrow \quad \frac{\partial \Psi(\mathbf{R}, t)}{\partial t} = -\hat{\mathcal{H}}\Psi(\mathbf{R}, t), \tag{5.7}$$

where

$$\hat{\mathcal{H}} = -D\frac{\partial^2}{\partial \mathbf{R}^2} + D\frac{1}{g(\mathbf{R})}\frac{\partial^2 g(\mathbf{R})}{\partial \mathbf{R}^2} \tag{5.8}$$

is the hamiltonian of some fictious quantum system that we can describe employing the classical system obeying Eq.(5.4). By simple inspection one can see that $g(\mathbf{R})$ is the bosonic ground–state of such system with zero eigenvalue.

Let us now turn to the Schroedinger equation in coordinate–space, considering a local potential $\langle \mathbf{R}'|\hat{V}|\mathbf{R}\rangle = \delta(\mathbf{R}-\mathbf{R}')V(\mathbf{R})$ it has the following form:

$$\begin{aligned} -\frac{\partial \Psi(\mathbf{R},\tau)}{\partial \tau} &= -D\nabla^2\Psi(\mathbf{R},\tau) + (V(\mathbf{R}) - E_R)\,\Psi(\mathbf{R},\tau) \\ &= \hat{T}\Psi(\mathbf{R},\tau) + \hat{V}\Psi(\mathbf{R},\tau) - E_R\Psi(\mathbf{R},\tau) \end{aligned} \tag{5.9}$$

where $E_R$ is a reference energy used to control the normalization of the propagated wave-function during the simulation, and the *diffusion coefficient* is now D=$\hbar^2/2m$. The first term in the r.h.s. of Eq.(5.9) leads to a diffusive process like the one described above while the second term leads to a branching process where it acts as sink/source (depending on its sign) for the probability density in $\mathbf{R}$.

Since we are dealing with bosons we can consider $\Psi(\mathbf{R},\tau)$ to be positive semi-definite, and as such it can be interpreted as the probability density of a suitable random walk that mimics these simultaneous diffusion and branching processes. Diffusion Monte Carlo in coordinate–space can be in fact implemented in this way, using a gaussian transition probability like Eq.(5.2) with $F = 0$

$$K(\mathbf{R}',\mathbf{R}) = \frac{1}{(4\pi D\Delta\tau)^{\frac{dN}{2}}}\exp\left(-\frac{(\mathbf{R}'-\mathbf{R})^2}{4D\Delta\tau}\right), \tag{5.10}$$

and then reweighting the walkers arriving at $\mathbf{R}$ by the exponential factor

$$B(\mathbf{R}) = \exp\left(-\Delta\tau\,(V(\mathbf{R}) - E_R)\right), \tag{5.11}$$

so that the short time propagator is given by

$$\begin{aligned} G(\mathbf{R},\mathbf{R}',\Delta\tau) &= \frac{1}{(4\pi D\Delta\tau)^{\frac{dN}{2}}}\exp\left(-\frac{(\mathbf{R}'-\mathbf{R})^2}{4D\Delta\tau}\right)\exp\left(-\Delta\tau\,(V(\mathbf{R}) - E_R)\right) \\ &= K(\mathbf{R}',\mathbf{R})B(\mathbf{R}). \end{aligned} \tag{5.12}$$

This factorized form for the Green's function with the transition to new state governed solely by the non–interacting part of the Hamiltonian is a key ingredient for the success of MC in coordinate–space. This expression for the short–time Green's function can be motivated by employing a Trotter–Suzuki decomposition of the imaginary–time propagator

$$e^{-\Delta\tau(\hat{T}+\hat{V})} = e^{-\Delta\tau\hat{T}}e^{-\Delta\tau\hat{V}} + O(\Delta\tau^2). \tag{5.13}$$

We then see that expression (5.18) would be appropriate for sufficiently small imaginary–time intervals $\Delta\tau$.

The presence of singularities in the interaction $V(\mathbf{R})$ (as in e.g. hard–core potentials) deteriorates considerably the efficiency of the simulation, this due to the large fluctuations in the branching factor $B(\mathbf{R})$ used for the reweighting.

In principle reducing $\Delta\tau$ helps in lowering these fluctuations but then both the convergence to the ground state ($\tau \to \infty$) and the quality of the simulation data would be greatly affected due to larger auto–correlations. The solution to this problem arrives, once again, from Importance Sampling.

Let us choose some guiding wave–function $\Psi_G(\mathbf{R})$ and define a new (mixed) probability density $\xi(\mathbf{R},\tau) = \Psi(\mathbf{R},\tau)\Psi_G(\mathbf{R})$. The Schroedinger equation (5.9) can be easily recasted in the following form:

$$\frac{\partial \xi(\mathbf{R},\tau)}{\partial \tau} = D\nabla^2\xi(\mathbf{R},\tau) - D\nabla(\xi(\mathbf{R},\tau)\mathbf{F}(\mathbf{R})) + (E_R - E_L(\mathbf{R}))\phi(\mathbf{R},\tau) \quad (5.14)$$

where the *quantum–force* $\mathbf{F}$ is now given by:

$$\mathbf{F}(\mathbf{R}) = 2\nabla(\log(\Psi_G(\mathbf{R}))). \quad (5.15)$$

This choice turns the diffusive part into a drift-diffusion process like the Langevin one where transitions to new configurations is regulated by Eq.(5.2), while the branching part now depends on the *local energy*:

$$E_L(\mathbf{R}) = -D\frac{\nabla^2\Psi_G(\mathbf{R})}{\Psi_G(\mathbf{R})} + V(\mathbf{R}), \quad (5.16)$$

which for good choices for $\Psi_G$ has just small fluctuations around its mean value. This last feature is the key aspect for boosting the efficiency of the algorithm since with judicious choices for $\Psi_G(\mathbf{R})$ we may overcome problems like divergences in the interaction potential and we obtain a *zero variance* limit for $\Psi_G(\mathbf{R}) = \Psi_0(\mathbf{R})$ the ground–state. In this case in fact $E_L(\mathbf{R}) = E_0 = E_R$.

The steady-state distribution produced by the process described by Eq.(5.14) is the *mixed distribution*

$$\xi(\mathbf{R},\tau) \xrightarrow{\tau\to\infty} \Phi_0(\mathbf{R})\Psi_G(\mathbf{R}), \quad (5.17)$$

from which we can calculate mixed–expectation values (cf. Eq.(1.27)) by averaging over the random walk. When Importance Sampling is employed we can find the following expression for the short time Green's function

$$G_{IS}(\mathbf{R}',\mathbf{R},\Delta\tau) = K_{IS}(\mathbf{R}',\mathbf{R})B_{IS}(\mathbf{R}). \quad (5.18)$$

where the the drift–diffusion part is analogous to the Langevin case but with a $\Psi_G$–dependent drift–force (5.15) and the potential in the branching part is replaced by the local energy:

$$B_{IS}(\mathbf{R}) = \exp\left(-\Delta\tau\left(E_L(\mathbf{R}) - E_R\right)\right). \quad (5.19)$$

The connection between the classical–system described by the solution of the Fokker–Planck equation and the quantum system described by (5.14) is now more evident: we now know what external force–field $F$ to use and that $B_{IS}$ is the needed reweight factor. We will further elaborate on this in the next section.

A couple of words about the branching process are now necessary. As we have briefly mentioned, the easiest way to account for the branching factor is to allow walkers to accumulate weights during the stochastic process. However, this turns out to be impractical for any finite set of walkers, in fact soon a small

amount of walkers with very large weights will dominate the entire population resulting in a poor overall efficiency. A better alternative is to dynamically adjust the population of walkers by creating identical copies of high–weight ones while deleting low–weight configurations. Identical copies are independently diffused and after some steps will eventually decorrelate giving rise to a correct algorithm. In order to control efficiently the dimension of this walker population that can now fluctuate, one can use the reference energy $E_R$ adjusting it along the random walk in order to coherently increase/decrease the weight of every walker in the current population in order to have a fixed mean population size $N_W$.

This procedure introduces however a systematic bias, whose slowest component scales as $\approx 1/N_W$, and extrapolations in some form to the $N_W \to \infty$ limit are usually needed.

The possibility to tackle this problem, together with the unavailability of *pure–estimators* for the DMC algorithm are two of the main motivations why Reptation Monte Carlo is usually chosen over Diffusion MC.

## 5.2 Path–Integrals in coordinate–space

As we have seen previously the main difference between DMC and RMC is in the representation of the imaginary–time propagator. In the last section we have seen that the random–walk in imaginary–time described by the Schroedinger equation can be successfully mapped into a resampling of the random–process generated by the Fokker–Planck equation (5.4). As we will see in this section however, in Reptation MC there is no direct branching involved.

We start pointing out that the analogy we have developed in the previous section between classical diffusion and quantum evolution implies that imaginary-time correlations can be cast in two different forms:

$$\langle \hat{O}(\tau)\hat{O}(0)\rangle = \int\int d\mathbf{R}' d\mathbf{R} \hat{O}(\mathbf{R}')\mathcal{W}(\mathbf{R}',\mathbf{R},\tau)\Psi_G^2(\mathbf{R})\hat{O}(\mathbf{R}) \tag{5.20}$$

for the classical system and

$$\langle \Psi_G|\hat{O}(\tau)\hat{O}(0)|\Psi_G\rangle = \int\int d\mathbf{R}' d\mathbf{R} \Psi_G(\mathbf{R}')\hat{O}(\mathbf{R}')\mathcal{G}(\mathbf{R}',\mathbf{R},\tau)\hat{O}(\mathbf{R})\Psi_G(\mathbf{R}), \tag{5.21}$$

for the fictious quantum one. In these expressions $\hat{O}$ is some observable, $\mathcal{W}(\mathbf{R}',\mathbf{R},\tau)$ is the Green's function of the Fokker-Planck equation and

$$\mathcal{G}(\mathbf{R}',\mathbf{R},\tau) = \langle \mathbf{R}'|e^{-\tau\hat{\mathcal{H}}}|\mathbf{R}\rangle$$

is the imaginary time propagator of the fictious system with hamiltonian given by (5.8). It is easy to see that $\mathcal{W}(\mathbf{R}',\mathbf{R},\tau)$ equals the so-called importance sampled Green's function $\mathcal{G}$ of the fictious quantum system

$$\mathcal{W}(\mathbf{R}',\mathbf{R},\tau) = \Psi_G(\mathbf{R}')\mathcal{G}(\mathbf{R}',\mathbf{R},\tau)\frac{1}{\Psi_G(\mathbf{R})}, \tag{5.22}$$

which in the short time limit can be well approximated by a Langevin–type transition probability Eq.(5.2).

As we seen in the previous section the random process generated by such transition probability will asymptotically sample from $\Psi_G^2$, while the role of the branching factor $B_{IS}$ is to correct it to the wanted mixed distribution $\Psi_0\Psi_G$. The short time Green's function that we need should be then something like

$$G(\mathbf{R}', \mathbf{R}, \Delta\tau) = \mathcal{W}(\mathbf{R}', \mathbf{R}, \Delta\tau)e^{-\Delta\tau E_L(\mathbf{R})}.$$

We can say this in a more path–integral way by considering the following "partition–function":

$$Z_0 \equiv \langle \Psi_T | e^{-\tau\hat{H}} | \Psi_T \rangle = \int e^{-\mathcal{S}[\mathcal{X}]}\mathcal{P}[\mathcal{X}]D[\mathcal{X}] \tag{5.23}$$

where $\mathcal{P}[\mathcal{X}]$ is the probability distribution for a random walk $\mathcal{X}$, $D[\mathcal{X}]$ is the usual Wiener measure and the action $\mathcal{S}[\mathcal{X}]$ is a functional of the random walk which in the continuum limit coincides with the time integral of the local energy along the path. In order to make the calculation of Eq.(5.23) feasible we break the paths in $M$ time slices (such that $\tau = M\Delta\tau$) obtaining a discrete representation of the path integral, in this case we have

$$\begin{aligned}\mathcal{P}[\mathcal{X}] &= \mathcal{W}(\mathbf{R}_M, \mathbf{R}_{M-1}, \Delta\tau)\cdots\mathcal{W}(\mathbf{R}_1, \mathbf{R}_0, \Delta\tau)\Psi_T^2(\mathbf{R}_0) \\ &= \Psi_T(\mathbf{R}_m)\mathcal{G}(\mathbf{R}_M, \mathbf{R}_{M-1}, \Delta\tau)\cdots\mathcal{G}(\mathbf{R}_1, \mathbf{R}_0, \Delta\tau)\Psi_T(\mathbf{R}_0),\end{aligned} \tag{5.24}$$

and

$$\mathcal{S}[\mathcal{X}] = \epsilon\left[\frac{E_L(\mathbf{R}_0)}{2} + E_L(\mathbf{R}_1) + \cdots + E_L(\mathbf{R}_{M-1}) + \frac{E_L(\mathbf{R}_M)}{2}\right] \tag{5.25}$$

The equation for $Z_0$ can be seen as a generalization of the Feynman-Kac formula and can be easily proved using Trotter-Suzuki breakup to find the relation between the two propagators:

$$G(\mathbf{R}', \mathbf{R}, \Delta\tau) = e^{-\frac{\Delta\tau}{2}E_L(\mathbf{R}')}\mathcal{W}(\mathbf{R}', \mathbf{R}, \Delta\tau)e^{-\frac{\Delta\tau}{2}E_L(\mathbf{R})}. \tag{5.26}$$

$Z_0$ plays then the role of a pseudo partition–function, in the sense that it can be used to calculate observables of the system by differentiation in the same way we use it in classical statistical mechanics.

### 5.2.1 Sampling the paths

Recall that given the path probability for the true quantum system any ground-state expectation value together with correlation functions can be put in the form

$$\langle F[\mathcal{X}] \rangle = \frac{\int P[\mathcal{X}]F[\mathcal{X}]D[\mathcal{X}]}{\int P[\mathcal{X}]D[\mathcal{X}]} \tag{5.27}$$

Now in order to calculate this expectation value using the Metropolis method we need to construct a Markov chain of imaginary-time paths so that the corresponding steady state distribution is

$$P[\mathcal{X}] = \mathcal{W}(\mathbf{R}_M, \mathbf{R}_{M-1}, \Delta\tau)\cdots\mathcal{W}(\mathbf{R}_1, \mathbf{R}_0, \Delta\tau)\Psi_T^2(\mathbf{R}_0)e^{-\mathcal{S}[\mathcal{X}]} \tag{5.28}$$

Our dynamical variables are quantum paths or *snakes* $\{\mathbf{R}_0, \mathbf{R}_1, \ldots, \mathbf{R}_M\}$ living in $\mathbb{R}^{3N(M+1)}$ where each $\mathbf{R}_k \in \mathbb{R}^{3N}$ is a single configuration of our many-body system.

Let $\mathcal{X}$ be the current state of the Markov chain and $\bar{\mathcal{X}} = \{\mathbf{R}_M, \mathbf{R}_{M-1}, \ldots, \mathbf{R}_0\}$ the reversed snake. We will need this configuration in order to fulfill time-reversal invariance of the walk. Now the algorithm proposed in [170] proceeds as follows: with probability 1/2 a new snake $\mathcal{Y} = \{\mathbf{Q}_0, \mathbf{Q}_1, \ldots, \mathbf{Q}_M\}$ is generated from $\mathcal{X}$ with proposal density $T_0(\mathcal{Y}, \mathcal{X})$ otherwise $\mathcal{Y}$ is generated from $\bar{\mathcal{X}}$ with proposal density $T_0(\mathcal{Y}, \bar{\mathcal{X}})$. In the general case $T_0$ can be chosen in order to update an arbitrary number $r$ of configurations from the starting snake.

Let us consider the following form:

$$T_0[\mathcal{Y} \leftarrow \mathcal{X}] = \mathcal{W}_\epsilon(\mathbf{Q}_M, \mathbf{Q}_{M-1}) \cdots \mathcal{W}_\epsilon(\mathbf{Q}_{M-r+1}, \mathbf{Q}_{M-r}) \tag{5.29}$$

whenever $\mathbf{Q}_0 = \mathbf{R}_r, \ldots, \mathbf{Q}_{M-r} = \mathbf{R}_M$ and zero otherwise. The new snake is then accepted or rejected according to the MRT test Eq.(1.5) using (5.28) as target distribution. The extension for $\bar{\mathcal{X}}$ is straightforward. If we further assume micro-reversibility of the random walk, that is:

$$\mathcal{W}_\epsilon(\mathbf{R}_i, \mathbf{R}_j)\Psi_T^2(\mathbf{R}_j) = \mathcal{W}_\epsilon(\mathbf{R}_j, \mathbf{R}_i)\Psi_T^2(\mathbf{R}_i), \tag{5.30}$$

we can put the acceptance probability in a neater form

$$A[\mathcal{Y} \leftarrow \mathcal{X}] = \min\left(1, \frac{e^{-\mathcal{S}[\mathcal{Y}]}}{e^{-\mathcal{S}[\mathcal{X}]}}\right), \tag{5.31}$$

and the same for $\bar{\mathcal{X}}$. In fact using micro-reversibility we can freely revert the order of the propagators $\mathcal{W}$ in Eq.(5.28) so that they cancel each other.

We can now note the way the branching term is handled in RQMC: it is incorporated in the acceptance probability of the Metropolis random walk, instead of using it as a weight in a branching random walk as it is done in DMC.

This is the first version of the RQMC initially devised by Baroni e Moroni, however some technical arrangements can be done to improve the algorithm efficiency. Before entering into these details we first resume how to calculate pure observables as well as correlation functions within this formalism.

### 5.2.2 Calculation of observables

Ground state expectation values of any observable can be put in the following form

$$\begin{aligned} \langle \hat{O} \rangle_\tau &= \frac{\int P[\mathcal{X}] \hat{O}[\mathcal{X}] D[\mathcal{X}]}{\int P[\mathcal{X}] D[\mathcal{X}]} \\ &= \frac{\langle \Psi_T e^{-\tau \hat{H}} | \hat{O} | e^{-\tau \hat{H}} \Psi_T \rangle}{\langle \Psi_T | e^{-2\tau \hat{H}} | \Psi_T \rangle} \end{aligned} \tag{5.32}$$

where we have considered a quantum path $\mathcal{X}$ over an imaginary-time interval $2\tau$ discretized in $2M+1$ time slices. Pure observables can then be obtained using a

sufficiently large projection time $\tau$. The explicit form for the expectation value will then be

$$\langle \hat{O} \rangle_\tau = \frac{\int \Psi_T(\mathbf{R}_{2M+1}) \prod_{j=0}^{2M+1} G(\mathbf{R}_{j+1}, \mathbf{R}_j, \Delta\tau) \Psi_T(\mathbf{R}_0) O(\mathbf{R}_{M+1}) \left( \prod_{j=0}^{2M+1} d\mathbf{R}_j \right)}{\int \Psi_T(\mathbf{R}_{2M+1}) \prod_{j=0}^{2M+1} G(\mathbf{R}_{j+1}, \mathbf{R}_j, \Delta\tau) \Psi_T(\mathbf{R}_0) \left( \prod_{j=0}^{2M+1} d\mathbf{R}_j \right)}. \tag{5.33}$$

We see that the value of the observable is taken at the central configuration of the snake. This is the point where reliable pure expectation values can be calculated as we have seen in Section 1.2.2.

One can of course calculate even the *mixed* expectation value as in DMC, this may be useful for observables that commute with the Hamiltonian of the system. In these cases we have

$$\begin{aligned} \ll \hat{O}_H \gg_\tau &= \frac{\langle \Psi_T e^{-\tau \hat{H}} | \hat{O} | e^{-\tau \hat{H}} \Psi_T \rangle}{\langle \Psi_T | e^{-2\tau \hat{H}} | \Psi_T \rangle} = \frac{\langle \Psi_0 | \hat{O} | \Psi_0 \rangle}{\langle \Psi_0 | \Psi_0 \rangle} \\ &= \frac{\langle \Psi_T e^{-2\tau \hat{H}} | \hat{O}_H | \Psi_T \rangle}{\langle \Psi_T | e^{-2\tau \hat{H}} | \Psi_T \rangle} = \frac{\langle \Psi_0 | \hat{O} | \Psi_T \rangle}{\langle \Psi_0 | \Psi_T \rangle} \\ &= \frac{\langle \Psi_T | \hat{O}_H | e^{-2\tau \hat{H}} \Psi_T \rangle}{\langle \Psi_T | e^{-2\tau \hat{H}} | \Psi_T \rangle} = \frac{\langle \Psi_T | \hat{O} | \Psi_0 \rangle}{\langle \Psi_T | \Psi_0 \rangle}. \end{aligned} \tag{5.34}$$

In practice the accumulated value for calculating (5.34) is the mean of the value of $O$ at both the head and tail configurations of the snake:

$$\hat{O}[\mathcal{X}] = 0.5 \left( O(\mathbf{R}_0) + O(\mathbf{R}_{2m+1}) \right).$$

This is the procedure we used for the calculation of the ground–state energy.

The calculation of imaginary-time correlation functions of two generic observables $\hat{A}$ and $\hat{B}$ is similar

$$C_{AB}(\beta) \equiv \langle \hat{A}(0) \hat{B}(\beta) \rangle_\tau = \frac{\langle \Psi_T e^{-\tau \hat{H}} | \hat{A} e^{-\beta \hat{H}} \hat{B} | e^{-\tau \hat{H}} \Psi_T \rangle}{\langle \Psi_T | e^{-(2\tau+\beta) \hat{H}} | \Psi_T \rangle} \tag{5.35}$$

where time dependence of operators is intended in imaginary-time Heisenberg picture. In path integral language this translates directly into

$$\langle \hat{O} \rangle_\tau = \frac{\int \Psi_T(\mathbf{R}_{2M+K+1}) \prod_{j=0}^{2M+K+1} G(\mathbf{R}_{j+1}, \mathbf{R}_j, \Delta\tau) \Psi_T(\mathbf{R}_0) A(\mathbf{R}_{M+1}) B(\mathbf{R}_{M+K+1}) \left( \prod_{j=0}^{2M+K+1} d\mathbf{R}_j \right)}{\int \Psi_T(\mathbf{R}_{2M+K+1}) \prod_{j=0}^{2M+K+1} G(\mathbf{R}_{j+1}, \mathbf{R}_j, \Delta\tau) \Psi_T(\mathbf{R}_0) \left( \prod_{j=0}^{2M+K+1} d\mathbf{R}_j \right)} \tag{5.36}$$

where now the path is composed of $2M+K+1$ time slices over a total imaginary time of $2\tau + \beta$. For the purpose of a simple implementation the actual total imaginary time interval of the path is kept fixed to a certain value $\Gamma$. Then, correlation functions at all values of $\beta$ are calculated considering the innermost piece of path long $\beta$ as the central part of the total snake. Thus considering the two remaining $\tau = (\Gamma - \beta)/2$ long parts as *projection paths*.

Clearly, these paths can not be too short in order to project out the correct ground state function so one has to fix a $\beta$ limit for the computed correlation function values. In the present work values $\tau_{min} \approx 0.1$–$0.2 H^{-1}$ have been chosen, corresponding to roughly $100 - 200$ time slices.

## 5.3 Algorithmic refinements

As it is, the RQMC algorithm can behave quite badly because of the growth of the time-discretization error along the path. This fact can be particularly tedious in the central part of the path where measurements are taken. To address this problem Yuen et al. ([171]) proposed to neglect the requirement of micro-reversibility and sample from the following density:

$$\tilde{P}[\mathcal{X}] = \mathcal{W}(\mathbf{R}_M, \mathbf{R}_{M-1}, \Delta\tau)\cdots\mathcal{W}(\mathbf{R}_{\frac{M}{2}+1}, \mathbf{R}_{\frac{M}{2}}, \Delta\tau)\Psi_T^2(\mathbf{R}_{\frac{M}{2}}) \\ \mathcal{W}(\mathbf{R}_{\frac{M}{2}-1}, \mathbf{R}_{\frac{M}{2}}, \Delta\tau)\cdots\mathcal{W}(\mathbf{R}_0, \mathbf{R}_1, \Delta\tau)e^{-\mathcal{S}[\mathcal{X}]} \quad (5.37)$$

which is clearly identical to Eq.(5.28) when micro-reversibility is assumed. However, if the time step error is substantial this form of $\tilde{P}$ will guarantee that the density at the center of the snake is proportional to the desired density, namely the Langevin random-walk multiplied by the exponential of the action.

In cases where the guiding wave–function is not a good approximation to the ground–state the use of this scheme may however allow a large number of "bad" configurations to be accepted, with the net effect that both the head and the tail of the snake will fail to reach equilibration. In order to cure this behavior we may adopt another scheme proposed later by the same authors ([172]), the so called *head-tail adjusted* Reptation Monte Carlo. The idea here is to put the square of the trial wave-function at the bead of the snake where we start to generate the next step. The target distribution is the same as Eq.(5.28) for a *head* move and equal to

$$P[\mathcal{X}] = \Psi_T^2(\mathbf{R_M})\mathcal{W}(\mathbf{R_M}, \mathbf{R_{M-1}}, \Delta\tau)\cdots\mathcal{W}(\mathbf{R_1}, \mathbf{R_0}, \Delta\tau)e^{-\mathcal{S}[\mathcal{X}]} \quad (5.38)$$

for a *tail* move. It is fundamental to note that now all of the propagators $\mathcal{W}$ can no longer be canceled. We easily obtain then the following acceptance probability for a *tail* move:

$$A[\mathcal{Y} \leftarrow \mathcal{X}] = \min\left(1, \frac{\Psi_T^2(\mathbf{R}_M)\mathcal{W}(\mathbf{R}_M, \mathbf{R}_{M-1}, \Delta\tau)\cdots\mathcal{W}(\mathbf{R}_{M-r+1}, \mathbf{R}_{M-r}, \Delta\tau)e^{-\mathcal{S}[\mathcal{Y}]}}{\Psi_T^2(\mathbf{R}_{M-r})\mathcal{W}(\mathbf{R}_{M-r}, \mathbf{R}_{M-r+1}, \Delta\tau)\cdots\mathcal{W}(\mathbf{R}_{M-1}, \mathbf{R}_M, \Delta\tau)e^{-\mathcal{S}[\mathcal{X}]}}\right), \quad (5.39)$$

while for the *head* one we have:

$$A[\mathcal{Y} \leftarrow \mathcal{X}] = \min\left(1, \frac{\Psi_T^2(\mathbf{R}_0)\mathcal{W}(\mathbf{R}_0, \mathbf{R}_1, \Delta\tau)\cdots\mathcal{W}(\mathbf{R}_{r-1}, \mathbf{R}_r, \Delta\tau)e^{-\mathcal{S}[\mathcal{Y}]}}{\Psi_T^2(\mathbf{R}_r)\mathcal{W}(\mathbf{R}_r, \mathbf{R}_{r-1}, \Delta\tau)\cdots\mathcal{W}(\mathbf{R}_1, \mathbf{R}_0, \Delta\tau)e^{-\mathcal{S}[\mathcal{X}]}}\right). \quad (5.40)$$

As suggested in [170] the number $r$ of configurations generated at each step can be chosen randomly to prevent the walk get stuck in some region of the extended configuration space, the maximum value should be chosen in order to obtain a quite high acceptance ratio $\approx 0.8$.

Reptation moves presented here have however some drawback: the autocorrelation time of the random walk (the number of steps necessary to obtain two uncorrelated snakes) can be quite high being a quadratic function of the snake length $L$. In particular, when dealing with long snakes (some hundreds of configurations) and many particles, an accurate guiding function is really needed, because otherwise the computational cost to generate a new uncorrelated sample in the space of snakes becomes prohibitive.

An alternative update scheme that may reduce the autocorrelation time is the so-called *bounce method* of Pierleoni and Ceperley [173]. The idea is to keep going in the same direction (ie head or tail) until a move is rejected, in which case we move from the other side of the snake. Although this algorithm does not fulfill the detailed-balance condition, it can be proved (see [173]) to sample from the correct steady-state distribution $P[\mathcal{X}]$. The main advantage of this procedure is the possible reduction in autocorrelation time which is now $L^2/(an)$, with $a$ the acceptance ratio and $n$ the average number of steps taken along the same direction before the bounce occurred.

# Chapter 6

# Density Response of Superfluid $He^4$

Condensed phases of helium provide an exceptional example of a strongly correlated system where quantum effects play a crucial role. Both helium isotopes, the Boson $He^4$ and the Fermion $He^3$, undergo a thermodynamic transition at a critical temperature $T_c$ of $2.19K$ for liquid $He^4$ and $2.49mK$ for liquid $He^3$. Below this temperature these systems become superfluid, exhibiting many strange properties. For example, the viscosity of the liquid drops to zero and heat transport from diffusive becomes wave-like (*second sound*).

The reasons of this transition are different in the two cases: the properties of superfluid $He^4$ can be described by means of Bose Einstein Condensation of the atoms, whereas in $He^3$ the process responsible for the appearance of superfluidity is the formation of Cooper-pairs of atoms and is thus more similar to BCS superconductivity. In this work we have studied the boson case.

## 6.1 Excitations in superfluid helium

At a macroscopic level, many of the thermodynamical properties of superfluid $He^4$ can be described within the Tisza's phenomenological two-fluid model [176]. In this view the liquid is thought of as a mixture of a $superfluid$ and a *normal* components. At zero temperature the whole liquid is supposed to be in the $superfluid$ state. As we raise the temperature the *normal* component grows until it eventually constitutes the whole liquid at the critical temperature $T_c$

Nearly seventy years ago, Landau [177] realized that the macroscopic properties of the liquid would precisely resemble those of a mixture of two fluids, provided that a certain form is assumed for the energy-momentum relation $\omega(k)$ satisfied by the elementary excitations in the liquid. In particular, it was shown that a collective excitation with a deep minimum in $\omega(k)$ should exist. This led him to postulate the existence of the *roton* as another type of excitation, which in his view had to be connected to some kind of vortical motion in the fluid, with a minimum energy $\Delta$ needed to excite it. For this reason below $\approx 0.5K$ there are practically only phonons while rotons can be excited when more energy is

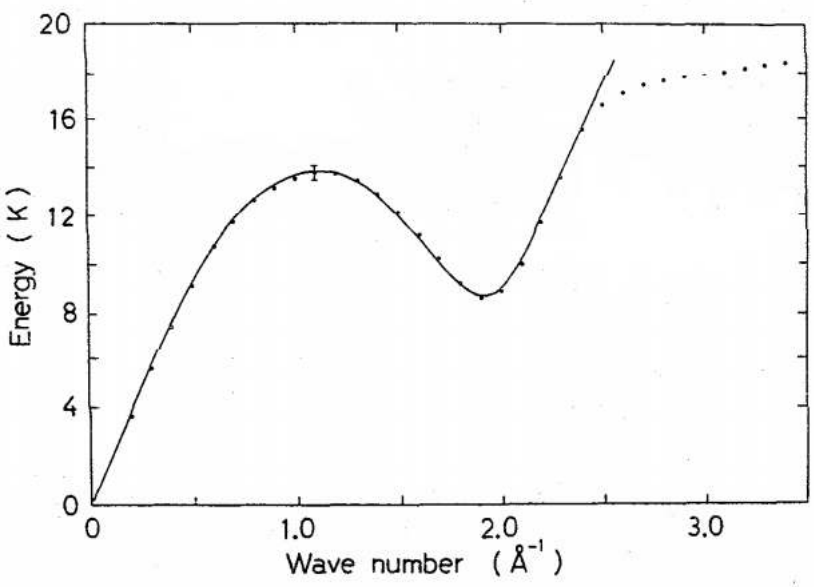


Figure 6.1: Experimentally determined excitation spectrum at 1.1 K, SVP. Dots are neutron scattering data [174] and the solid line is a polynomial fit (picture taken from [175])

available, and became dominant above $\approx 1.0K$. This argument is in agreement with the experimental evidence that below $0.5K$ the specific heat varies as $T^3$ in just the manner to be expected if only compressional waves could be excited.

In this picture the two fluid model is now interpreted as the presence of a macroscopic wave-function extending over the whole system and of a weakly interacting gas of elementary excitations (phonons and rotons). At zero temperature all the atoms are described by this macroscopic wave-function and the liquid is in the superfluid state. As the temperature is raised the number of thermally excited phonons and rotons increases and they act as a *normal* fluid component. When the temperature reaches $T_c$ the number of thermally excited elementary excitations equals the number of atoms in the system, and the entire liquid becomes a normal fluid.

In the following we will briefly summarize the experimental dispersion curve obtained from inelastic neutron scattering data [175]. The energy momentum dispersion relation (Fig. 6.1) has exactly the form suggested by Landau and can be divided into basically four regions.

The first one is the *phonon branch* and corresponds to small momenta, where the energy spectrum approaches linearity:

$$\omega_{ph}(Q) = \lim_{Q\to 0} \omega(Q) = c_1 Q. \tag{6.1}$$

Here $c_1 = 238ms^{-1}$ is the (first) sound velocity.

The elementary excitations which have energies near the first energy maximum ($Q_m = 1.125A^{-1}$ and $E_m = 13.85K$) have come to be called *maxons*. In the past, less attention has been devoted to this part of the spectrum since the

maxon energies are relatively high, and their contribution to thermal properties is correspondingly very small.

The third region is the *roton minimum* which can be very well represented by Landau's parabolic expression

$$\omega_{rot}(Q) = \Delta + \frac{1}{2\mu}(Q - Q_r)^2, \tag{6.2}$$

where $\Delta$ is the roton energy gap, $Q_r$ is the roton momentum at the minimum and $\mu$ is the effective mass of the excitation near $Q_0$. These three quantities describing the roton minimum are called the *Landau parameters* of the roton spectrum, and have the values $\Delta = 8.61K$, $Q_r = 1.925A^{-1}$ and $\mu = 0.15m$.

Beyond the roton minimum, the slope of the spectrum approaches the velocity of sound $c_1$ at a momentum $Q_s \approx 2.15A^{-1}$ and then bends over and approaches twice the roton energy at $Q_e \approx 2.6A^{-1}$, finally terminating at a momentum $Q_e \approx 3.6A^{-1}$. Above this threshold the weight of the single phonon/roton mode vanishes and a description by means of weakly interacting elementary excitations cannot be made. This behavior for large momenta was predicted by Pitaevskii to be:

$$\omega_P(Q) = 2\Delta - \alpha \exp\left(-\frac{\sigma}{Q_e - Q}\right) \tag{6.3}$$

where $\alpha$ and $\sigma$ are constants to be determined. The physical explanation is that at these momentum transfers the decay of a single roton into a pair of rotons becomes allowed, or in other words the continuum part of the spectrum merges with the single-excitation peak.

Once fitted to experimental data this model can be used to predict many thermodynamical properties with high accuracy [175]. However, a more fundamental approach starting from first-principles would be welcome.

Along this direction an attempt of devising a microscopic treatment of superfluid $He^4$ was carried out by Feynman [178], who gave an analytical upper bound for the energy-momentum dispersion curve obtained using variational calculations

$$\omega(Q) = \frac{\hbar^2 Q^2}{2mS(Q)}, \tag{6.4}$$

where $S(Q)$ is the static structure factor (6.5) of the liquid:

$$\begin{aligned} S(Q) &= \frac{1}{N}\left\langle \left| \sum_{j=1}^{N} e^{i\mathbf{Q}\cdot\mathbf{r}_j} \right|^2 \right\rangle = \frac{1}{N}\langle |\rho_{\mathbf{Q}}|^2 \rangle \\ &= \frac{1}{N}\sum_{j=1}^{N}\sum_{k=1}^{N}\left\langle e^{i\mathbf{Q}\cdot(\mathbf{r}_j - \mathbf{r}_k)} \right\rangle = \frac{1}{N}\langle \rho^{\dagger}_{\mathbf{Q}}\rho_{\mathbf{Q}} \rangle \end{aligned} \tag{6.5}$$

where averages are taken on the ground–state and $\rho_{\mathbf{Q}}$ is the Fourier transform of the density operator

$$\rho_{\mathbf{Q}} = \int_{-\infty}^{+\infty} d\mathbf{r} e^{-i\mathbf{Q}\cdot\mathbf{r}} \rho(\mathbf{r}). \tag{6.6}$$

It can be proved that this form leads to the correct linear behavior in the long wave-length limit (phonons). The static structure factor has in fact a sharp

maximum at $k \approx 2A^{-1}$ which is the wavelength equal to the nearest neighbor distance in the liquid, gives the corresponding roton minimum. Despite the appearance of the minimum is in qualitative agreement with Landau's prediction, the gap $\Delta$ predicted in this way (using experimentally obtained $S(Q)$) is too high ($\approx 2\Delta$). An improvement in accuracy has been later achieved by Feynman and Cohen [179] considering also backflow contributions.

As pointed out by Ceperly [180] the variational approach leaves a number of questions unanswered. First, it is guaranteed to find a single excitation energy not the entire spectrum, nor the lifetime of the excitation. Second, extending the method to non-zero temperature brings in more approximations needed in order to account for interactions between excitations.

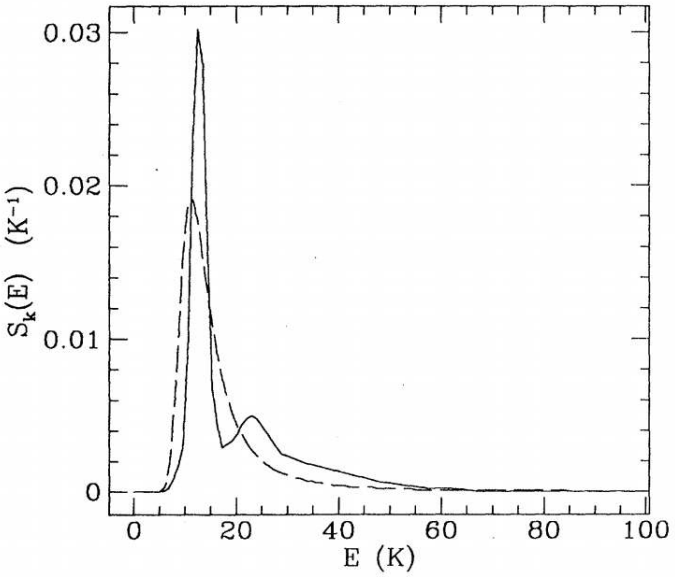


Figure 6.2: Dynamic structure factor for liquid He$^4$ at 1.2 K and wavelength $Q = 0.76A^{-1}$. Solid line as measured by neutron scattering [36]; dashed curve MEM reconstruction from the PIMC data [37]

PIMC calculations can in principle overcome the last problem and they have been studied by Boninsegni and Ceperley in [181] and [37]. However due to the problems connected to the direct inversion of the thermal intermediate scattering function $F(Q,\tau)$:

$$F(Q,\tau) = \frac{1}{NZ} Tr\left[\rho_Q^\dagger e^{-\tau\hat{H}} \rho_Q e^{-(\beta-\tau)\hat{H}}\right], \tag{6.7}$$

the agreement with experiment is not particularly good. As we can see from the picture Fig.6.2, although this approach gives the overall shape of the response function, it does not resolve the two-peak structure nor the width of the phonon-roton line. Taking the peak position as an estimate of the excitation energy one gets a dispersion curve with an agreement with experiment of about 10%. These problems are clearly linked to the ill-posed nature of the Laplace-transform inversion.

## 6.2 Monte Carlo Calculation

At relatively low densities, a realistic description of a system of bulk liquid $He^4$ can be obtained considering an hamiltonian with pair–wise interactions only:

$$\hat{H} = -\frac{\hbar^2}{2m}\sum_{i=1}^{N}\nabla_i^2 + \sum_{i<j=1}^{N} v(r_{ij}) \tag{6.8}$$

where sums rise over the $N$ atoms of the system, $m$ is the helium mass and $v(r)$ is the pair potential. In all the calculations presented here we used the $HFDHE2$ two-body interaction of Aziz et al. [182] given by the following central potential:

$$v(r) = \epsilon\left[Ae^{\left(-\alpha\frac{r}{r_m}\right)} - F(r)\left(C_6\left(\frac{r}{r_m}\right)^6 + C_8\left(\frac{r}{r_m}\right)^8 + C_{10}\left(\frac{r}{r_m}\right)^{10}\right)\right] \tag{6.9}$$

where we have introduced the function

$$F(r) = \begin{cases} 1 & \text{if} r \geq Dr_m \\ \exp-(Dr_m/r) & \text{if} r < Dr_m. \end{cases} \tag{6.10}$$

The parameters in Eqs.(6.9) and (6.10) are taken from Kalos et al. [183].

Recently it has been pointed out (see e.g. [184]) that three-body forces may be needed to correctly describe the system in the condensed phases. Although we didn't consider the possibility of three–body forces in this work it would be interesting to see their effect on excited–state properties from the calculated response functions.

### 6.2.1 Trial Wave Function

One of the key aspect needed to obtain an efficient RMC calculation is the availability of good trial–wave functions to be used in the Importance Sampling procedure. In our case we have considered a Jastrow wave–function with explicit two and three–body correlations:

$$\Psi(\vec{r}_1,\cdots,\vec{r}_N) = \exp\left(\sum_{i<j}^{N} U_2(r_{ij}) + \sum_{i<j<k}^{N} U_3(\vec{r}_i,\vec{r}_j,\vec{r}_k)\right) \tag{6.11}$$

where $r_{ij} = |\vec{r}_i - \vec{r}_j|$ are the pair–wise distances while $U_2$ and $U_3$ are pair and triplet pseudo–potentials respectively. In order to efficiently optimize these correlators, the pseudo–potentials are expanded in a suitable basis set ([185]):

$$U_2(r) = U_2^0(r) + \sum_{m}^{M}\alpha_m\chi_m(r), \tag{6.12}$$

$$U_3(\vec{r}_i,\vec{r}_j,\vec{r}_k) = U_3^0(\vec{r}_i,\vec{r}_j,\vec{r}_k) + \sum_{mnl}\sum_{\text{cyc}}\beta_{mn}^l\chi_m(r_{ij})\chi_n(r_{ik})P_l(\hat{r}_{ij}\dot{\hat{r}}_{ik}). \tag{6.13}$$

The matrices $\beta_{mn}^l$ must be symmetric in $m,n$ and with $cyc$ we mean a sum over the permutations of $ijk$.

The zeroth–order contributions are given respectively by the McMillan ansatz:

$$U_2^0(r_{ij}) = -\frac{1}{2}\left(\frac{a}{r_{ij}}\right)^5 \tag{6.14}$$

with $a = 3.04\mathring{A}$, and Feynman pseudopotentials:

$$U_3^0(r_{ij}) = -\frac{1}{2}\sum_{\text{cyc}} \xi^0(r_{ij})\xi^0(r_{ik})P_1(\hat{r}_{ij}\dot{\hat{r}}_{ik}). \tag{6.15}$$

For the latter we used a gaussian form for $\xi^0$:

$$\xi^0(r) = a_t e^{-\left(\frac{r-r_t}{\sigma_t}\right)}\xi^0(r_{ik})P_1(\hat{r}_{ij}\dot{\hat{r}}_{ik}). \tag{6.16}$$

with $a_t = 0.827\mathring{A}^{-1}$, $r_t = 2.04\mathring{A}$ and $\sigma_t = 1.05\mathring{A}$.

In order to limit the dimensionality of the parameter space we adopted the simplifying assumptions $l = 0, 1$ in Eq.(6.13) and also $\beta^l_{mn} \equiv \beta^l_m\beta^l_n$ which restricts the possible triplet correlations to the factorized form:

$$U_3^F(\vec{r}_i, \vec{r}_j, \vec{r}_k) = \sum_l \sum_{\text{cyc}} \xi_l(r_{ij})\xi_l(r_{ik})P_l(\hat{r}_{ij}\dot{\hat{r}}_{ik}), \tag{6.17}$$

with

$$\xi_l(r) = \sum_m^{M_t} \beta^l_m \chi_m(r). \tag{6.18}$$

Finally the basis function are taken to be of the form:

$$\chi_m(r) = \begin{cases} \left[1 - \cos\frac{2\pi m}{L-2r_c}(r - L/2)r\right] r^n & \text{if } r \geq r_c \\ r^n & \text{if } r < r_c \end{cases} \tag{6.19}$$

where $L$ is the simulation box side and $r_c$ is a cut-off distance introduced to enhance the stability during the optimization. The exponent $n$ is taken to be $-5$ for the expansion of $U_2$ while $n = l$ in the $l$–th component of $U_3$.

The optimization of the parameters $\alpha_m$ and $\beta^l_m$ has been performed using a Variational Monte Carlo and the SRH algorithm by Sorella [44]. We have found that a value of $M \approx M_t \approx 20$ is sufficient to get converged results within VMC. Finally we note that the inclusion of the triplet correlations brings a noticeable lowering in the ground–state energy at equilibrium density from $\approx -6.2K$ to $\approx -6.9K$, much closer to the experimental value of $-7.17K$. This big improvement will be crucial to efficiently calculate ground–state properties with RMC.

Reptation Quantum Monte Carlo has been carried out using the Metropolis acceptance probabilities Eq.(5.39) and Eq.(5.40) with the bounce algorithm. In order to simulate the bulk liquid at the experimental equilibrium density $\rho_0 = 0.02186\mathring{A}^{-3}$, the computation is carried out using either 64 or 125 helium atoms in a cubic box of size $L$ with Periodic Boundary Conditions (PBC). To enforce PBC, the pair–potential $v(r)$ was smoothly cut–off at $r = L/2$ by using:

$$\begin{aligned} v'(r) &= \begin{cases} v(r) + v(L-r) - 2v(L/2) & \text{if } r \leq L/2 \\ 0 & \text{if } r > L/2 \end{cases} \\ &= v(r) - \delta v(r), \end{aligned} \tag{6.20}$$

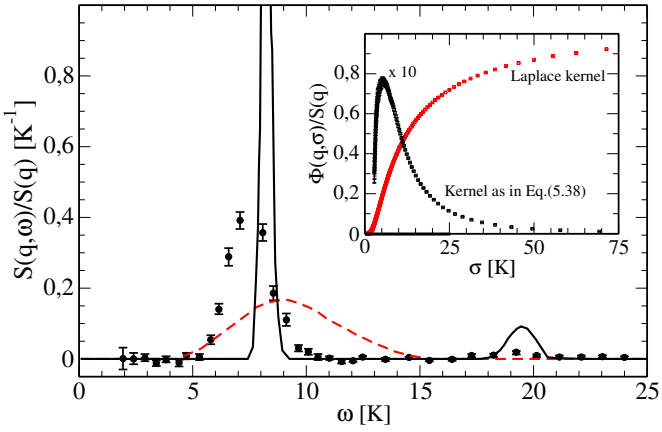


Figure 6.3: S$(q,\omega)$ in liquid $^4$He at T=0 and $q$ = 0.44Å$^{-1}$. Black solid curve: inversion of IT with kernel in Eq. (4.37). Red dashed curve: inversion of IT with Laplace kernel. Experimental data (black dots) are from Ref. [186] (at $T$ = 1.34K and $q$ = 0.4Å$^{-1}$). In the inset the corresponding ITs are shown.

and correspondingly a correction

$$\Delta V = \frac{1}{2}\rho \int \delta v(r) g(r) dr \tag{6.21}$$

has been added to the computed potential energy. The *pair distribution function* $g(r)$ is obtained from the simulation for $r \leq L/2$ and assumed to be $\approx 1$ for $x > L/2$. The same procedure has been applied to the functions $U_2$ and $U_3$. Typical time-steps are $0.001 \div 0.0001K^{-1}$ with snakes length ranging usually between 400 and 800 time-slices. Thanks to the imaginary–time projection, ground state properties are well reproduced: the ground–state energy per particle si $E_0^{RMC} = -7.23 \pm 0.01K$, in good agreement with previous calculations with the same potential [170], and with the experimental value $E_0^{exp} = -7.17K$. We also checked that the static structure actor $S(q)$ is consistent with both experimental data and previous calculations [170, 185].

## 6.3 Results

Turning to the result on $S(\mathbf{q},\omega)$, the striking difference between the estimate obtained inverting the transform with the Laplace kernel or the one in Eq. (4.37) can be seen in Fig. 6.4, where we compare the results of the inversion obtained from RMC data with both kernels (in the figure $S(q,\omega)$ has been normalized to the static structure factor $S(q)$). Apart from the small shift of the peak due to the 0.04 Å$^{-1}$ difference in the momentum transfer[1], the new kernel permits to retrieve the information on the second peak and gives a much more realistic

[1] the momenta are limited by the discretization imposed by the use of a finite simulation cell, here L=14.306Å

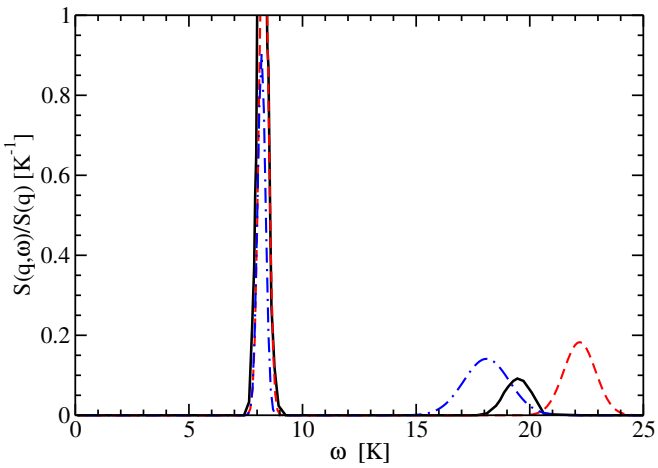


Figure 6.4: S$(q,\omega)$ in liquid $^4$He at T=0 and $q$ = 0.44Å$^{-1}$. Inversion with SMART or EMML (solid black line), inversion with ansatz in Eq. (6.22) and $M$ = 2 (dashed red line) and $M$ = 3 (dash-dotted blue line).

height and width of the one-phonon peak. It should be noted that at $T$ = 0 the peak corresponding to the collective excitation should be substantially narrower than the measured one at higher T. An estimate of the intrinsic peak width is $\Delta\omega \simeq 5 \times 10^{-4}$K [187]. Therefore, the experimental width is essentially due to the resolution of the apparatus [186].

The power of the new kernel appears to be clear from the insert in Fig. 6.3, where the two transforms obtained with the Laplace kernel ($K(\sigma,\omega) = e^{-\omega/\sigma}$) and with the kernel in (4.37) are shown. In the former case no structure is visible, while a clear signature of a resonance is visible in the latter case in the interesting region. This is due to the fact that the new kernel is a representation of the delta-function. Even if we have used $P$ = 2 and therefore its width is rather large around the first resonance energy (see Fig. 4.3) the inversion procedure is able to recover a narrow peak. In addition a second peak is recovered, even if the width of the kernel is larger in that region.

Above we stated that our main point is on the improvement that one can attain from a wise choice of the integral transform to invert, and not on the particular inversion scheme used. Nonetheless a few comments are necessary here concerning the methods used to invert the transform. We have used three different methods: the Entropy Maximization Maximum Likelihood (EMML) [188], the Simultaneous Algebraic Reconstruction Technique (SMART) [188] (both with the unique constraint of a positive definite DSF) and a simpler *regularization* method. The latter consists in writing

$$S(\mathbf{q},\omega) = \sum_m^M c_m \frac{1}{\sqrt{2\pi}\Gamma_m} e^{-\left(\frac{\omega-\omega_m}{\sqrt{2}\Gamma_m}\right)^2}, \tag{6.22}$$

evaluating its IT and performing a (non linear) best fit of the parameters $c_m, \omega_m$ and $\Gamma_m$ on $\Phi(\sigma)$ calculated by RMC for a large a large number of $\sigma$ values (300 points). In Fig. 6.4 the results obtained with the different inversions are

shown. One notices that the first narrow peak is rather stable against the three methods. A second peak is also predicted in all cases. Its position and width is very stable against the inversion with EMML or SMART. As expected, the fit with the ansatz in (6.22) is too rough to be reliable in a region where the kernel has too large a width, as shown in Fig. 4.3.

In Fig. 6.5a we have plotted the dispersions of the collective modes obtained using the new transform. The bars in the figures indicate the computed widths of the excitations. Both the peak positions and the line widths are robust with respect to EMML or SMART inversions. We found that for $q \leq 2.4$ Å$^{-1}$ methods converge to the same solutions.

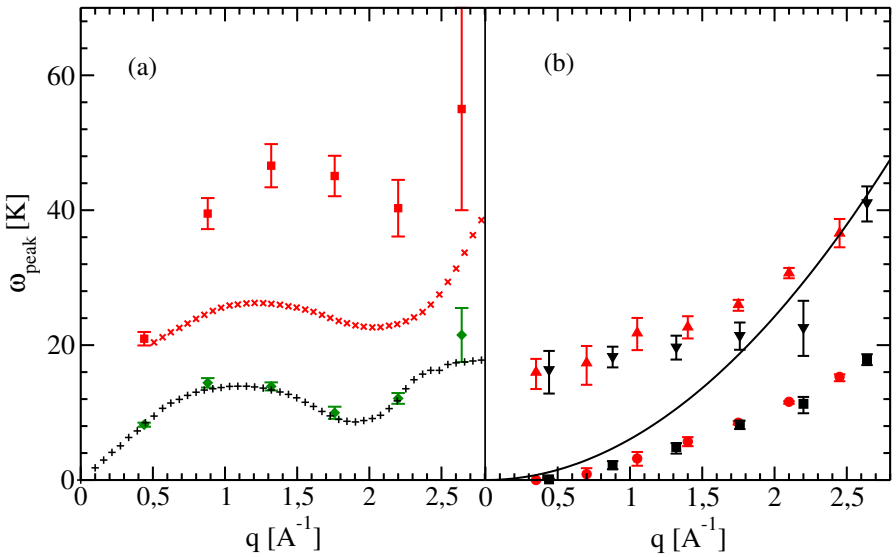


Figure 6.5: (a): Dispersion of the collective modes in liquid $^4$He at equilibrium density and $T = 0$. Computed values for the first (green diamonds) and second (red squares) peaks. Error bars are estimates of the widths of the peaks. + and × are the corresponding experimental data from Ref. [189] at $T = 1.1$ K. (b): Dispersion of the $1^{st}$ peak (red circles: box with N=64; black squares: box with N=125) and $2^{nd}$ peak (red up triangles: box with N=64; black down triangles: box with N=125) of the *incoherent* DSF. Full line: free-particle excitation spectrum. (Inset) half-widths of the 1st peak for both incoherent excitations (black circles: box with N=64; red squares: box with N=125) and coherent ones (green diamonds: box with N=64)

The experimental low-lying part [186] is extremely well reproduced up to $q \approx 2.6$ Å$^{-1}$. The two-phonon branch is clearly visible and well resolved. As it happens in Ref. [34], it only qualitatively compares to the experiment. The calculated widths of the second-branch excitations are much smaller than what is obtained from experiments. At present it is difficult to judge the reason of this discrepancy. It can be ascribed to temperature effects, inadequacy of the Aziz pair-potential to describe multi-excitation processes or it might be as well an indication that the width of our kernel is not small enough in that energy region to allow a more robust estimation.

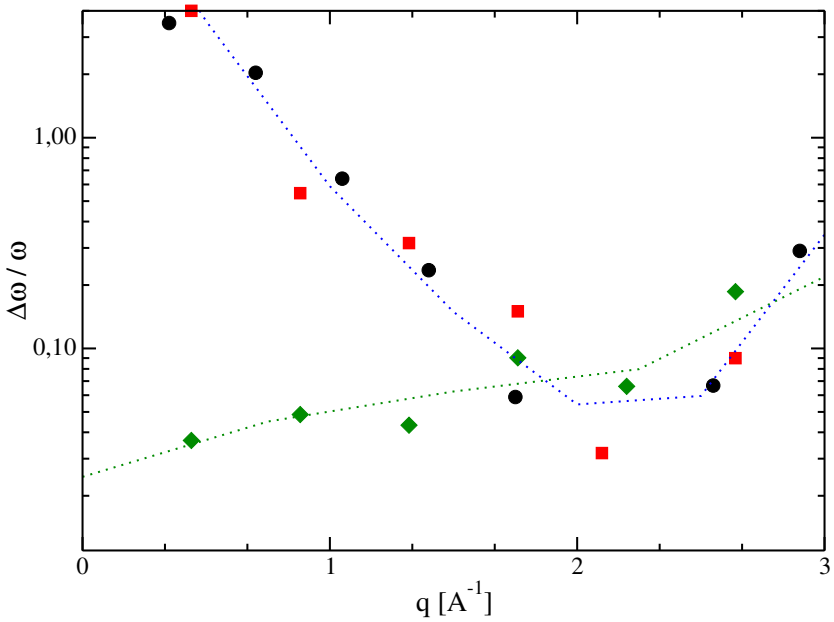


Figure 6.6: half-widths of the 1st peak for both incoherent excitations (black circles: box with N=64; red squares: box with N=125) and coherent ones (green diamonds: box with N=64). The dotted lines are just guides for the eye.

The results in Fig. 6.5a were obtained combining two simulations at $\Delta\tau$ = $0.002\,\mathrm{K}^{-1}$ and $0.001\,\mathrm{K}^{-1}$ respectively obtaining a mesh separation less than 0.5 until about 40 K. In order to obtain meaningful results in the high energy regime, a large collection of RQMC data taken with different imaginary-time steps is needed in order to increase the sampling points. Due to this technical difficulty, at present we have not performed an exhaustive research in the high momentum-transfer limit. However, preliminary calculations show that the spectrum has the expected approximately free-particle like behavior, and that for $q \approx 6\mathring{A}^{-1}$ and above the incoherent part of the DSF accounts for the total scattering.

Indeed, a useful feature of these calculations is that one can separately compute the incoherent part of the full response function, in order to help interpreting the result in terms of possible single-particle and collective excitations.

In Fig. 6.5b we have plotted the calculated excitation spectrum of single-particle excited states. The spectrum shows at least two distinct branches. A lower energy excitation starting at $q \approx 0.5\text{Å}^{-1}$ and propagating with a velocity of the same order of magnitude as the superfluid critical velocity. A second branch can be observed starting at an energy slightly below two times the roton energy, tending asymptotically to the free particle spectrum. In order to help the interpretation of these peaks as single–particle excitations, in Fig. 6.6 we show the relative half-width in energy of these peaks as compared to that of the lower-branch in the full-spectrum Fig. 6.5a. We see that for low-momentum transfer the dominant long-living excitation are the coherent ones, while as we approach the roton minimum the incoherent contributions start playing an important role.

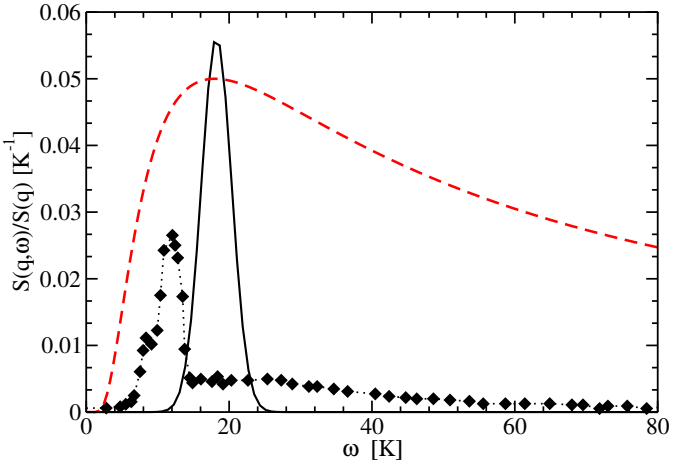


Figure 6.7: $S(q,\omega)$ for liquid $^4$He at $T$ = 0K and $q$ = 2.64Å$^{-1}$ (solid line), compared with the results of Ref. [190] for $q$ = 2.4Å$^{-1}$, $T$ = 0.6K and at pressure 20 bar (dots). The red curve (in arbitrary units) is an example of $\sigma K_P(\sigma,\omega)$ used for computing the inverse response function in this energy range. Notice that the last curve is plotted as a function of $\sigma$ (in K) with a fixed value of $\omega$ = 18K.

Interestingly enough, the lower energy branch crosses the collective excitation spectrum exactly at the roton minimum, thereby reinforcing the picture of the roton as a single particle excitation of an atom exiting the superfluid. The behavior of these single–particle excitations might be significantly affected by the quantum many–body correlations induced by the particle–particle interaction.

At intermediate values of the momentum $q \geq 2.8$Å$^{-1}$, the positions of the peaks become less stable with respect to the specific inversion procedure employed. This might be a signature of the fact that our resolution in that regime is too low.

In order to illustrate this fact, we report in Fig. 6.7 a typical result obtained at high momentum transfer. We compare our results with experiments obtained at non-zero pressure and temperature from Ref. [190]. The experiment presents a well distinct peak along with a slowly decaying tail (generally interpreted as due to single particle excitations [191, 190]). The theoretical curve shows instead a single peak in a position that is not very far from the overall centroid of the experimental response. In this case the existence of a collective peak cannot be established separately. In the graph a typical $\sigma K_P(\sigma,\omega)$ (in the specific case $\omega$ = 18K) is also displayed. We point out once more that for a given value of $P$ the kernel function becomes broader when increasing $\sigma$. In this case it is evident that the width makes the kernel qualitatively similar to the Laplace one. The computational cost required to use a narrower kernel (corresponding to a larger value of $P$) which would allow to resolve the structures observed at large $q$ dramatically increases due to the need of using longer imaginary time paths. This is the current limit of applicability of the method when used along

with unsophisticated inversion techniques.

# Appendices

# Appendix A

# Importance Sampling

In this section we want to introduce, in a more detailed fashion, a powerful technique that allows to improve significantly the efficiency of Monte Carlo techniques: Importance Sampling (IS). To set the stage let us suppose that our problem is to find the following expectation value:

$$\Omega_F = \int F(x)P(x)dx \equiv \mathbb{E}_P[F(\mathbf{X})],$$

where $P(x)$ is some PDF and $F(x)$ is the wanted quantity. As we have already seen before we can attempt to compute $\mu$ by producing a random–walk that samples $P(x)$ and average the integrand $F(x)$ along this walk:

$$\Omega_F = \mathbb{E}_P[F(\mathbf{X})] \longrightarrow \widetilde{\Omega}_F = \frac{1}{M}\sum_i^M F(X_i). \tag{A.1}$$

In many interesting cases however, depending on the structure of both $P(x)$ and $F(x)$, we may have problems with the variance of this estimator. Too see this let us assume that $P(x)$ is a gaussian centered around some mean $x_P$ and with unit variance, while $F(x)$ is another gaussian but centered in another position $x_F$. It is then clear that, if for instance $x_F \gg x_P$, the variance of $\mu_F$ will be extremely big since most of the samples will give $F(X_i) \approx 0$ and only in rare events we will have some non-zero value contributing to the average.

Importance Sampling provides a general–purpose strategy to deal with such problems. By introducing an auxiliary PDF $Q(x) > 0$ and rewriting the expectation value as

$$\Omega_F = \int \frac{F(x)P(x)}{Q(x)}Q(x)dx = \mathbb{E}_Q\left[\frac{F(\mathbf{X})P(\mathbf{X})}{Q(\mathbf{X})}\right], \tag{A.2}$$

the corresponding sample mean will be given by

$$\widetilde{\Omega}_F^{IS} = \frac{1}{M}\sum_i^M \frac{F(X_i)P(X_i)}{Q(X_i)} = \frac{1}{M}\sum_i^M w(X_i)F(X_i), \tag{A.3}$$

where now the configurations $X_i$ are drawn from $Q$ and in the last equality we have introduced *weights* :

$$w(x) = \frac{P(x)}{Q(x)}.$$

A necessary condition for IS to be applicable is then the ability to compute the weight factors $w(X_i)$ for every sample generated along the random–walk. This may be problematic if we don't know the normalizations of the $P$ and $Q$ distributions, and we will come back to that, but for now we will assume that we know the normalization constants of both and use the normalized version.

In order to find a rationale in the choice of the auxiliary distribution $Q$, lets have a look at the expression for the variance:

$$\begin{aligned}\sigma_Q^2 = Var_Q\left[\frac{F(x)P(x)}{Q(x)}\right]^2 &= \int\left(\frac{F(x)P(x)}{Q(x)}\right)^2 Q(x)dx - \Omega_F^2 = \int\frac{(F(x)P(x))^2}{Q(x)}dx - \Omega_F^2 \\ &= \int\left(\frac{F(x)P(x) - \Omega_F Q(x)}{Q(x)}\right)^2 Q(x)dx.\end{aligned} \tag{A.4}$$

The first line of (A.4) already teaches us that a good choice for $Q$ is a function such that the integral $\int (F(x)P(x))^2/Q(x)dx$ is made as small as possible, we then have:

$$\begin{aligned}\int\left(\frac{F(x)P(x)}{Q(x)}\right)^2 Q(x)dx &= \mathbb{E}_Q\left[\left(\frac{F(\mathbf{X})P(\mathbf{X})}{Q(\mathbf{X})}\right)^2\right]_Q \\ &\geq \left(\mathbb{E}_Q\left[\frac{F(\mathbf{X})P(\mathbf{X})}{Q(\mathbf{X})}\right]_Q\right)^2\end{aligned} \tag{A.5}$$

where we have used the fact that for any random variable $\mathbf{Y}$ we have a Cauchy–Schwartz like relation $\mathbb{E}\left[\mathbf{Y}^2\right] \geq \mathbb{E}\left[\mathbf{Y}\right]^2$. Furthermore we have equality if and only if $\mathbf{Y}$ is constant, this implies that $F(\mathbf{X})P(\mathbf{X})/Q(\mathbf{X})$ should also be a constant and then we need: $Q(x) \propto F(x)P(x)$.

We see now that an optimal choice for the auxiliary distribution $Q(x)$ is:

$$Q_{opt}(x) = \frac{F(x)P(x)}{\int Q_{opt}(y)dy} \equiv \frac{F(x)P(x)}{\Omega_F} \tag{A.6}$$

for which we have $\sigma^2_{Q_{opt}} = 0$ and then for any finite sample also the estimator $\widetilde{\sigma}^2_{Q_{opt}} = 0$. Unfortunately this is not going to help us much since the proportionality constant is exactly $\Omega_F^{-1}$, the estimation of which was the target of our original problem!

Although zero–variance densities are not usable in practice, they give a significant insight on the features that we are searching in a good $Q(x)$: it should be as close as possible to be proportional to $F(x)P(x)$. That is, it should be big whenever $F(x)P(x)$ is big and small whenever $F(x)P(x)$ is small.

In most of the practical cases however we can compute only an unnormalized version $P_u(x) = \lambda_P P(x)$ of the original distribution $P$, and the same is usually also true for the auxiliary distribution $Q(x) \to Q_u(x) = \lambda_Q Q(x)$. In the lucky case where $\lambda_P = \lambda_Q$ we can again clearly use the expression (A.3) for the mean, otherwise we can resort to the following self–normalized version:

$$\tilde{\mu}_Q = \frac{\sum_i^M w_u(X_i)F(X_i)}{\sum_i^M w_u(X_i)} \tag{A.7}$$

where the new weights $w_u$ are given by:

$$w_u(x) = \frac{P_u(x)}{Q_u(x)} = \frac{\lambda_P}{\lambda_Q}\frac{P(x)}{Q(x)}. \tag{A.8}$$

As we have seen Importance Sampling is a powerful tool that can turn a slowly convergent algorithm into an extremely efficient one and we will use it in many places of this work.

# Appendix B

# Upper bound proof in complex–hermitian case

In this section of the appendix we give the proof of the upper–bound property for the auxiliary hamiltonians $\mathcal{H}_\gamma$, defined in Sect.2.2, for the general complex–hermitian case. We will concentrate in the simpler case $\gamma = 0$ in equations (2.11) and (2.12), extension to the generic $\gamma \geq 0$ is then straightforward. In what follows we will use the shorthand $\mathcal{H}_{\gamma=0} \equiv \tilde{H}$. Let $\Psi(\mathbf{n})$ be any arbitrary wave function, our goal is to show that

$$\Re[\langle\Psi|\tilde{H}|\Psi\rangle] \geq \Re\left[\langle\Psi|H|\Psi\rangle\right] . \tag{B.1}$$

Let us proceed by considering the following difference:

$$\begin{aligned}
\Re[\langle\Psi|\tilde{H}|\Psi\rangle] - \Re\left[\langle\Psi|H|\Psi\rangle\right] &= \sum_{\mathbf{mn}} \Re\left[\Psi^*(\mathbf{m})(\tilde{H}_{\mathbf{mn}} - H_{\mathbf{mn}})\Psi(\mathbf{n})\right] \\
&= \sum_{\mathbf{mn}} h_{\mathbf{mn}}|\Psi(\mathbf{n})|^2 + \sum_{\mathbf{m}\neq\mathbf{n}} \Re\left[\Psi^*(\mathbf{m})(\tilde{H}_{\mathbf{mn}} - H_{\mathbf{mn}})\Psi(\mathbf{n})\right] \\
&= \sum_{\mathbf{n}} \sum_{\mathfrak{s}_{\mathbf{mn}}\neq -} |\Psi(\mathbf{n})|^2 \frac{\Re\left[\Phi_T^*(\mathbf{m})H_{\mathbf{mn}}\Phi_T(\mathbf{n})\right]}{|\Phi_T(\mathbf{n})|^2} - \Re\left[\Psi^*(\mathbf{m})H_{\mathbf{mn}}\Psi(\mathbf{n})\right]
\end{aligned} \tag{B.2}$$

where the second sum is over all $\mathbf{mn}$ pairs such that $\mathfrak{s}_{\mathbf{mn}}$ of (2.10) is positive–definite. The last term can now be rewritten as:

$$\begin{aligned}
\Re\left[\Psi^*(\mathbf{m})H_{\mathbf{mn}}\Psi(\mathbf{n})\right] &= \Re\left[\Psi^*(\mathbf{m})\Phi_T(\mathbf{m})\Phi_T(\mathbf{m})^{-1}H_{\mathbf{mn}}\Phi_T^*(\mathbf{n})^{-1}\Phi_T^*(\mathbf{n})\Psi(\mathbf{n})\right] \\
&= (\Psi^*(\mathbf{m})\Phi(\mathbf{m}))\Re\left[\Phi_T(\mathbf{m})^{-1}H_{\mathbf{mn}}\Phi_T^*(\mathbf{n})^{-1}\right](\Phi_T^*(\mathbf{n})\Psi(\mathbf{n})) \\
&= (\Psi^*(\mathbf{m})\Phi(\mathbf{m}))\Re\left[\frac{\Phi_T^*(\mathbf{m})}{|\Phi_T(\mathbf{m})|^2}H_{\mathbf{mn}}\frac{\Phi_T(\mathbf{n})}{|\Phi_T(\mathbf{n})|^2}\right](\Phi_T^*(\mathbf{n})\Psi(\mathbf{n}))
\end{aligned} \tag{B.3}$$

where in the second step we used the fact that by employing a real propagator we are imposing a fixed–phase constraint, ie $\Im(\Phi_T^*(\mathbf{n})\Psi(\mathbf{n})) = 0$ for every $\mathbf{n}$

explored in the random walk. The equation for the difference becomes:

$$\begin{aligned}\Re[\langle\Psi|\tilde{H}|\Psi\rangle] - \Re\left[\langle\Psi|H|\Psi\rangle\right] &= \sum_{\mathbf{mn}} \Re\left[\Psi^*(\mathbf{m})(\tilde{H}_{\mathbf{mn}} - H_{\mathbf{mn}})\Psi(\mathbf{n})\right] \\ &= \sum_{\mathbf{n}} \sum_{s_{\mathbf{mn}}\neq -} \frac{\Re\left[\Phi_T^*(\mathbf{m})H_{\mathbf{mn}}\Phi_T(\mathbf{n})\right]}{|\Phi_T(\mathbf{n})|^2}\left(|\Psi(\mathbf{n})|^2 - \frac{(\Psi^*(\mathbf{m})\Phi_T(\mathbf{m}))(\Phi_T^*(\mathbf{n})\Psi(\mathbf{n}))}{|\Phi(\mathbf{m})|^2}\right).\end{aligned} \tag{B.4}$$

Using again the fixed–phase constraint (ie. $(\Phi_T^*(\mathbf{n})\Psi(\mathbf{n})) \equiv (\Phi_T(\mathbf{n})\Psi^*(\mathbf{n}))$) we can rewrite the numerator of the second term in (at least) three equivalent ways:

$$\begin{aligned}(\Psi^*(\mathbf{m})\Phi_T(\mathbf{m}))(\Phi_T^*(\mathbf{n})\Psi(\mathbf{n})) &= -\frac{1}{2}\big(|\Psi^*(\mathbf{m})\Phi_T(\mathbf{m}) - \Phi_T(\mathbf{n})\Psi^*(\mathbf{n})|^2 \\ &\quad - |\Phi_T(\mathbf{n})|^2|\Psi(\mathbf{n})|^2 - |\Phi_T(\mathbf{m})|^2|\Psi(\mathbf{m})|^2\big) \\ &= -\frac{1}{2}\big(|\Psi^*(\mathbf{m})\Phi_T(\mathbf{n}) - \Phi_T^*(\mathbf{m})\Psi(\mathbf{n})|^2 \\ &\quad - |\Phi_T(\mathbf{n})|^2|\Psi(\mathbf{m})|^2 - |\Phi_T(\mathbf{m})|^2|\Psi(\mathbf{n})|^2\big) \\ &= -\frac{1}{2}\big(|\Psi^*(\mathbf{m})\Psi^*(\mathbf{n}) - \Phi_T^*(\mathbf{n})\Phi_T^*(\mathbf{m})|^2 \\ &\quad - |\Phi_T(\mathbf{n})|^2|\Phi_T(\mathbf{m})|^2 - |\Psi(\mathbf{m})|^2|\Psi(\mathbf{n})|^2\big)\end{aligned} \tag{B.5}$$

then using the second expression we have:

$$\begin{aligned}\Re\left[\langle\Psi|\tilde{H}|\Psi\rangle\right] - \Re\left[\langle\Psi|H|\Psi\rangle\right] &= \sum_{\mathbf{mn}} \Re\left[\Psi^*(\mathbf{m})(\tilde{H}_{\mathbf{mn}} - H_{\mathbf{mn}})\Psi(\mathbf{n})\right] \\ &= \sum_{\mathbf{n}} \sum_{s_{\mathbf{mn}}\neq -} \frac{\Re\left[\Phi_T^*(\mathbf{m})H_{\mathbf{mn}}\Phi_T(\mathbf{n})\right]}{|\Phi_T(\mathbf{n})|^2}\left(|\Psi(\mathbf{n})|^2 + \frac{|\Psi^*(\mathbf{m})\Phi_T(\mathbf{n}) - \Phi_T^*(\mathbf{m})\Psi(\mathbf{n})|^2}{2|\Phi_T(\mathbf{m})|^2}\right. \\ &\quad \left. - \frac{|\Phi_T(\mathbf{n})|^2|\Psi(\mathbf{m})|^2}{2|\Phi_T(\mathbf{m})|^2} - \frac{|\Psi(\mathbf{n})|^2}{2}\right) \\ &= (\text{positive terms}) + \sum_{\mathbf{n}} \sum_{s_{\mathbf{mn}}\neq -} \frac{\Re\left[\Phi_T^*(\mathbf{m})H_{\mathbf{mn}}\Phi_T(\mathbf{n})\right]}{2|\Phi_T(\mathbf{n})|^2}\left(|\Psi(\mathbf{n})|^2 - \frac{|\Phi_T(\mathbf{n})|^2|\Psi(\mathbf{m})|^2}{|\Phi_T(\mathbf{m})|^2}\right)\end{aligned} \tag{B.6}$$

Now we note that

$$\Re\left[\Phi_T^*(\mathbf{m})H_{\mathbf{mn}}\Phi_T(\mathbf{n})\right] = \Re\left[\Phi_T^*(\mathbf{n})H_{\mathbf{nm}}\Phi_T(\mathbf{m})\right]$$

for a complex–hermitian hamiltonian, we can then express the sums by allowing only unique $\mathbf{mn}$ combinations:

$$\begin{aligned}\Re\left[\langle\Psi|\tilde{H}|\Psi\rangle\right] - \Re\left[\langle\Psi|H|\Psi\rangle\right] &= \sum_{\mathbf{mn}} \Re\left[\Psi^*(\mathbf{m})(\tilde{H}_{\mathbf{mn}} - H_{\mathbf{mn}})\Psi(\mathbf{n})\right] \\ &= (\text{positive terms}) + \\ &\sum_{\mathbf{n}} {\sum_{s_{\mathbf{mn}}\neq -}}' \Re\left[\Phi_T^*(\mathbf{m})H_{\mathbf{mn}}\Phi_T(\mathbf{n})\right]\left(\frac{|\Psi(\mathbf{n})|^2}{2|\Phi_T(\mathbf{n})|^2} + \frac{|\Psi(\mathbf{m})|^2}{2|\Phi_T(\mathbf{m})|^2} - \right. \\ &\left. \frac{|\Phi_T(\mathbf{n})|^2|\Psi(\mathbf{m})|^2}{2|\Phi_T(\mathbf{m})|^2|\Phi_T(\mathbf{n})|^2} - \frac{|\Phi_T(\mathbf{m})|^2|\Psi(\mathbf{n})|^2}{2|\Phi_T(\mathbf{n})|^2|\Phi_T(\mathbf{m})|^2}\right) \\ &= (\text{positive terms})\end{aligned} \tag{B.7}$$

which by definition is positive. The extension to the case with $\gamma > 0$ is straightforward since we are basically adding a positive constant to the difference.

Along the same lines one can prove that $\Re\left[\langle\Phi_T|\tilde{H}|\Phi_T\rangle\right] = \Re\left[\langle\Phi_T|H|\Phi_T\rangle\right]$ from which we can derive the *supervariational* principle

$$\Re\left[\langle\Phi_T|H|\Phi_T\rangle\right] \geq \Re\left[\langle\Psi|H|\Psi\rangle\right]$$

where now $\Psi$ is the stationary solution of the random walk generated by $\tilde{H}$.

Finally, in order to show that the fixed–node energy is a convex function of the parameter $\gamma$, let us choose $\gamma_1$, $\gamma_2$ and $0 \leq p \leq 1$ such that $\gamma = p\gamma_1 + (1-p)\gamma_2$ and

$$\mathcal{H}_\gamma = p\mathcal{H}_{\gamma_1} + (1-p)\mathcal{H}_{\gamma_2}. \tag{B.8}$$

Since the ground–state energy of $\mathcal{H}_\gamma$ is bounded by the minimum possible energy that can be obtained from each of the two terms in the rhs of (B.8), we find then the variational lower–bound:

$$\langle\Psi_\gamma|\mathcal{H}_\gamma|\Psi_\gamma\rangle \geq p\langle\Psi_{\gamma_1}|\mathcal{H}_{\gamma_1}|\Psi_{\gamma_1}\rangle + (1-p)\langle\Psi_{\gamma_2}|\mathcal{H}_{\gamma_2}|\Psi_{\gamma_2}\rangle. \tag{B.9}$$

# Appendix C

# Recursive evaluation of CCD wave–functions

Let's define the Hartree-Fock state $|HF\rangle$ of a $N$ particle system as

$$|HF\rangle \equiv a^\dagger_{i_1} a^\dagger_{i_2} \cdots a^\dagger_{i_N} |0\rangle \tag{C.1}$$

where $|0\rangle$ is the vacuum-state.

Further we define a generic pair-excited state containing $N$ pairs as

$$a^\dagger_{p_1} a^\dagger_{p_2} \cdots a^\dagger_{p_{2N}} a_{h_1} a_{h_2} \cdots a_{h_{2N}} |HF\rangle \equiv |\, {}^{p_1 p_2 \cdots p_{2N}}_{h_1 h_2 \cdots h_{2N}} \,\rangle \tag{C.2}$$

with the only constraint that $p_1 < p_2 < \cdots < p_{2N}$ and $h_1 < h_2 < \cdots < h_{2N}$.

In our MC simulation walkers can be represented as such pair-excited states.

We can then define the CCD wave-function in the following way

$$|\Psi_{CCD}\rangle \equiv e^{\hat{T}_2} |HF\rangle \tag{C.3}$$

or expanding the exponential

$$|\Psi_{CCD}\rangle = \left(1 + \hat{T}_2 + \frac{1}{2}\hat{T}_2^2 + \dots\right) |HF\rangle \tag{C.4}$$

more explicitly

$$|\Psi_{CCD}\rangle = \left(1 + \sum_{\substack{a<b \\ i<j}} t^{ab}_{ij} a^\dagger_a a^\dagger_b a_j a_i + \frac{1}{2} \sum_{\substack{a<b \\ i<j}} \sum_{\substack{c<d \\ k<l}} t^{ab}_{ij} t^{cd}_{kl} a^\dagger_a a^\dagger_b a^\dagger_c a^\dagger_d a_l a_k a_j a_i + \dots\right) |HF\rangle \tag{C.5}$$

The first non trivial term arise from exciting one pair

$$\hat{T}_2 |HF\rangle = \sum_{\substack{a<b \\ i<j}} t^{ab}_{ij} a^\dagger_a a^\dagger_b a_j a_i |HF\rangle = \sum_{\substack{a<b \\ i<j}} t^{ab}_{ij} |\, {}^{ab}_{ij} \,\rangle \tag{C.6}$$

In order to write the next term in terms of 2 pairs we need to reorganize the

sums

$$\frac{1}{2}\sum_{\substack{a<b\\ i<j}}\sum_{\substack{c<d\\ k<l}} t_{ij}^{ab}t_{kl}^{cd}a_a^\dagger a_b^\dagger a_c^\dagger a_d^\dagger a_l a_k a_j a_i|HF\rangle \rightarrow \sum_{\substack{a<b<c<d\\ i<j<k<l}} \overline{t_{ij}^{ab}t_{kl}^{cd}}a_a^\dagger a_b^\dagger a_c^\dagger a_d^\dagger a_l a_k a_j a_i|HF\rangle$$
$$\equiv \sum_{\substack{a<b<c<d\\ i<j<k<l}} \overline{t_{ij}^{ab}t_{kl}^{cd}}|\,{}^{abcd}_{ijkl}\,\rangle \tag{C.7}$$

where the new coefficients arise from all the different ways we can organize $a, b, c, d$ and $i, j, k, l$ into two pairs $(a_1, b_1)(a_2, b_2)$ with the constraints $a_1 < b_1$, $a_2 < b_2$ , $ab \neq cd$, $ij \neq kl$ and obviously $a < b, c < d, i < j, k < l$.

In the 2–pairs case we have a total of 36 terms:

$$\begin{aligned}
\overline{t_{ij}^{ab}t_{kl}^{cd}} = \frac{1}{2}\big(\; & t_{ij}^{ab}t_{kl}^{cd} - t_{ik}^{ab}t_{jl}^{cd} + t_{il}^{ab}t_{jk}^{cd} \\
& - t_{ij}^{ac}t_{kl}^{bd} + t_{ik}^{ac}t_{jl}^{bd} - t_{il}^{ac}t_{jk}^{bd} \\
& + t_{ij}^{ad}t_{kl}^{bc} - t_{ik}^{ad}t_{jl}^{bc} + t_{il}^{ad}t_{jk}^{bc} \\
& + t_{ij}^{cd}t_{kl}^{ab} - t_{ik}^{cd}t_{jl}^{ab} + t_{il}^{cd}t_{jk}^{ab} \\
& - t_{ij}^{bd}t_{kl}^{ac} + t_{ik}^{bd}t_{jl}^{ac} - t_{il}^{bd}t_{jk}^{ac} \\
& + t_{ij}^{bc}t_{kl}^{ad} - t_{ik}^{bc}t_{jl}^{ad} + t_{il}^{bc}t_{jk}^{ad} \\
& + t_{kl}^{cd}t_{ij}^{ab} - t_{jl}^{cd}t_{ik}^{ab} + t_{jk}^{cd}t_{il}^{ab} \\
& - t_{kl}^{bd}t_{ij}^{ac} + t_{jl}^{bd}t_{ik}^{ac} - t_{jk}^{bd}t_{il}^{ac} \\
& + t_{kl}^{bc}t_{ij}^{ad} - t_{jl}^{bc}t_{ik}^{ad} + t_{jk}^{bc}t_{il}^{ad} \\
& + t_{kl}^{ab}t_{ij}^{cd} - t_{jl}^{ab}t_{ik}^{cd} + t_{jk}^{ab}t_{il}^{cd} \\
& - t_{kl}^{ac}t_{ij}^{bd} + t_{jl}^{ac}t_{ik}^{bd} - t_{jk}^{ac}t_{il}^{bd} \\
& + t_{kl}^{ad}t_{ij}^{bc} - t_{jl}^{ad}t_{ik}^{bc} + t_{jk}^{ad}t_{il}^{bc}\big)
\end{aligned} \tag{C.8}$$

which reduces to just 18 unequivalent terms:

$$\begin{aligned}
\overline{t_{ij}^{ab}t_{kl}^{cd}} = \; & t_{ij}^{ab}t_{kl}^{cd} - t_{ik}^{ab}t_{jl}^{cd} + t_{il}^{ab}t_{jk}^{cd} \\
& - t_{ij}^{ac}t_{kl}^{bd} + t_{ik}^{ac}t_{jl}^{bd} - t_{il}^{ac}t_{jk}^{bd} \\
& + t_{ij}^{ad}t_{kl}^{bc} - t_{ik}^{ad}t_{jl}^{bc} + t_{il}^{ad}t_{jk}^{bc} \\
& + t_{ij}^{cd}t_{kl}^{ab} - t_{ik}^{cd}t_{jl}^{ab} + t_{il}^{cd}t_{jk}^{ab} \\
& - t_{ij}^{bd}t_{kl}^{ac} + t_{ik}^{bd}t_{jl}^{ac} - t_{il}^{bd}t_{jk}^{ac} \\
& + t_{ij}^{bc}t_{kl}^{ad} - t_{ik}^{bc}t_{jl}^{ad} + t_{il}^{bc}t_{jk}^{ad}
\end{aligned} \tag{C.9}$$

The general expression for the $CCD$ wave-function becomes then

$$|\Psi_{CCD}\rangle = |HF\rangle + \sum_{\substack{a<b\\ i<j}} t_{ij}^{ab}|\,{}^{ab}_{ij}\,\rangle + \sum_{\substack{a<b<c<d\\ i<j<k<l}} \overline{t_{ij}^{ab}t_{kl}^{cd}}|\,{}^{abcd}_{ijkl}\,\rangle + \sum_{\substack{a<b<c<d<e<f\\ i<j<k<l<m<n}} \overline{t_{ij}^{ab}t_{kl}^{cd}t_{mn}^{ef}}|\,{}^{abcdef}_{ijklmn}\,\rangle + \ldots \tag{C.10}$$

and so on. If we now want the evaluate the $CCD$ wave-function on a walker configuration containing $m$ excited pairs

$$|\mathbf{n}\rangle = |\,{}^{p_1 p_2 \cdots p_{2m}}_{h_1 h_2 \cdots h_{2m}}\,\rangle \tag{C.11}$$

we have

$$\Psi^{2m}_{CCD}(\mathbf{n}) \equiv \langle \mathbf{n}|\Psi_{CCD}\rangle = \overline{t^{p_1p_2}_{h_1h_2} t^{p_3p_4}_{h_3h_4} \cdots t^{p_{(2m-1)}p_{2m}}_{h_{(2m-1)}h_{2m}}} \tag{C.12}$$

We are searching for a recursion relation like:

$$\Psi^{2m}_{CCD}(\mathbf{n}) = \sum (t\ \Psi^{2(m-1)}_{CCD})(\mathbf{n}) \tag{C.13}$$

.

It turns out that such recursive relation actually exists, in fact we can write:

$$\begin{aligned}
\Psi^{2m}_{CCD}\left(\left|{}^{p_1p_2\cdots p_{2m}}_{h_1h_2\cdots h_{2m}}\right\rangle\right) = \quad & \sum_{k=2}^{2m}(-1)^k t^{p_1p_k}_{h_1h_2} \Psi^{2(m-1)}_{CCD}\left(\left|{}^{\cdots p_{k-1}p_{k+1}\cdots p_{2m}}_{h_3h_4\cdots h_{2m}}\right\rangle\right) \\
& - \sum_{k=3}^{2m}(-1)^k t^{p_2p_k}_{h_1h_2} \Psi^{2(m-1)}_{CCD}\left(\left|{}^{p_1\cdots p_{k-1}p_{k+1}\cdots p_{2m}}_{h_3h_4\cdots h_{2m}}\right\rangle\right) \\
& + \cdots \\
& + t^{p_{(2m-1)}p_{2m}}_{h_1h_2} \Psi^{2(m-1)}_{CCD}\left(\left|{}^{p_1p_2\cdots p_{2m-2}}_{h_3h_4\cdots h_{2m}}\right\rangle\right) \\
& - \sum_{k=2}^{2m}(-1)^k t^{p_1p_k}_{h_1h_3} \Psi^{2(m-1)}_{CCD}\left(\left|{}^{\cdots p_{k-1}p_{k+1}\cdots p_{2m}}_{h_2h_4\cdots h_{2m}}\right\rangle\right) \\
& + \sum_{k=3}^{2m}(-1)^k t^{p_2p_k}_{h_1h_3} \Psi^{2(m-1)}_{CCD}\left(\left|{}^{p_1\cdots p_{k-1}p_{k+1}\cdots p_{2m}}_{h_2h_4\cdots h_{2m}}\right\rangle\right) \\
& - \cdots \\
& - t^{p_{(2m-1)}p_{2m}}_{h_1h_3} \Psi^{2(m-1)}_{CCD}\left(\left|{}^{p_1p_2\cdots p_{2m-2}}_{h_2h_4\cdots h_{2m}}\right\rangle\right) \\
& \cdots
\end{aligned} \tag{C.14}$$

or in a more compact way

$$\Psi^{2m}_{CCD}\left(\left|{}^{p_1p_2\cdots p_{2m}}_{h_1h_2\cdots h_{2m}}\right\rangle\right) = \sum_{j<k}^{2m}\sum_{l=2}^{2m}(-1)^{k+l+j} t^{p_jp_k}_{h_1h_l} \Psi^{2(m-1)}_{CCD}\left(\left|{}^{\cdots p_{j-1}p_{j+1}\cdots p_{k-1}p_{k+1}\cdots p_{2m}}_{\cdots h_{l-1}h_{l+1}\cdots h_{2m}}\right\rangle\right) \tag{C.15}$$

Fixing the first hole index to $h_1$ removes the overcounting of the $m!$ equivalent ways to permute the $t$ amplitudes. Similar relation can be derived in the more general case were also singles (CCSD) and triples (CCSDT) correlations are explicitly included.

# Appendix D

# Continuous time propagation

Let us consider for the moment the linear propagator from (2.7):

$$P^l(\tau, \mathbf{m}, \mathbf{n}) = \langle \mathbf{m}|1 - \Delta\tau\,(H - E_T)|\mathbf{n}\rangle. \tag{D.1}$$

In order for the imaginary–time evolution to project to the ground–state $\phi_0$ we need it to be the dominant eigenstate of $P_l$, this implies that the maximum allowed time–step is

$$\tau_{max} = \frac{2}{E_{max} - E_{min}} \tag{D.2}$$

where $E_{max}$ and $E_{min}$ are the highest and lowest eigenvalues of $H$ respectively ([62]). This condition is necessary in a stochastic treatment of the imaginary–time evolution in order to maintain positive diagonal matrix elements for $P_l$. In simulations employing the linear propagator (D.1), values of $\tau$ much smaller than the maximum value are usually employed due to the difficulty in obtaining reliable estimates of $E_{max}$ in realistic situations. This fact may be a limitation to the efficiency of these algorithms since a huge number of steps have to be carried between consecutive measurements due to long correlation times. Linear propagators however allow also for a quick generation of the single steps enabling very efficient implementations [192].

To further complicate the scenario, when lattice fixed–node methods are employed (ie. diagonal–dumping) this maximum value is reduced even further because the diagonal matrix elements of $P$ gets further pushed towards the negative region by the addition of the sign–violating contributions. If these methods are used to control the sign–problem additional care has to be devoted in the choice of the time–step, greatly deteriorating the efficiency of the overall scheme.

In discrete space however we have also another possibility, we can in fact use directly (meaning sample from) the exponential propagator

$$P^e(\tau, \mathbf{m}, \mathbf{n}) = \langle \mathbf{m}|e^{-\tau(H - E_T)}|\mathbf{n}\rangle, \tag{D.3}$$

that clearly has no problem with negative diagonal elements. These schemes usually come with the name of *continuous–time* evolution.

In this section we will give the necessary details regarding our implementation of this continuous–time evolution based on the work in [63, 64] (see also [54]) . Let us forget the sign–problem for the time being and imagine we are working with the fixed–node importance–sampled greens function (2.13) with $\gamma = 0$ (and the corresponding Hamiltonian $\tilde{H}$) in order to avoid such problems, i.e. we will assume that $\tilde{H}_{\mathbf{m},\mathbf{n}} \leq 0 \forall \mathbf{m} \neq \mathbf{n}$. Furthermore, we will neglect the energy shift $E_T$ since its addition to the following relations is straightforward.

Recall that the Green's function can be written as a product of a stochastic matrix $\tilde{p}_{\mathbf{m},\mathbf{n}}$ and a weight factor $\tilde{b}_{\mathbf{n}}$ (see Sect. ):

$$\tilde{G}_{\mathbf{m},\mathbf{n}}(\Delta\tau) = \delta_{\mathbf{m},\mathbf{n}} - \Delta\tau\tilde{H}_{\mathbf{m},\mathbf{n}} = \tilde{p}_{\mathbf{m},\mathbf{n}}\tilde{b}_{\mathbf{n}} \tag{D.4}$$

where the two factors are given by:

$$\begin{aligned} \tilde{p}_{\mathbf{m},\mathbf{n}} &= \frac{\tilde{G}_{\mathbf{m},\mathbf{n}}(\Delta\tau)}{\tilde{b}_{\mathbf{n}}}, \\ \tilde{b}_{\mathbf{n}} &= \sum_{\mathbf{m}} \tilde{G}_{\mathbf{m},\mathbf{n}}(\Delta\tau) \\ &= 1 - \Delta\tau E_L(\mathbf{n}) \end{aligned} \tag{D.5}$$

and in the last equation we have used the expression for the local energy.

The continuous–time limit is recovered by applying $M$ times $\tilde{G}(\Delta\tau)$ and letting $\Delta\tau \to 0$ while preserving constant the product $\tau = M\Delta\tau$:

$$\begin{aligned} \tilde{G}_{\mathbf{m},\mathbf{n}}(\tau) &= \lim_{M\to\infty} \left(1 - \frac{\tau}{M}\tilde{H}_{\mathbf{m},\mathbf{n}}\right)^M \\ &= \lim_{\Delta\tau\to 0} \left(1 - \Delta\tau\tilde{H}_{\mathbf{m},\mathbf{n}}\right)^{\frac{\tau}{\Delta\tau}} \\ &= \langle \mathbf{m}|e^{-\tau\tilde{H}}|\mathbf{n}\rangle = P^e(\tau, \mathbf{m}, \mathbf{n}). \end{aligned} \tag{D.6}$$

Now note that if we let $\Delta\tau \to 0$ then the probability to make a diagonal move in a single step among the $M$ will accordingly go to $\approx 1$, in fact:

$$\begin{aligned} P_{diag} &= \frac{\tilde{G}_{\mathbf{n},\mathbf{n}}(\Delta\tau)}{\tilde{b}_{\mathbf{n}}} \\ &= \frac{1 - \Delta\tau\tilde{H}_{\mathbf{n},\mathbf{n}}}{1 - \Delta\tau E_L(\mathbf{n})} \\ &\xrightarrow{\Delta\tau\to 0} 1 \end{aligned} \tag{D.7}$$

since the local–energy $E_L$ does not depend on the time step but just on the current configuration $\mathbf{n}$. Accordingly, the probability of making $K$ consecutive diagonal moves will be:

$$\begin{aligned} P_{diag}^K = \left(\frac{\tilde{G}_{\mathbf{n},\mathbf{n}}(\Delta\tau)}{\tilde{b}_{\mathbf{n}}}\right)^K = \left(\frac{1 - \Delta\tau\tilde{H}_{\mathbf{n},\mathbf{n}}}{1 - \Delta\tau E_L(\mathbf{n})}\right)^K \\ \xrightarrow{K\to\infty} e^{\tau(E_L(\mathbf{n}) - \tilde{H}_{\mathbf{n},\mathbf{n}})} \equiv e^{-\tau\tilde{H}_{\mathbf{n}}^{off}} = f_{\mathbf{n}}(\tau) \end{aligned} \tag{D.8}$$

where we have implicitly defined the off–diagonal sum

$$\tilde{H}_{\mathbf{n}}^{off} = \sum_{\mathbf{m}\neq\mathbf{n}} \tilde{H}_{\mathbf{m},\mathbf{n}} < 0.$$

Therefore the elapsed time between consecutive off–diagonal moves is distributed as an exponential distribution $f_{\mathbf{n}}(\tau)$ with average time given by

$$\int_0^\infty \tau f_{\mathbf{n}}(\tau) = -\frac{1}{\tilde{H}^{off}_{\mathbf{n}}} = \left|\frac{1}{\tilde{H}^{off}_{\mathbf{n}}}\right|. \tag{D.9}$$

We can then sample the time when the off-diagonal move happens by using a transformation technique: suppose we have a way to sample values $\xi$ from a uniform distribution $g(\xi) = \text{const}$, due to conservation of probability the samples $\tau$ drawn from the wanted $f_{\mathbf{n}}(\tau)$ will satisfy:

$$|f(\tau)d\tau| = |g(\xi)d\xi| \quad \longrightarrow \left|\frac{d\xi(\tau)}{d\tau}\right| = f_{\mathbf{n}}(\tau) \tag{D.10}$$

where $\tau$ are the samples drawn from the wanted PDF $f_{\mathbf{n}}$. By solving now equation (D.10) for $\xi(\tau)$ and performing the inversion to $\tau = \tau(\xi)$ we obtain the following relation

$$\tau_\xi = \frac{log(\xi)}{\tilde{H}^{off}_{\mathbf{n}}}. \tag{D.11}$$

that allows to sample exactly from $f_{\mathbf{n}}$ using only samples from a uniform distribution $\xi \in (0, 1)$.

Walkers undergoing such random walk accumulate weight during the $K$ diagonal–moves as well as from performing the off–diagonal step. The weight coming from the diagonal moves is given by

$$w_{\mathbf{n}} = \tilde{b}^K_{\mathbf{n}} = (1 - \Delta\tau E_L(\mathbf{n}))^K \xrightarrow{\Delta\tau\to 0} e^{-\tau E_L(\mathbf{n})}. \tag{D.12}$$

For the off–diagonal moves instead we can either sample $\mathbf{m}$ from the normalized probability $P_1(\mathbf{m}, \mathbf{n}) = \tilde{H}_{\mathbf{m},\mathbf{n}}/\tilde{H}^{off}_{\mathbf{n}}$ using for instance a heat–bath algorithm, and in this case the off–diagonal weight would be $w_{\mathbf{m},\mathbf{n}} = 1$, or we can sample off–diagonal moves using a uniform probability $P_2(\mathbf{m}, \mathbf{n}) = 1/N_{conn}$, where $N_{conn}$ is the number of connected state to the starting point $\mathbf{n}$, and then reweight the walker with $w_{\mathbf{m},\mathbf{n}} = P_1(\mathbf{m}, \mathbf{n})/P_2(\mathbf{m}, \mathbf{n})$. In our current implementation we have used the first of these options.

Furthermore, in order for the measurements along the path to be unbiased we want to define equidistant "time–slices" along the random walk, in order to this we simply choose a target time–step $\tau_t$ at the beginning then for each move we first sample a value of $\tau_\xi$ from (D.11), if $\tau_\xi > \tau_t$ we set $\tau = \tau_t$ and use correspondingly a diagonal move if instead $\tau_\xi < \tau_t$ we have to sample an off–diagonal move. The process is preformed until the sum of all the sampled $\tau_\xi$ reaches the target time $\tau_t$.

The final algorithm is then as follows:

1. starting from state $x$, sample a time–step $\tau_\xi$ from (D.11)
2. if $\tau_\xi > \tau_t$, apply the diagonal weight $w_{\mathbf{n}} = e^{-\tau_t E_L(\mathbf{n})}$ and exit (go to next walker)
3. apply diagonal weight $w_{\mathbf{n}} = e^{-\tau_\xi E_L(\mathbf{n})}$
4. choose a new state $\mathbf{m} \neq \mathbf{n}$ according to $P_1(\mathbf{m}, \mathbf{n}) = \tilde{H}_{\mathbf{m},\mathbf{n}}/\tilde{H}^{off}_{\mathbf{n}}$
5. move walker to state $\mathbf{m}$, the time remaining becomes $\tau_t - \tau\xi \to \tau_t$, replace $\mathbf{n}$ with $\mathbf{m}$ and repeat from 1

# Acknowledgements

I would like to express my deep gratitude to my supervisor Francesco Pederiva for its patient guidance, enthusiastic encouragement and the trust he has granted me along all these years. Another special thank is for Abhishek Mukherjee with whom I have shared much of my research journey in Trento and from whom I have learnt so many things. Thanks also to Giuseppina Orlandini for her support and for keeping alive my interest in integral transforms and inversion techniques.

I would like to thank also all the nice people I have met, collaborate and spent time together in the many visits to the US in this three years. Starting from south–west and making a clock–wise round I start from the people in Los Alamos, Joe Carlson and Stefano Gandolfi for the great hospitality and the many interesting discussions. In the Bay Area my biggest thank is for Mal Kalos, not only for having patiently guided me through the mysteries of Fermionic Monte Carlo, but also for the hospitality and for his knowledgeable and passionate introduction to Asian cuisine. My grateful thanks are specially for Eric Schwegler and the guys at LLC for allowing the use of their computational facilities on which most of the research presented in this work have been carried out. Thank you also to Jonathan and Ethan for the nice time and the many interesting discussions. Going further north in the sunny Seattle I wish to thank the people in UW/INT, especially Sanjay Reddy, Jeremy and Ermal for the hospitality and for the many stimulating interactions during my visits. A special thank is due to Ermal for the good time we had together and for his help. Changing coast and going to Ithaca I would like to thank Cyrus Umrigar, for the exquisite hospitality in my visits to Cornell and for having taught me so many things about Monte Carlo. I have enjoyed the time spent there, and this also thanks to Adam, Matt, John, Andreas and the beers/barbecue/whiskeys we had together.

I would like then to express my gratitude to my fellow PhD students in the LISC office Elia, Roberto, Diego, Giorgia, Lorenzo and Marco together with the adopted two Enrico and Paolo and the FBK guys Michele, Marco and Marco, for making the long days at work much more funny and enjoyable.

The last and biggest thank is for my parents for their neverending support.

# Bibliography


[1] D. R. Hartree. The wave mechanics of an atom with a non–coulomb central field. part i. theory and methods. *Math. Proc. Cambridge*, 24:89, 1928.

[2] V. Fock. Näherungsmethode zur lösung des quantenmechanischen mehrkörperproblems. *Z. Physik*, 61:126, 1930.

[3] V. Pandharipande and R. Wiringa. A variational theory of nuclear matter. *Nucl. Phys. A*, 266:269, 1976.

[4] S. Fantoni and S. Rosati. The hypernetted-chain approximation for a fermion system. *Nuovo Cimento A Series 11*, 25:593, 1975.

[5] W. L. McMillan. Ground state of liquid he$^4$. *Phys. Rev.*, 138:A442–A451, Apr 1965.

[6] I. Shavitt and R. J. Bartlett. *Many-Body Methods in Chemistry and Physics: MBPT and Coupled-Cluster Theory*. Cambridge Molecular Science. Cambridge University Press, 2009.

[7] B. D. DAY. Elements of the brueckner-goldstone theory of nuclear matter. *Rev. Mod. Phys.*, 39:719–744, Oct 1967.

[8] W.H. Dickhoff and C. Barbieri. Self-consistent green's function method for nuclei and nuclear matter. *Progress in Particle and Nuclear Physics*, 52(2):377 – 496, 2004.

[9] Rodney J. Bartlett and Monika Musiał. Coupled-cluster theory in quantum chemistry. *Rev. Mod. Phys.*, 79:291–352, Feb 2007.

[10] Malvin H Kalos and Paula A Whitlock. *Monte Carlo methods*. Wiley-VCH, 2009.

[11] M. P. Nightingale and C. J Umrigar. *Quantum Monte Carlo methods in physics and chemistry*, volume 525. Springer, 1998.

[12] D. M. Ceperley and L. Mitas. Quantum monte carlo methods in chemistry. In I Prigogine and S A Rice, editors, *New Methods in Computational Quantum Mechanics//Advances in Chemical Physics, XCIII*, pages 1–38. John Willey & Sons, NY, 1995, 1995.

[13] J. B. Anderson. "quantum monte carlo: Atoms, molecules, clusters, liquids, and solids". *Rev. Comp. Chem.*, 13:133, 2007.

[14] K. Binder, editor. *The Monte Carlo method in condensed matter physics*, volume 71 of *Top. Appl. Phys.* Springer Berlin Heidelberg, 1995.

[15] W. M. C. Foulkes, L. Mitas, R. J. Needs, and G. Rajagopal. Quantum monte carlo simulations of solids. *Rev. Mod. Phys.*, 73(1):33, 2001.

[16] S. C. Pieper. Quantum monte carlo calculations of light nuclei. *Nucl. Phys.*, A751:516–532, 2005.

[17] B. S. Pudliner, V. R. Pandharipande, J. Carlson, Steven C. Pieper, and R. B. Wiringa. Quantum monte carlo calculations of nuclei with $a \sim 7$. *Phys. Rev. C*, 56:1720, Oct 1997.

[18] Steven C. Pieper. Quantum monte carlo calculations of light nuclei. *Riv. Nuovo Cimento*, 31:709, 2008.

[19] S. Gandolfi, A. Yu. Illarionov, K. E. Schmidt, F. Pederiva, and S. Fantoni. Quantum monte carlo calculation of the equation of state of neutron matter. *Phys. Rev. C*, 79:054005, May 2009.

[20] A. Gezerlis and J. Carlson. Low-density neutron matter. *Phys. Rev. C*, 81(2):025803, February 2010.

[21] R. B. Wiringa, V. G. J. Stoks, and R. Schiavilla. Accurate nucleon-nucleon potential with charge-independence breaking. *Phys. Rev. C*, 51:38–51, Jan 1995.

[22] Steven C. Pieper, V. R. Pandharipande, R. B. Wiringa, and J. Carlson. Realistic models of pion-exchange three-nucleon interactions. *Phys. Rev. C*, 64:014001, Jun 2001.

[23] G.H. Booth, A.J.W. Thom, and Ali Alavi. Fermion monte carlo without fixed nodes: A game of life, death and annihilation in slater determinant space. *J. Chem. Phys.*, 131:054106, 2009.

[24] A. Mukherjee and Y. Alhassid. Configuration-interaction Monte Carlo method and its application to the trapped unitary Fermi gas. *Phys. Rev. A*, 88:053622, 2013.

[25] E. Epelbaum, H.-W. Hammer, and U.-G. Meißner. Modern theory of nuclear forces. *Rev. Mod. Phys.*, 81:1773–1825, October 2009.

[26] R. Machleidt and D. R. Entem. Chiral effective field theory and nuclear forces. *Phys. Rep.*, 503:1, June 2011.

[27] H.-W. Hammer, A. Nogga, and A. Schwenk. Colloquium: Three-body forces: From cold atoms to nuclei. *Rev. Mod. Phys.*, 85:197–217, January 2013.

[28] A. Gezerlis, I. Tews, E. Epelbaum, S. Gandolfi, K. Hebeler, A. Nogga, and A. Schwenk. Quantum Monte Carlo Calculations with Chiral Effective Field Theory Interactions. *Phys. Rev. Lett.*, 111(3):032501, July 2013.

[29] John P Perdew and Yue Wang. Accurate and simple analytic representation of the electron-gas correlation energy. *Phys. Rev. B*, 45(23):13244, 1992.

[30] David M Ceperley and BJ Alder. Ground state of the electron gas by a stochastic method. *Phys. Rev. Lett.*, 45(7):566–569, 1980.

[31] J.G. McWhirter and E.R. Pike. *J. Phys. A*, 11(9):1729–45, 1978.

[32] R. Piessens. *J. Comp. Appl. Maths.*, 1:115, 1975.

[33] A. Talbot. *J. Inst. Maths. Applics.*, 23(1):97, 1979.

[34] E. Vitali, M. Rossi, L. Reatto, and D. E. Galli. *Phys. Rev. B*, 82:174510, 2010.

[35] A. Nakayama and N.Makri. *Proc. Natl. Acad. Sci. USA*, 102(12):4230–4234, 2005.

[36] E. C. Svensson, P. Marte, V. F. Sears, and A. D. B. Woods. *J. Can. Phys.*, 54:2178, 1976.

[37] M. Boninsegni and D. M . Ceperley. *Phys. Rev. Lett.*, 74:2288, 1995.

[38] V. D. Efros, W. Leidemann, G. Orlandini, and N. Barnea. *J. Phys. G: Nucl. Part. Phys.*, 34:R459, 2007.

[39] A. Bazavov, D. Toussaint, C. Bernard, J. Laiho, C. DeTar, L. Levkova, M. B. Oktay, Steven Gottlieb, U. M. Heller, J. E. Hetrick, P. B. Mackenzie, R. Sugar, and R. S. Van de Water. Nonperturbative qcd simulations with 2+1 flavors of improved staggered quarks. *Rev. Mod. Phys.*, 82:1349–1417, May 2010.

[40] N. Metropolis, A.W. Rosenbluth, M.N. Rosenbluth, A.H. Teller, and E. Teller. Equations of state calculations by fast computing machines. *J. Chem. Phys.*, 21:1087, 1953.

[41] W.K. Hastings. Monte carlo sampling methods using markov chains and their applications. *Biometrika*, 57:97, 1970.

[42] C. J. Umrigar. Accelerated metropolis method. *Phys. Rev. Lett.*, 71:408, 1993.

[43] E. Neuscamman, C. J. Umrigar, and G. K. Chan. Optimizing large parameter sets in variational quantum monte carlo. *Phys. Rev. B*, 85:045103, Jan 2012.

[44] S. Sorella. Wave function optimization in the variational monte carlo method. *Phys. Rev. B*, 71:241103(R), 2005.

[45] X. Lin, H. Zang, and A. M. Rappe. Optimization of quantum monte carlo wave functions using analytical energy derivatives. *J. Chem. Phys.*, 112:2650, 2000.

[46] C. J. Umrigar and C. Filippi. Energy and variance optimization of many-body wave functions. *Phys. Rev. Lett.*, 94:150201, 2005.

[47] C. J. Umrigar, J. Toulouse, C. Filippi, S. Sorella, and R. G. Hennig. Alleviation of the fermion-sign problem by optimization of many-body wave functions. *Phys. Rev. Lett.*, 98:110201, Mar 2007.

[48] M. H. Kalos. *J. Comput. Phys.*, 1:257, 1966.

[49] K. S. Liu, G. V. Chester, and M. H. Kalos. *Phys. Rev. A*, 10:303, 1974.

[50] P. A. Whitlock, D. M. Ceperley, G. V. Chester, and M. H. Kalos. *Phys. Rev. B*, 19:5598, 1979.

[51] K. J. Runge. *Phys. Rev. B*, 45:7229, 1992.

[52] S. Baroni and S. Moroni. Reptation Quantum Monte Carlo. *eprint arXiv:cond-mat/9808213*, August 1998.

[53] A. Roggero. A stochastic method for the computation of response functions in quantum many–body systems, 2011. Master Thesis – University of Trento.

[54] M. Kolodrubetz and B. K. Clark. Partial node configuration-interaction monte carlo as applied to the fermi polaron. *Phys. Rev. B*, 86:075109, 2012.

[55] G Sugiyama and SE Koonin. Auxiliary field monte-carlo for quantum many-body ground states. *Ann. Phys.*, 168(1):1–26, 1986.

[56] Shiwei Zhang. Quantum monte carlo methods for strongly correlated electron systems. In David Sénéchal, André-Marie Tremblay, and Claude Bourbonnais, editors, *Theoretical Methods for Strongly Correlated Electrons*, CRM Series in Mathematical Physics, pages 39–74. Springer New York, 2004.

[57] Aurel Bulgac, Joaquin E. Drut, and Piotr Magierski. Quantum monte carlo simulations of the bcs-bec crossover at finite temperature. *Phys. Rev. A*, 78:023625, Aug 2008.

[58] Joaquin E. Drut, Timo A. Lahde, Gabriel Wlazlowski, and Piotr Magierski. Equation of state of the unitary fermi gas: An update on lattice calculations. *Phys. Rev. A*, 85:051601, May 2012.

[59] J. Carlson, Stefano Gandolfi, Kevin E. Schmidt, and Shiwei Zhang. Auxiliary-field quantum monte carlo method for strongly paired fermions. *Phys. Rev. A*, 84:061602, Dec 2011.

[60] George H Booth, Andreas Grüneis, Georg Kresse, and Ali Alavi. Towards an exact description of electronic wavefunctions in real solids. *Nature*, 493(7432):365–70, 2013.

[61] F. R. Petruzielo, A. A. Holmes, Hitesh J. Changlani, M. P. Nightingale, and C. J. Umrigar. Semistochastic projector monte carlo method. *Phys. Rev. Lett.*, 109:230201, 2012.

[62] Nandini Trivedi and D. M. Ceperley. Ground-state correlations of quantum antiferromagnets: A green-function monte carlo study. *Phys. Rev. B*, 41(7):4552–4569, 1990.

[63] D. F. B. ten Haaf, H. J. M. van Bemmel, J. M. J. van Leeuwen, W. van Saarloos, and D. M. Ceperley. Proof for an upper bound in fixed-node monte carlo for lattice fermions. *Phys. Rev. B*, 51(19):13039–13045, 1995.

[64] S. Sorella and L. Capriotti. Green function monte carlo with stochastic reconfiguration: An effective remedy for the sign problem. *Phys. Rev. B*, 61(4):2599–2612, 2000.

[65] A. Roggero, A. Mukherjee, and F. Pederiva. Quantum Monte Carlo with Coupled-Cluster wave functions. *Phys. Rev. B*, 88:115138, 2013.

[66] A. Roggero, A. Mukherjee, and F. Pederiva. Quantum Monte Carlo calculations of neutron matter with non-local chiral interactions. *Phys. Rev. Lett.*, 112:221103, 2014.

[67] A. Roggero, A. Mukherjee, and F. Pederiva. Quantum monte carlo with non-local chiral interactions. *Journal of Physics: Conference Series*, 527(1):012003, 2014.

[68] A. Roggero, A. Mukherjee, and F. Pederiva. Constraining the nuclear energy density functional with quantum Monte Carlo calculations. *ArXiv e-prints*, 1406.1631, June 2014.

[69] James J. Shepherd, George H. Booth, and Ali Alavi. Investigation of the full configuration interaction quantum monte carlo method using homogeneous electron gas models. *J. Chem. Phys.*, 136(24):244101, 2012.

[70] Yongkyung Kwon, D. M. Ceperley, and Richard M. Martin. Effects of backflow correlation in the three-dimensional electron gas: Quantum monte carlo study. *Phys. Rev. B*, 58:6800–6806, 1998.

[71] P. López Ríos, A. Ma, N. D. Drummond, M. D. Towler, and R. J. Needs. Inhomogeneous backflow transformations in quantum monte carlo calculations. *Phys. Rev. E*, 74(6):066701, 2006.

[72] James J. Shepherd, George Booth, Andreas Grüneis, and Ali Alavi. Full configuration interaction perspective on the homogeneous electron gas. *Phys. Rev. B*, 85(8):081103, 2012.

[73] Troy Van Voorhis and Martin Head-Gordon. Benchmark variational coupled cluster doubles results. *J. Chem. Phys.*, 113(20):8873–8879, 2000.

[74] Bridgette Cooper and Peter J. Knowles. Benchmark studies of variational, unitary and extended coupled cluster methods. *J. Chem. Phys.*, 133(23):234102, 2010.

[75] James J. Shepherd, Andreas Grüneis, George H. Booth, Georg Kresse, and Ali Alavi. Convergence of many-body wave-function expansions using a plane-wave basis: From homogeneous electron gas to solid state systems. *Phys. Rev. B*, 86(3):035111, 2012.

[76] M. Pedersen Lohne, G. Hagen, M. Hjorth-Jensen, S. Kvaal, and F. Pederiva. *Ab initio* computation of the energies of circular quantum dots. *Phys. Rev. B*, 84:115302, 2011.

[77] R. Gaudoin and J. M. Pitarke. Hellman-feynman operator sampling in diffusion monte carlo calculations. *Phys. Rev. Lett.*, 99:126406, Sep 2007.

[78] R. Gaudoin and J. M. Pitarke. Efficient method for the quantum monte carlo evaluation of the static density response function of a many–electron system. *Phys. Rev. B*, 81:245116, 2010.

[79] L. Mitáš, E. L. Shirley, and D. M. Ceperley. Nonlocal pseudopotentials and diffusion monte carlo. *The Journal of Chemical Physics*, 95(5):3467–3475, 1991.

[80] JE Lynn and KE Schmidt. Real-space imaginary-time propagators for non-local nucleon-nucleon potentials. *Physical Review C*, 86(1):014324, 2012.

[81] Warren E Pickett. Pseudopotential methods in condensed matter applications. *Comp. Phys. Rep.*, 9(3):115–197, 1989.

[82] U Van Kolck. Effective field theory of nuclear forces. *Prog. Part. Nucl. Phys.*, 43:337–418, 1999.

[83] N Kalantar-Nayestanaki, E Epelbaum, J G Messchendorp, and A Nogga. Signatures of three-nucleon interactions in few-nucleon systems. *Rep. Prog. Phys.*, 75(1):016301, 2012.

[84] Bruce R. Barrett, Petr Navrátil, and James P. Vary. Ab initio no core shell model. *Prog. Part. Nucl. Phys.*, 69(0):131 – 181, 2013.

[85] R. Roth, J. Langhammer, A. Calci, S. Binder, and P. Navrátil. Similarity-Transformed Chiral NN+3N Interactions for the Ab Initio Description of C12 and O16. *Phys. Rev. Lett.*, 107(7):072501, August 2011.

[86] Robert Roth, Sven Binder, Klaus Vobig, Angelo Calci, Joachim Langhammer, and Petr Navrátil. Medium-mass nuclei with normal-ordered chiral $nn$+3$n$ interactions. *Phys. Rev. Lett.*, 109:052501, Jul 2012.

[87] H. Hergert, S. K. Bogner, S. Binder, A. Calci, J. Langhammer, R. Roth, and A. Schwenk. In-medium similarity renormalization group with chiral two- plus three-nucleon interactions. *Phys. Rev. C*, 87(3):034307, March 2013.

[88] E. Epelbaum, H. Krebs, D. Lee, and U.-G. Meißner. Ground-state energy of dilute neutron matter at next-to-leading order in lattice chiral effective field theory. *Eur. Phys. J. A*, 40:199–213, May 2009.

[89] E. Epelbaum, H. Krebs, D. Lee, and U.-G. Meißner. Lattice Effective Field Theory Calculations for A=3, 4, 6, 12 Nuclei. *Phys. Rev. Lett.*, 104(14):142501, April 2010.

[90] E. Epelbaum, H. Krebs, D. Lee, and U.-G. Meißner. Ab Initio Calculation of the Hoyle State. *Phys. Rev. Lett.*, 106(19):192501, May 2011.

[91] E. Epelbaum, H. Krebs, T. A. Lähde, D. Lee, and U.-G. Meißner. Viability of Carbon-Based Life as a Function of the Light Quark Mass. *Phys. Rev. Lett.*, 110(11):112502, March 2013.

[92] G. Hagen, M. Hjorth-Jensen, G. R. Jansen, R. Machleidt, and T. Papenbrock. Evolution of Shell Structure in Neutron-Rich Calcium Isotopes. *Phys. Rev. Lett.*, 109(3):032502, July 2012.

[93] G. Hagen, M. Hjorth-Jensen, G. R. Jansen, R. Machleidt, and T. Papenbrock. Continuum Effects and Three-Nucleon Forces in Neutron-Rich Oxygen Isotopes. *Phys. Rev. Lett.*, 108(24):242501, June 2012.

[94] T. Otsuka, T. Suzuki, J. D. Holt, A. Schwenk, and Y. Akaishi. Three-Body Forces and the Limit of Oxygen Isotopes. *Phys. Rev. Lett.*, 105(3):032501, July 2010.

[95] J. D. Holt, T. Otsuka, A. Schwenk, and T. Suzuki. Three-body forces and shell structure in calcium isotopes. *J. Phys. G*, 39(8):085111, August 2012.

[96] J. D. Holt, J. Menéndez, and A. Schwenk. The role of three-nucleon forces and many-body processes in nuclear pairing. *J. Phys. G*, 40(7):075105, July 2013.

[97] V. Somà, C. Barbieri, and T. Duguet. Ab initio Gorkov-Green's function calculations of open-shell nuclei. *Phys. Rev. C*, 87(1):011303, January 2013.

[98] F Wienholtz, D Beck, K Blaum, Ch Borgmann, M Breitenfeldt, RB Cakirli, S George, F Herfurth, JD Holt, M Kowalska, et al. Masses of exotic calcium isotopes pin down nuclear forces. *Nature*, 498(7454):346–349, 2013.

[99] N. Kaiser, S. Fritsch, and W. Weise. Chiral dynamics and nuclear matter. *Nucl. Phys. A*, 697:255–276, January 2002.

[100] J. W. Holt, N. Kaiser, and W. Weise. Chiral Fermi liquid approach to neutron matter. *Phys. Rev. C*, 87(1):014338, January 2013.

[101] I. Tews, T. Krüger, K. Hebeler, and A. Schwenk. Neutron Matter at Next-to-Next-to-Next-to-Leading Order in Chiral Effective Field Theory. *Phys. Rev. Lett.*, 110(3):032504, January 2013.

[102] G. Baardsen, A. Ekström, G. Hagen, and M. Hjorth-Jensen. Coupled-cluster studies of infinite nuclear matter. *Phys. Rev. C*, 88:054312, Nov 2013.

[103] G. Hagen, T. Papenbrock, A. Ekström, K. A. Wendt, G. Baardsen, S. Gandolfi, M. Hjorth-Jensen, and C. J. Horowitz. Coupled-cluster calculations of nucleonic matter. *Phys. Rev. C*, 89:014319, November 2014.

[104] T. Krüger, I. Tews, K. Hebeler, and A. Schwenk. Neutron matter from chiral effective field theory interactions. *Phys. Rev. C*, 88(2):025802, August 2013.

[105] A. Gezerlis, I. Tews, E. Epelbaum, M. Freunek, S. Gandolfi, K. Hebeler, A. Nogga, and A. Schwenk. Local chiral effective field theory interactions and quantum Monte Carlo applications. *ArXiv e-prints*, June 2014.

[106] A. Ekström, G. Baardsen, C. Forssén, G. Hagen, M. Hjorth-Jensen, G. R. Jansen, R. Machleidt, W. Nazarewicz, T. Papenbrock, J. Sarich, and S. M. Wild. Optimized chiral nucleon-nucleon interaction at next-to-next-to-leading order. *Phys. Rev. Lett.*, 110:192502, May 2013.

[107] D. R. Entem and R. Machleidt. Accurate charge-dependent nucleon-nucleon potential at fourth order of chiral perturbation theory. *Phys. Rev. C*, 68:041001, Oct 2003.

[108] Michael Bender, Paul-Henri Heenen, and Paul-Gerhard Reinhard. Self-consistent mean-field models for nuclear structure. *Rev. Mod. Phys.*, 75:121–180, Jan 2003.

[109] S. Gandolfi, J. Carlson, S. Reddy, A. W. Steiner, and R. B. Wiringa. The equation of state of neutron matter, symmetry energy, and neutron star structure. *ArXiv e-prints*, July 2013.

[110] A. Akmal, V. R. Pandharipande, and D. G. Ravenhall. Equation of state of nucleon matter and neutron star structure. *Phys. Rev. C*, 58:1804–1828, Sep 1998.

[111] G. Shen, C. J. Horowitz, and S. Teige. New equation of state for astrophysical simulations. *Phys. Rev. C*, 83:035802, Mar 2011.

[112] AW Steiner, M Hempel, and T Fischer. Core-collapse supernova equations of state based on neutron star observations. *Astrophys. J.*, 774(1):17, 2013.

[113] C. Lin, F. H. Zong, and D. M. Ceperley. Twist-averaged boundary conditions in continuum quantum monte carlo algorithms. *Phys. Rev. E*, 64:016702, Jun 2001.

[114] James M Lattimer and F Douglas Swesty. A generalized equation of state for hot, dense matter. *Nucl. Phys. A*, 535:331, 1991.

[115] G Shen, CJ Horowitz, and S Teige. New equation of state for astrophysical simulations. *Phys. Rev. C*, 83(3):035802, 2011.

[116] G Shen, CJ Horowitz, and E O'Connor. Second relativistic mean field and virial equation of state for astrophysical simulations. *Phys. Rev. C*, 83(6):065808, 2011.

[117] H. Shen, H. Toki, K. Oyamatsu, and K. Sumiyoshi. Relativistic equation of state for core-collapse supernova simulations. *Astrophys. J. Suppl.*, 197(2):20, 2011.

[118] S. Typel, G. Röpke, T. Klähn, D. Blaschke, and H. H. Wolter. Composition and thermodynamics of nuclear matter with light clusters. *Phys. Rev. C*, 81(1):015803, January 2010.

[119] Philippe Nozières and David Pines. *The theory of quantum liquids*, volume 6. Perseus books Cambridge, Massachusetts, 1999.

[120] T. L. Gilbert. Hohenberg-kohn theorem for nonlocal external potentials. *Phys. Rev. B*, 12:2111–2120, Sep 1975.

[121] Arnau Rios, Artur Polls, and W. H. Dickhoff. Depletion of the nuclear fermi sea. *Phys. Rev. C*, 79:064308, Jun 2009.

[122] Frédéric Chevy and Christophe Mora. Ultra-cold polarized fermi gases. *Rept. Prog. Phys.*, 73(11):112401, 2010.

[123] Pietro Massignan, Matteo Zaccanti, and Georg M Bruun. Polarons, dressed molecules and itinerant ferromagnetism in ultracold fermi gases. *Reports on Progress in Physics*, 77(3):034401, 2014.

[124] W. Satula. Wigner energy, odd-even mass staggering and the time-odd mean-fields. In C. Baktash, editor, *Nuclear Structure'98, AIP Conf. Proc. No. 481 (AIP, New York, 1999)*, page 114, 1999.

[125] T. Duguet, P. Bonche, P.-H. Heenen, and J. Meyer. Pairing correlations. i. description of odd nuclei in mean-field theories. *Phys. Rev. C*, 65:014310, Dec 2001.

[126] M. Bender, J. Dobaczewski, J. Engel, and W. Nazarewicz. Gamow-teller strength and the spin-isospin coupling constants of the skyrme energy functional. *Phys. Rev. C*, 65:054322, May 2002.

[127] MM Forbes, A Gezerlis, K Hebeler, T Lesinski, and A Schwenk. The neutron polaron as a constraint on nuclear density functionals. *Phys. Rev. C*, 89:041301(R), 2014.

[128] J. Dobaczewski and J. Dudek. Time-odd components in the mean field of rotating superdeformed nuclei. *Phys. Rev. C*, 52:1827–1839, Oct 1995.

[129] U. Post, E Wüst, and U. Mosel. Time-odd terms in the nuclear hamiltonian at high angular momenta. *Nucl. Phys.*, A437(2):274, 1985.

[130] A. V. Afanasjev and P. Ring. Time-odd mean fields in the rotating frame: Microscopic nature of nuclear magnetism. *Phys. Rev. C*, 62:031302, Aug 2000.

[131] C. Lobo, A. Recati, S. Giorgini, and S. Stringari. Normal state of a polarized fermi gas at unitarity. *Phys. Rev. Lett.*, 97:200403, Nov 2006.

[132] Nikolay Prokof'ev and Boris Svistunov. Fermi-polaron problem: Diagrammatic monte carlo method for divergent sign-alternating series. *Phys. Rev. B*, 77:020408, Jan 2008.

[133] E Chabanat, P Bonche, P Haensel, J Meyer, and R Schaeffer. New skyrme effective forces for supernovae and neutron rich nuclei. *Physica Scripta*, 1995(T56):231, 1995.

[134] E Chabanat, P Bonche, P Haensel, J Meyer, and R Schaeffer. A skyrme parametrization from subnuclear to neutron star densities. *Nucl. Phys.*, A627(4):710–746, 1997.

[135] E Chabanat, P Bonche, P Haensel, J Meyer, and R Schaeffer. A skyrme parametrization from subnuclear to neutron star densities part ii. nuclei far from stabilities. *Nucl. Phys.*, A635(1):231–256, 1998.

[136] J Bartel, Ph Quentin, Matthias Brack, C Guet, and H-B Håkansson. Towards a better parametrisation of skyrme-like effective forces: A critical study of the skm force. *Nucl. Phys.*, A386(1):79–100, 1982.

[137] Stéphane Goriely, Nicolas Chamel, and JM Pearson. Further explorations of skyrme-hartree-fock-bogoliubov mass formulas. xii. stiffness and stability of neutron-star matter. *Phys. Rev. C*, 82(3):035804, 2010.

[138] J Dobaczewski, H Flocard, and J Treiner. Hartree-fock-bogolyubov description of nuclei near the neutron-drip line. *Nucl. Phys.*, A422(1):103–139, 1984.

[139] P.-G. Reinhard, D. J. Dean, W. Nazarewicz, J. Dobaczewski, J. A. Maruhn, and M. R. Strayer. Shape coexistence and the effective nucleon-nucleon interaction. *Phys. Rev. C*, 60(1):014316, July 1999.

[140] X Roca-Maza, G Colo, and H Sagawa. New skyrme interaction with improved spin-isospin properties. *Physical Review C*, 86(3):031306, 2012.

[141] J Erler, CJ Horowitz, Witold Nazarewicz, M Rafalski, and P-G Reinhard. Energy density functional for nuclei and neutron stars. *Phys. Rev. C*, 87(4):044320, 2013.

[142] S. Gandolfi, A. Lovato, J. Carlson, and K. E. Schmidt. From the lightest nuclei to the equation of state of asymmetric nuclear matter with realistic nuclear interactions. *ArXiv e-prints*, June 2014.

[143] Arianna Carbone, Artur Polls, and Arnau Rios. Symmetric nuclear matter with chiral three-nucleon forces in the self-consistent green's functions approach. *Phys. Rev. C*, 88:044302, Oct 2013.

[144] V.D. Efros. *Sov. J. Nucl. Phys.*, 41:949, 1985.

[145] V.D. Efros, W. Leidemann, and G. Orlandini. *Phys. Lett. B*, 338:130, 1994.

[146] G. H. Booth and G. K. Chan. Excited States, Dynamic Correlation Functions and Spectral Properties from Full Configuration Interaction Quantum Monte Carlo. *J. Chem. Phys.*, 137:191102, 2012.

[147] N. Barnea, V. D. Efros, W. Leidemann, and G. Orlandini. The Lorentz Integral Transform and its Inversion. *Few-Body Systems*, 47:201–206, May 2010.

[148] S. C. Pieper, R. B. Wiringa, and J. Carlson. Quantum Monte Carlo calculations of excited states in A = 6–8 nuclei. *Phys. Rev. C*, 70:054325, 2004.

[149] P. Huang, A. Viel, and K.B. Whaley. Efficient implementation of the projector imaginary time spectral evolution (poitse) method for excited states. In W.A. Lester, S.M. Rothstein, and S. Tanaka, editors, *Recent Advances in Quantum Monte Carlo Methods*. World Scientific Publishing, 2002.

[150] G. Orlandini, T. Steele, and D. Harnett. *Nucl. Phys. A*, 686:261, 2001.

[151] T. Munehisa and Y. Munehisa. Calculations for a delta function of hamiltonian by the suzuki-trotter decomposition, 2000. RIKEN Review N. 29.

[152] P. E. Kornilovitch. Real-time correlation functions from imaginary-time evolution. *eprint arXiv:cond-mat/0010100*, October 2000.

[153] D. Arnow, M. H. Kalos, M. A. Lee, and K. E. Schmidt. *J. Chem. Phys.*, 77:5562, 1982.

[154] M.H. Kalos and F. Pederiva. *Phys. Rev. Lett.*, 85:3547, 2000.

[155] F. Calcavecchia, F. Pederiva, M. H. Kalos, and T. D. Kühne. On the Sign Problem of the Fermionic Shadow Wave Function. *ArXiv e-prints*, April 2014.

[156] S. Bacca, N. Barnea, G. Hagen, G. Orlandini, and T. Papenbrock. First principles description of the giant dipole resonance in 16O. *Phys. Rev. Lett.*, 111:122502, 2013.

[157] G. Orlandini, S. Bacca, N. Barnea, G. Hagen, M. Miorelli, and T. Papenbrock. *Few Body Syst.*, 55:907–911, 2014.

[158] G. K. Watugala. *Int. J. Maths. Ed. Sci. Tech.*, 24:35–43, 1993.

[159] F. B. M. Belgacem and A. A. Karaballi. *J. Appl. Maths. Stoch. An.*, 2006:23, 2006.

[160] M.M. Lavrent'ev, V.G. Romanov, and S.P. Shishatskii. *Ill-posed Problems of Mathematical Physics and Analysis*. Am. Math. Soc., 1986.

[161] E. T. Jaynes. *Information Theory and Statistical Mechanics, in Statistical Physics, Ed. K. Ford*. New York: Benjamin, 1963.

[162] R. N. Silver, D. S. Sivia, and J. E. Gubernatis. *Phys. Rev. B*, 41:2380, 1990.

[163] Yannis Burnier and A. Rothkopf. Bayesaian approach to spectral function reconstruction for euclidean quantum field theories. *Phys. Rev. Lett.*, 111:182003, 2013.

[164] S. R. White. *Computer Simulation Studies in Condensed Matter Physics III*. Springer-Verlag Berlin, Heidelberg, 1991.

[165] A. W. Sandvik. *Phys. Rev B*, 57:10287, 1998.

[166] P. Magierski and G. Wlazlowski. *Comput. Phys. Commun.*, 183:2264–2271, 2012.

[167] A. Bulgac P. Magierski, G. Wlaz?owski. *Phys. Rev. Lett.*, 107:145304, 2011.

[168] G. Wlazlowski and P. Magierski. *Phys.Rev. C*, 83:012801, 2011.

[169] Victor D. Efros. Method to solve integral equations of the first kind with an approximate input. *Phys. Rev. E*, 86:016704, Jul 2012.

[170] Stefano Baroni and Saverio Moroni. Reptation quantum monte carlo: A method for unbiased ground-state averages and imaginary-time correlations. *Phys. Rev. Lett.*, 82:4745–4748, Jun 1999.

[171] W.K. Yuen, T.J. Farrar, and S.M. Rothstein. No-compromise reptation quantum monte carlo. *J. Phys. A: Mathl. Theor.*, 40:F639–F646, 2007.

[172] W.K. Yuen, D.G. Oblinsky, R.D. Giacometti, and S.M. Rothstein. Improving reptation quantum monte carlo. *Int. J. Quant. Chem.*, 109(14):3229–3234, 2009.

[173] C. Pierleoni and D.M. Ceperley. Computational methods in coupled electron-ion monte carlo. *Chem. Phys. Chem.*, 6:1–8, 2005.

[174] R. A. Cowley and A. D. B. Woods. *Can. J. Phys.*, 49:177, 1971.

[175] J.S. Brooks and R.J. Donelly. The calculated thermodynamic properties of superfluid helium 4, 1977. J. Phys. Chem. Ref. Data, Vol. 6(1).

[176] L. Tisza. *Phys. Rev.*, 72:838, 1947.

[177] L. Landau. *J. Phys. U.S.S.R.*, 5:71, 1941.

[178] R.P. Feynman. *Phys. Rev.*, 94:262, 1954.

[179] R.P. Feynman and M. Cohen. *Phys. Rev.*, 102:1189, 1956.

[180] D. M . Ceperley. *Rev. Mod. Phys.*, 67(2):279–355, 1995.

[181] M. Boninsegni, C. Pierleoni, and D. M . Ceperley. *Phys. Rev. Lett.*, 72:1854, 1994.

[182] R. A. Aziz, J. S. Carley, V. P. S. Nain, W. L. Taylor, and G. T. McConville. *J. Chem. Phys.*, 70:4330, 1979.

[183] P. A. Withlock, M. H. Kalos, M. A. Lee, and G. V. Chester. *Phys. Rev. B*, 24:115–130, 1981.

[184] S. Ujevic and S. Vitiello. *Phys. Rev. B*, 71:224518, 2005.

[185] S. Fantoni, S. Moroni, and G. Senatore. *Phys. Rev. B*, 52:547–558, 1995.

[186] H.R. Glyde and A. Griffin. *Phys. Rev. Lett.*, 65:1454–1457, 1990.

[187] F. Mezei and G.W. Stirling. *in 75th Jubilee Conference on Helium-4, ed. by J. G. M. Armitage, World Scientific, Singapore*, page 111, 1983.

[188] C. L. Byrne. *IEEE Transactions on Image Processing,IP-2*, 96, 1993.

[189] A. Woods and R. Cowley. *Can. J. Phys.*, 49:177, 1971.

[190] J. V. Pearce, R. T. Azuah, B. Fak, A. R. Sakhel, H. R. Glyde, and W. Stirling. *J. Phys. Cond. Mat.*, 13:4421, 2001.

[191] B. Få k, L. P. Regnault, and J. Bossy. *J. Low Temp. Phys.*, 89:345, 1992.

[192] G. H. Booth, S. D. Smart, and A. Alavi. Linear-scaling and parallelizable algorithms for stochastic quantum chemistry. *ArXiv e-prints*, May 2013.